

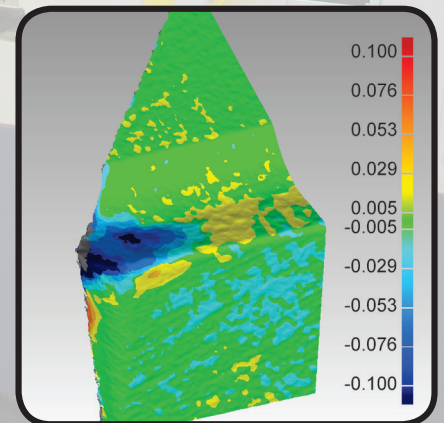
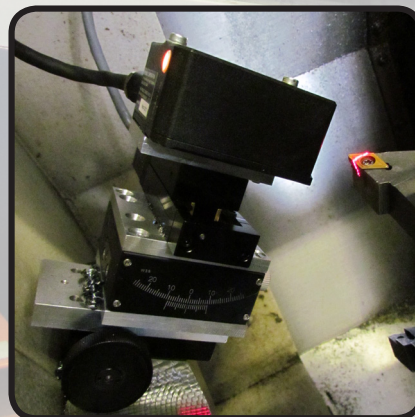


Strojniški vestnik

Journal of Mechanical Engineering



no. **9**
year **2015**
volume **61**



Strojniški vestnik – Journal of Mechanical Engineering (SV-JME)

Aim and Scope

The international journal publishes original and (mini)review articles covering the concepts of materials science, mechanics, kinematics, thermodynamics, energy and environment, mechatronics and robotics, fluid mechanics, tribology, cybernetics, industrial engineering and structural analysis.

The journal follows new trends and progress proven practice in the mechanical engineering and also in the closely related sciences as are electrical, civil and process engineering, medicine, microbiology, ecology, agriculture, transport systems, aviation, and others, thus creating a unique forum for interdisciplinary or multidisciplinary dialogue.

The international conferences selected papers are welcome for publishing as a special issue of SV-JME with invited co-editor(s).

Editor in Chief

Vincenc Butala

University of Ljubljana, Faculty of Mechanical Engineering, Slovenia

Technical Editor

Pika Škraba

University of Ljubljana, Faculty of Mechanical Engineering, Slovenia

Founding Editor

Bojan Kraut

University of Ljubljana, Faculty of Mechanical Engineering, Slovenia

Editorial Office

University of Ljubljana, Faculty of Mechanical Engineering
SV-JME, Aškerčeva 6, SI-1000 Ljubljana, Slovenia

Phone: 386 (0)1 4771 137

Fax: 386 (0)1 2518 567

info@sv-jme.eu, <http://www.sv-jme.eu>

Print: Grafex, d.o.o., printed in 380 copies

Founders and Publishers

University of Ljubljana, Faculty of Mechanical Engineering,
Slovenia

University of Maribor, Faculty of Mechanical Engineering,
Slovenia

Association of Mechanical Engineers of Slovenia

Chamber of Commerce and Industry of Slovenia,

Metal Processing Industry Association

President of Publishing Council

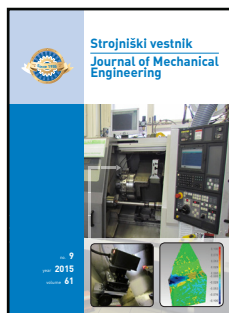
Branko Širok

University of Ljubljana, Faculty of Mechanical Engineering, Slovenia

Vice-President of Publishing Council

Jože Balič

University of Maribor, Faculty of Mechanical Engineering, Slovenia



Cover:

The tool-wear of cutting tools has a very strong impact on the product quality as well as efficiency of the machining processes. Despite the nowadays high automation level in machining industry, tool-wear is usually measured off the machine tool. This paper presents an innovative, robust and reliable direct measuring procedure for measuring spatial cutting tool-wear in-line, with the usage of laser profile sensor.

Courtesy: Laboratory for Cutting,
Faculty of Mechanical Engineering,
University of Ljubljana, Slovenia

International Editorial Board

Kamil Arslan, Karabuk University, Turkey

Josep M. Bergada, Politechnical University of Catalonia, Spain

Anton Bergant, Litostroj Power, Slovenia

Miha Boltežar, UL, Faculty of Mechanical Engineering, Slovenia

Franci Čuš, UM, Faculty of Mechanical Engineering, Slovenia

Anselmo Eduardo Diniz, State University of Campinas, Brazil

Igor Emri, UL, Faculty of Mechanical Engineering, Slovenia

Imre Felde, Obuda University, Faculty of Informatics, Hungary

Janez Grum, UL, Faculty of Mechanical Engineering, Slovenia

Imre Horvath, Delft University of Technology, The Netherlands

Aleš Hribernik, UM, Faculty of Mechanical Engineering, Slovenia

Soichi Ibaraki, Kyoto University, Department of Micro Eng., Japan

Julius Kaplunov, Brunel University, West London, UK

Iyas Khader, Fraunhofer Institute for Mechanics of Materials, Germany

Jernej Klemenc, UL, Faculty of Mechanical Engineering, Slovenia

Milan Kljajin, J.J. Strossmayer University of Osijek, Croatia

Janez Kušar, UL, Faculty of Mechanical Engineering, Slovenia

Gorazd Lojen, UM, Faculty of Mechanical Engineering, Slovenia

Thomas Lübben, University of Bremen, Germany

Janez Možina, UL, Faculty of Mechanical Engineering, Slovenia

George K. Nikas, KADMOS Engineering, UK

José L. Ocaña, Technical University of Madrid, Spain

Miroslav Plančak, University of Novi Sad, Serbia

Vladimir Popović, University of Belgrade, Faculty of Mech. Eng., Serbia

Franci Pušavec, UL, Faculty of Mechanical Engineering, Slovenia

Bernd Sauer, University of Kaiserslautern, Germany

Rudolph J. Scavuzzo, University of Akron, USA

Arkady Voloshin, Lehigh University, Bethlehem, USA

General information

Strojniški vestnik – Journal of Mechanical Engineering is published in 11 issues per year (July and August is a double issue).

Institutional prices include print & online access: institutional subscription price and foreign subscription €100,00 (the price of a single issue is €10,00); general public subscription and student subscription €50,00 (the price of a single issue is €5,00). Prices are exclusive of tax. Delivery is included in the price. The recipient is responsible for paying any import duties or taxes. Legal title passes to the customer on dispatch by our distributor.

Single issues from current and recent volumes are available at the current single-issue price. To order the journal, please complete the form on our website. For submissions, subscriptions and all other information please visit: <http://en.sv-jme.eu/>.

You can advertise on the inner and outer side of the back cover of the journal. The authors of the published papers are invited to send photos or pictures with short explanation for cover content.

We would like to thank the reviewers who have taken part in the peer-review process.

The journal is subsidized by Slovenian Research Agency.

ISSN 0039-2480

© 2015 Strojniški vestnik - Journal of Mechanical Engineering.

All rights reserved. SV-JME is indexed / abstracted in:

SCI-Expanded, Compendex, Inspec, ProQuest-CSA, SCOPUS,

TEMA. The list of the remaining bases, in which SV-JME is

indexed, is available on the website.

Strojniški vestnik - Journal of Mechanical Engineering is available on <http://www.sv-jme.eu>, where you access also to papers' supplements, such as simulations, etc.

Contents

Strojniški vestnik - Journal of Mechanical Engineering
volume 61, (2015), number 9
Ljubljana, September 2015
ISSN 0039-2480

Published monthly

Papers

Luka Čerče, Franci Pušavec, Janez Kopač: A New Approach to Spatial Tool Wear Analysis and Monitoring	489
Matej Müller, Gorazd Novak, Franc Steinman, Gašper Rak, Tom Bajcar: Influence of the Operating and Geometric Characteristics of a Bottom-hinged Flap Gate on the Discharge Coefficient of a Side Weir	498
Mohsen Moslemi, Mohammadreza Khoshravan: Cohesive Zone Parameters Selection for Mode-I Prediction of Interfacial Delamination	507
Andrzej Milecki, Dominik Rybarczyk: Modelling of an Electrohydraulic Proportional Valve with a Synchronous Motor	517
Yu Zhang, Hongzhi Yan, Tao Zeng: Computerised Design and Simulation of Meshing and Contact of Formate Hypoid Gears Generated with a Duplex Helical Method	523
Jernej Laloš, Tomaž Požar, Janez Možina: High-Frequency Calibration of Piezoelectric Displacement Sensors Using Elastic Waves Induced by Light Pressure	533
Primož Potočnik, Ervin Strmčnik, Edvard Govekar: Linear and Neural Network-based Models for Short-Term Heat Load Forecasting	543

A New Approach to Spatial Tool Wear Analysis and Monitoring

Luka Čerče* – Franci Pušavec – Janez Kopač

University of Ljubljana, Faculty of Mechanical Engineering, Slovenia

The tool wear of cutting tools has a very strong impact on the product quality as well as on the efficiency of the machining processes. Despite the current high automation level in the machining industry, a few key issues prevent complete automation of the entire turning process. One of these issues is tool wear, which is usually measured off the machine tool. Therefore, its in-line characterization is crucial.

This paper presents an innovative, robust and reliable direct measurement procedure for measuring spatial cutting tool wear in-line, using a laser profile sensor. This technique allows for the determination of 3D wear profiles, which is an advantage over the currently used 2D subjective techniques (microscopes, etc.). The use of the proposed measurement system removes the need for manual inspection and minimizes the time used for wear measurement.

In this paper, the system is experimentally tested on a case study, with further in-depth analyses of spatial cutting tool wear performed. In addition to tool wear measurements, tool wear modelling and tool life characterization are also performed. Based on this, a new tool life criterion is proposed, which includes the spatial characteristics of the measured tool wear.

The results of this work show that novel tool wear and tool life diagnostics yield an objective and robust methodology allowing tool wear progression to be tracked, without interruptions in the machining process or in the performance of the machining process. This work shows that such an automation of tool wear diagnostics, on a machine tool, can positively influence the productivity and quality of the machining process.

Keywords: machining process, tool wear measurement, spatial tool wear, in-line monitoring, volumetric estimator, tool life prediction

Highlights

- Newly developed measuring system to determine spatial cutting tool wear in-line.
- Spatial cutting tool wear measurements were performed on a case study.
- Tool wear modelling and tool life characterization has been performed.
- A new tool life criterion is proposed.

0 INTRODUCTION AND STATE OF THE ART

The tool wear of cutting tools has a very strong impact on product quality as well as on the efficiency of machining processes overall. Despite the current high automation level in the machining industry, a few key issues prevent complete automation of the entire turning process. One of these issues is tool wear, which is usually measured off the machine tool and is still done by hand under a toolmaker's microscope. There is no any industry wide procedure for automating the process of measuring wear. Furthermore, such conventional wear measurement requires stopping the automated turning, removing the tool, measuring the tool and putting the tool back to the holder, which is a considerable time loss relative to the tool's life. Therefore, the in-line characterization of cutting tool wear is crucial for cutting cycle times and costs, as well increasing the overall efficiency of the machining process.

This paper presents an innovative, robust and reliable direct measuring procedure for measuring spatial cutting tool wear in-line using a laser profile sensor. This technique allows 3D wear profiles to be determined, which is an advantage over the currently

used 2D subjective techniques (microscopes, etc.). The use of the proposed measurement system removes the need for manual inspection and minimizes the time used for wear measurement. A tool life characterization is also performed. Based on this, a new tool life criterion is proposed that includes the spatial characteristics of the measured tool wear. In the next three subsections, extensive state reviews are performed.

0.1 Tool Wear Characterization Review

The damages to a cutting tool are the consequence of the stress state and thermal loads on the tool surfaces, which in turn depend on the cutting mode, i.e. turning, milling or drilling, cutting parameters and the cooling/lubrication conditions.

During machining, the cutting tool wear mechanisms and their rates are very sensitive to changes in the cutting operation and the cutting conditions. To minimize machining costs, one must not only to find the most suitable cutting tool and work material combination for a given machining operation, but also reliably predict the tool life and also the tool changing/replacement protocol.

Tool wear mainly occurs at the rake and flank face. Flank wear is caused by friction between the flank face of the cutting tool and the machined workpiece surface and leads to loss of the cutting edge. Therefore, flank wear affects the dimensional accuracy and surface finish quality of the product. In practice, flank wear is generally used as the cutting tool wear criteria. When critical value of tool wear has been reached, the cutting tool is assumed to have reached its tool life. This point should be placed before but close to the moment when the cutting tool fails due to excessive stresses and thermal alterations. To avoid this, the cutting tool must be replaced before reaching its critical limit. In practice, the preferred cutting tool life criteria is the tool-flank wear threshold. However, even though the wear should progress gradually and should thus be easily monitored, tool wear is hard to predict due to uncertainties in the machining process. Therefore, to robustly define the tool-changing protocol in NC (numeric control) programs, the in-line tool wear measurement is inevitable [1] and [2].

In practice, some directly measured dimensional characteristics and criteria of typical wear patterns, i.e. crater, flank wear, and depth-of-cut notch wear at the extremities, for HSS (high speed steels), carbide and ceramics tools, are standardized in ISO 3685 [3], as shown in Fig. 1.

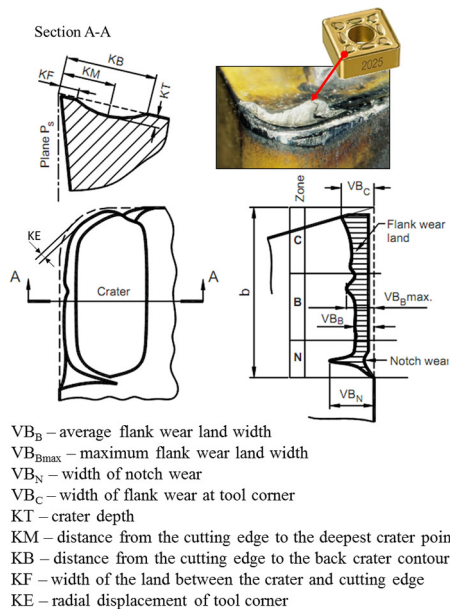


Fig. 1. Typical wear pattern according to ISO 3685

The process of cutting tool wear consists of three characteristic parts: the initial (running-in) period, the longest uniform (progressive) wear period and the

accelerated wear period leading often to catastrophic failure [1].

The machining process needs to be, on the one hand, stopped at the right time to prevent undesired consequences of the tool wear, such as increases in cutting forces, vibrations, noise, and temperature in the cutting zone, as well as deviation of part dimensions and surface quality from the point of view of respective tolerance values, while on the other hand, the tool should be replaced as late as possible to increase efficiency and decrease tooling costs.

In reality, several wear mechanisms occur simultaneously, although any one of them may dominate the process. They can be qualitatively identified as mechanical, thermal and adhesive. Mechanical types of wear, which include abrasion, chipping, early gross fracture and mechanical fatigue, are basically independent of temperature. Thermal loads appear with plastic deformation, thermal diffusion and oxygen corrosion as their typical forms, and increase drastically at high temperatures, thus accelerating the tool failure by causing easier tool material removal (by abrasion or attrition) [4].

At high cutting speed, temperature-activated wear mechanisms including diffusion (solution wear), chemical wear (oxidation and corrosion wear), and thermal wear (superficial plastic deformation due to thermal softening effect) occur. By contrast, at lower cutting speeds adhesive and abrasive wear are the most significant types of wear.

ISO 3685 notes that the type of tool wear is difficult to determine when machining with grooved tools. Ee et al. [5] found that the tool wear pattern on a worn grooved tool insert is influenced by the three-dimensional chip-flow and by the complex chip-groove configurations. They also found that some grooved tools fail long before the major flank wear (VB_B) reaches its failure criterion in many cases. It is also shown, that grooved tools demonstrate tool-failure as a result of concurrent multiple tool wear parameters. This confirms that the tool wear, or rather tool life, is significantly affected by the combined effects of cutting conditions and chip-groove configurations. This also answers the question as to why several new measurable parameters have been proposed for tool wear in machining with grooved tools (Fig. 2) [5]. From the grooved tools wear parameters, it can be seen that the wear regions in grooved tools can be very specific, such as the notch, etc. However, in general they can be divided into three major wear regions. These are: (a) the edge wear region, (b) the land and secondary face wear region, and (c) the backwall wear region (Fig. 2).

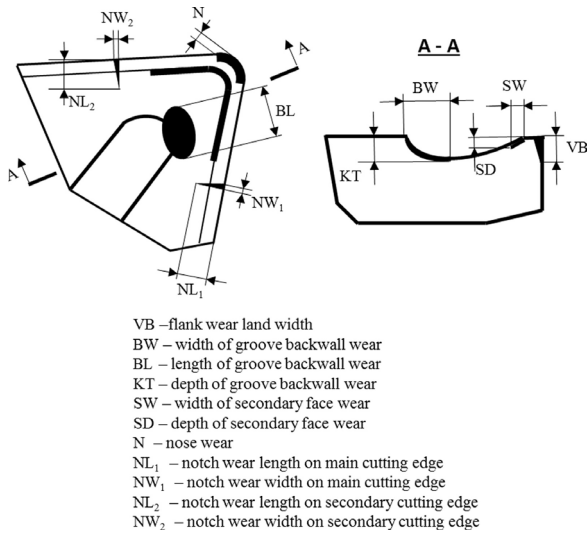


Fig. 2. Measurable tool wear parameters in grooved tools

0.2 Tool Wear Measurement Review

Tool wear can be measured using direct measuring techniques or estimated by indirect measuring techniques [6] and [7]. In indirect measuring techniques, tool wear is estimated using other more measurable machining process variables such as cutting force, surface finish, acoustic emission, vibrations, energy consumption, temperature, etc. [8]. A survey of the literature indicates that a variety of approaches have been applied to tool wear prediction [9] to [12]. Conversely, with direct measuring techniques, condition monitoring is carried out by analysing the change in geometry of the cutting tool. Usually these techniques can be taken only between two sequential machining runs, because the major flank of the tool is not visible during actual machining. Direct tool condition monitoring techniques can be divided into two-dimensional and three-dimensional techniques. Additionally, they can be divided into measurements made directly on the machine tool or outside it (using a microscope, etc.).

Kurada and Bradley [13] have designed a system consisting of a fiber-optic light source to illuminate the tool and a CCD camera, which is used in combination with a high resolution video zoom microscope. The resolution in the captured image was approximately 3 μm per pixel. Images are captured orthogonally to the flank face. The actual wear region identification and measurement relies on the specular reflection of the wear area from the fiber-optic lights. Identification of the tool wear area is performed in 2D, through the wear area reflection.

Lanzetta [14] has a different approach to the problem. Using two cameras, a grey-scale image is taken from the nose of the tool and image of the tool silhouette is taken from the top of the tool. The silhouette is taken with a back-light and the tool nose is directly illuminated. Images are also taken with a directional light from the top of the tool to detect crater wear. Flank wear is measured from the silhouette image. The silhouette of the worn tool is compared to the silhouette of the unused tool, which gives an estimate of the tool flank wear. Measurement error is reported to be less than 5%. Niranjana Prasad and Ramamoorthy [15] measured the crater wear using stereo vision. Stereo vision is not achieved by using two cameras but with the tool moving between two images taken with the same grey-scale camera. Resolution is 12 $\mu\text{m} \times 10 \mu\text{m}$ per pixel. The depth and width of the crater wear is measured and the measurements can be made accurately. However, the images of the tool are taken outside the turning machine and no method for automatically measuring the flank wear is presented.

On the other hand, Jurkovic et al. [16] used structured light from a laser diode to capture elevation information from the tool surface. A monochrome CCD camera was used to capture the images with a halogen light. The resolution of the image was approximately 3 μm per pixel. Flank wear can be measured as well as crater wear using the elevation information. The system was combined with a CNC lathe. Additionally, Devillez et al. [17] shows that white light interferometry is a useful tool for measuring cutting insert crater wear. The measurement methodology allows examination of all aspects of crater wear after the metal cutting process, although this technique does not permit in-line tool crater measurement and flank wear measurement. Dawson and Kurfess [18] present a novel method for quantifying tool wear using three-dimensional computational metrology that is also based on white light interferometry. The presented measurement technique allows measurement of flank and crater wear. Furthermore, a technique was developed to measure the deviations between the three-dimensional tool data and an 'ideal' version of an unworn cutting tool. The calculated deviations were then used to define the tool wear volume. Wang et al. [19] employ a phase shifting method using fringe patterns to measure crater wear by constructing a 3D map of the tool insert. Four fringe patterns with various phase-shifts are projected onto the rake face of the tool upon which four grey-level images are captured. With appropriate setup, the system can be used for on-line

crater wear measurement in industry, but the accuracy level is limited. A combination of the fringe projection system and the white light interferometry is used by Weckenmann and Nalbantlic [20].

The main disadvantages of the described methods are the inability to measure wear profiles in depth (three-dimensional geometry of crater wear – KT , etc.) and/or that they cannot be robustly used directly in the machine tool. To perform the measurement with these methods, the cutting insert should be removed from the machine tool. This causes time loss and possible problems with the accuracy of subsequent processing. This paper presents a novel method belonging to direct measuring method of determining of cutting tool wear. This method offers the possibility of three-dimensional tool wear measurement directly on the machine tool, without the need to remove cutting inserts from the tool holder (machine tool).

0.3 Tool Life Assessment Review

Flank wear of cutting tools is often selected as the tool life criterion because it determines the diametric accuracy of machining, as well as its stability and reliability [21]. According to the ISO 3685:1993 [3], the assessment of flank wear is determined by its direct measurement. Flank wear is considered using an aged Taylor's tool life equation having a phenomenological nature. The Taylor Tool life estimation is based on experimental data that are gathered by measuring the time until the tool life criterion is fulfilled using several different cutting speeds. Based on this experimental set, a curve (regression model) representing the tool life can be constructed. The drawback is that it describes just the linear section of the tool life curve. Additionally, Taylor's basic equation does not include the effect of cutting feed and is limited to a certain range of speeds. It also does not give information about the tool wear at any particular time t during turning. Even though an improved Taylor model exists that includes both feed and depth of cut, but they still just cover the tool life, not the wear at particular times.

An additional problem of such a model is that it is constructed based on tool wear measurements performed by the operator, etc. These assessments are subjective and insufficient. They do not include the tool geometry (the flank angle, the rake angle, the cutting edge angle, etc.) so they are not suitable for comparing cutting tools having different geometries. They do not include the cutting regime and thus do not reflect the real amount of work material removed

by the tool during the time over which the measured flank wear is achieved [21].

The selection of these characteristics depends upon the particular objective of a tool wear study. Most often, dimensional accuracy dictates this selection, i.e. the need to manufacture parts within the tolerance limits assigned for tool wear. As such, the tool life defined by this criterion may be referred to as dimension tool life. Dimension tool life can be characterized by the time within which the tool works without adjustment or replacement (T_{c-t}); by the number of parts produced (N_{p-t}); by the length of the tool path (L_{c-t}); by the area of the machined surface (A_{c-t}) and by the linear relative wear (h_{l-r}) [21]. All these characteristics listed are particulars and thus, in general, do not allow for the optimal control of cutting operations, comparison of different cutting regimes, assessment of different tool materials, etc. For example, dimensional tool life is of little help if one needs to compare cutting tools that work at different cutting speeds and feeds and/or when the widths of their flank wear land are not the same. The problem lies in the complex cutting tool surface geometries as well as high stochastic behaviour of the tool wear from the point of view of aggression and location. Therefore, the combination of the dimensional wear rate with the relative surface wear and the specific dimensional tool life are much more general characteristics to be used in metal cutting tests conducted everywhere from the research laboratory to shop floor level. A new 3D tool wear based estimation is presented in Section 2.

1 NEWLY DEVELOPED MEASUREMENT SYSTEM

The newly developed measuring system (Fig. 3) consists of a high-accuracy 2D laser displacement sensor Keyence LJ-G015 with a proper controller Keyence LJ-G5001 [22], a motorized linear translation stage Standa 8MT173-DCE2 and a LabVIEW application developed for process control.

The measurement range of the 2D laser displacement sensor Keyence LJ-G015 is in Z-axis (height) ± 2.6 mm and 7.0 mm in X-axis at the reference distance. The repeatability in the Z-axis is 0.2 μm and 2.5 μm in the X-axis. For linear positioning of the measurement head, a motorized linear translation stage is used with a minimal incremental motion of 0.1 μm and bi-directional repeatability of 0.4 μm [23].

With movement of the profile sensor across the cutting tool and the support of the developed software (LabVIEW application), the profile data are grabbed and prepared in a matrix form for further evaluation and analysis. A laser displacement sensor measures

the distance from the measurement head to the points projected on the measured object. In this way the Z-coordinates of the point cloud are measured. The X-coordinate is defined by the specification of the laser displacement sensor [22], while the Y-coordinate represents linear stage feed direction.

While the relative position/orientation of the measuring head has a significant influence on the measurements, the analysis of its orientation has been experimentally and empirically analysed in one of our previous works [24]. The accuracy was determined to reach $\pm 8 \mu\text{m}$. The measurement system was mounted on Mori Seiki SL-153 CNC lathe as shown in Fig. 3. This allows a quick measurement of tool wear on the machine tool itself. Between two machining operations, the average measuring procedure can be performed in approximately 20 s, without stopping the machining process.

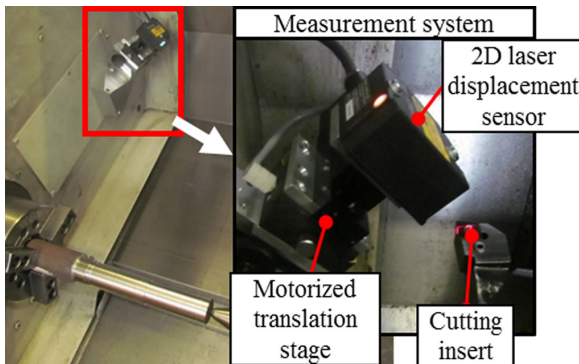


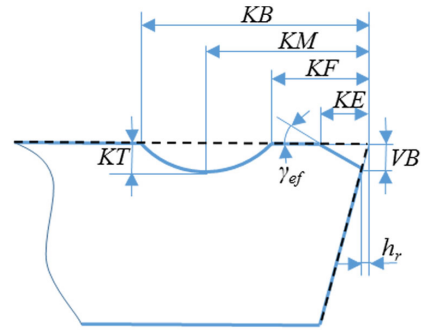
Fig. 3. Measurement system mounted on a Mori Seiki machine tool

Thus, we can take a measurement that includes far more information about tool wear, without having to remove the cutting inserts from the holders, which would be necessary if we were to measure tool wear on a toolmaker's microscope.

2 TOOL LIFE PREDICTION FOR GROOVED CUTTING INSERTS

Tool life prediction in grooved tools involves simultaneously occurring multiple wear parameters, as presented in Fig. 2 (wear on flank, wear on rake, etc.). However, there are no universally accepted standards for tool life prediction in grooved tools. The ISO 3685 based criterion, established for flat-faced tools, is usually not implementable on grooved tools. The geometry of the cutting tool significantly affects tool life, as the geometry defines the magnitude and direction of the cutting force and its components, the sliding velocity at the tool-chip interface, the distribution of the thermal energy released in

machining, the temperature distribution in the cutting edge, etc. [21]. Therefore, a new tool life prediction method is presented based on the rate of cutting tool geometry change and consequent change in the stresses at the cutting edge.



--- New cutting edge — Used cutting edge

Fig. 4. Measured cutting tool wear geometry

The greatest impact on prediction of the tool life for finishing operations is the radial wear h_r (Fig. 4). Thus, we can say that the cutting tool is useful until the radial wear h_r exceeds the prescribed tolerance of the workpiece. With the previously presented measurement system, current radial wear h_r can be measured directly on the machine tool. In this way we can control, measure and predict the cutting tool life for finishing operations.

In roughing operations, productivity is important (i.e. material removal rate), so the tool breakage is under consideration. For this purpose the influence of mechanical load on the rake face of the cutting insert will be simulated using the finite element method (FEM). Tamizharasan and Kumar [25] use FEM for simulating the effect of tool geometry on flank wear, surface roughness and cutting forces. In our case, the 3D model of the cutting insert is defined on the basis of measurements results (KT , VB , KE and γ_{ef}) performed in a case study. The mechanical pressure distribution on the rake face is applied based on the Zorev model [26]. The pressure decreases nonlinearly from the maximum value at the cutting edge to zero at the end of chip-tool contact zone (where the chip separates from the rake face). Apart from the model of contact load distribution on the tool faces, the contact load also depends on the contact area of the tool with the chip and the workpiece. On the rake face, the contact area depends on the contact length between the chip and tool rake face, l_{cr} , as shown in Fig. 5, and chip width. The length can be measured from the rubbing marks on the rake face, which can be

seen from the 3D wear measurements. The case study will be shown in the next section.

As a benefit of these FEM simulations, stress analyses show how changes in the geometry (wear) bring the tool to the stress limit/structure breakage. Based on this, the tool life can be predicted and with it the undesired tool breakage in real machining operations.

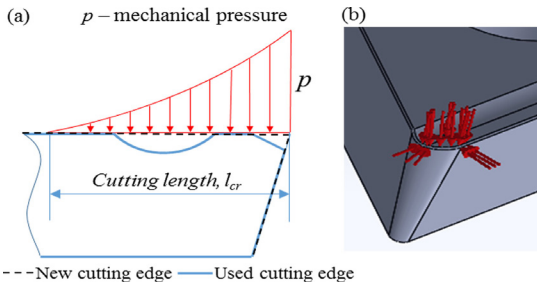


Fig. 5. a) mechanical pressure distribution on the cutting tool edge, and b) 3D model of cutting insert with pressure distribution on the rake face

As a proof of the proposed concept, the measurement system presented in Section 1 was tested in a machining environment. The results of a case study were analysed as described above and are presented in the next section.

3 CASE STUDY AND RESULTS

The presented measurement system has been tested on a case study of bearing steel machining (100Cr6 – AISI52100) performance determination. A bar shaped workpiece with diameter 40 mm and length 290 mm was machined. Machining tests were conducted on a Mori Seiki SL-153 turning machine. Commercially available Sumitomo DCGT 11T304 R-FX cutting inserts, grade ACZ310, were used with SDCJR 2020K11 tool-holder. All the machining experiments were performed dry, while the cutting parameters have been defined according to the manufacturer’s recommendations: $a_p=1\text{ mm}$, $v_c=250\text{ m/min}$ and $f=0.12\text{ mm/rev}$. To follow the progress of the wear, the sequential longitudinal workpiece turning operations were performed on 20 mm length intervals. The result of the corresponding tool wear progress is presented in Fig. 6. The measurement itself is executed in approximately 20 seconds, grabbing the $6\text{ mm} \times 3.5\text{ mm}$ area, with a grid size of $0.01\text{ mm} \times 0.005\text{ mm}$ ($\Delta X \times \Delta Y$).

To determine tool wear progress, six repeated measurements were performed. The first picture shows the new (unworn) cutting insert, while the

sixth picture show the critical wear that occur on the rake face of the cutting tool after 7.4 minutes of machining. The colour on those plots corresponds for the wear magnitude. Red color shows the presence of BUE (build up edge), while the blue color shows the actual wear. Nevertheless, the BUE regions were not dominant. Furthermore, from the result it can be seen that abrasive, adhesive and diffusion wear occurred on the cutting edge. Abrasive and diffusion wear can be observed on the rake face (region of blue colour), while adhesive wear is seen in the growing region of yellow colour. The progression of crater wear on rake face and chipping of cutting edge can also be observed (Fig. 6, darker blue zone on cutting edge). Observing the rake face crater wear depth formation, with a growing region of darker blue colour, high temperatures in cutting area are suspected.

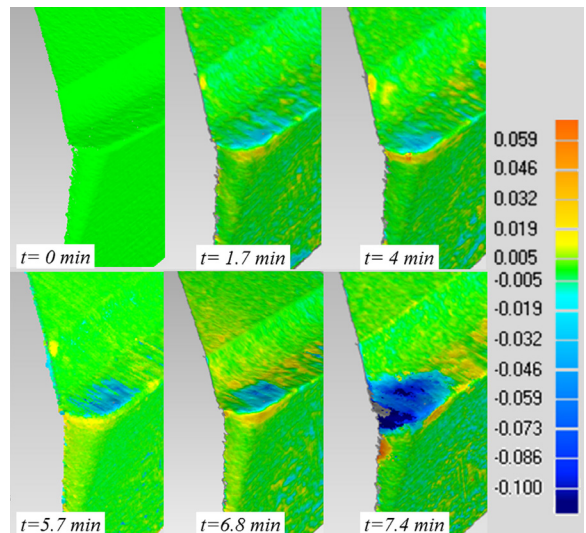


Fig. 6. 3D deviation results (new vs. worn cutting tools)

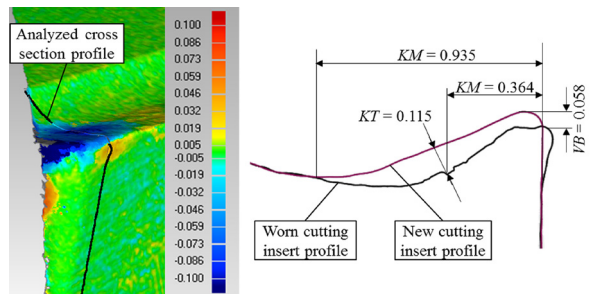


Fig. 7. Measurement of typical wear patterns, according to ISO 3685, on a cross section profile, 0.5 mm from secondary flank face after 7.4 min of cutting

For analysis of the extent and shape of the wear, an example of a cross section perpendicular to the primary flank face is shown and analysed in Fig. 7.

The wear corresponds to the 7.4 min of machining. The depth of flank wear is clearly visible from the comparison of cutting inserts cross-sections profiles (new vs. worn). Fig. 7 shows that with the use of the presented measurement system, the extent of the wear formation can be precisely determined. The depth of the crater for this particular case is $KT = 0.115$ mm and the flank wear extends to a depth $VB = 0.058$ mm.

The 3D deviation results showed that the maximum wear occurs 0.5 mm from the secondary flank face. Therefore, these profiles have been analysed and the results of flank wear land width (VB) and total wear volume (V_{Wear}) as a function of cutting time are presented in Fig. 8.

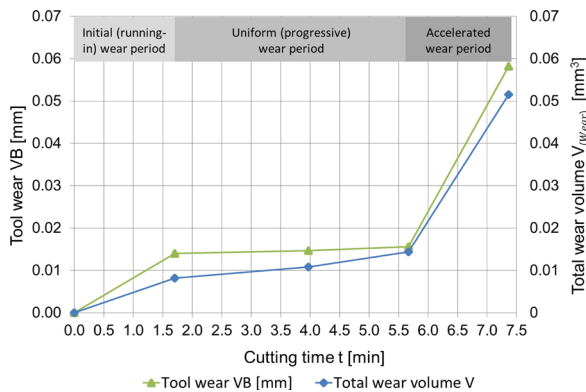


Fig. 8. Flank wear land width (VB) for cross section profile 0.5 mm from the secondary flank face and total wear volume (V_{Wear}) as function of cutting time t

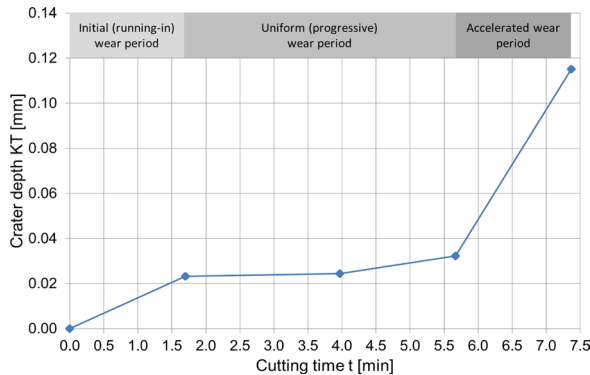


Fig. 9. Maximum crater depth (KT) as a function of cutting time t for the cross section profile 0.5 mm from secondary flank face

Maximum crater depth (KT) as a function of cutting time is shown in Fig. 9. In all cases, three characteristic parts are observed: the initial (running-in) period (up until 1.5 min), the longest uniform (progressive) wear period (from 1.5 min to 5.5 min) and the accelerated wear period (from 5.5 min on).

The results confirm that observing just the VB is not sufficient for tool life prediction. Higher wear than VB is observed on the rake face (although values are significantly smaller than KT). The VB will result in higher cutting forces and missing tolerances, while KT will cause cutting tool breakage.

In practice, the most important consideration in selecting cutting tools and cutting conditions is tool life (T). T is defined as the time when the measured wear levels exceed a predefined threshold. A standard measure of tool life is the time to develop a flank wear length VB_B of 0.3 mm or VB_{Bmax} of 0.6 mm, in case of cemented carbides. Standard ISO 3685:1993 also recommends a maximum value of KT (KT_{max}). It can be empirically calculated via following equation [2]:

$$KT_{max} = 0.06 + 0.3 \cdot f, \quad (1)$$

where f is feed. For the cutting parameters used, the KT_{max} is 0.096 mm. From the results presented in Fig. 9 it is apparent that KT is critical, while the critical value for VB is not reached (Fig. 8) ($VB = 0.06$ mm after 7.5 min of machining). However, this empirical KT_{max} equation does not include a lot of important parameters in machining (material, depth of cut, etc.) and is questionable. Therefore, this paper also aims to present a new approach in tool life prediction using FEM simulations. For this purpose, geometry data from cross-section profiles of the worn cutting inserts have been used to build an accurate 3D model of the cutting edge. This model has been used for stress analysis. The maximum pressure $p = 0.95$ GPa has been calculated from cutting forces. This has been performed with a back calculation of online measured cutting forces. The cutting tool material properties presented in Table 1 were found in the literature [27] and [28] and used in this work.

Table 1. Cutting tool material properties

Elastic modulus	600000 N/mm ²
Poisson's ratio	0.225
Shear modulus	263000 N/mm ²
Mass density	14.5 kg/m ³
Tensile strength	450 N/mm ²
Compressive strength	6000 N/mm ²

The results of the FEM simulation are presented in the Fig. 10. In Fig. 10a, the results of stress analyses of the new cutting insert are presented, while Fig. 10b presents results for the critically worn insert. The wear corresponds to the 7.4 min of machining. The maximal stress for a new insert (a) is 7.3×10^8 N/m²

(yellow zone), while for the worn inserts (b) it is much bigger $1.1 \times 10^9 \text{ N/m}^2$ (red zone).

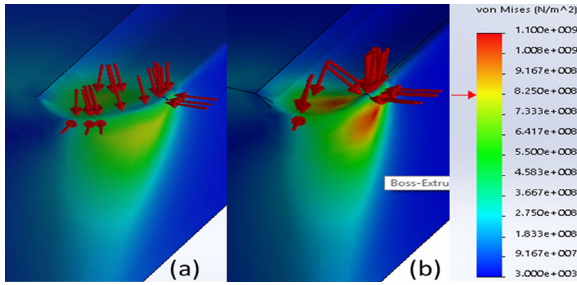


Fig. 10. FEM simulation results for a) new (unworn) and b) worn cutting insert

The presented results showed that FEM simulations are in good correlation with the experimental data presented in Fig. 8 (total volume V_{Wear}) and Fig. 9 (KT).

The stress at the cutting tool edge increases drastically when crater wear becomes significant (from 5 min to the end), as can be seen in Fig. 11. This happens due to the notch effect. By increasing the depth of crater wear, the cross-section of the cutting edge became smaller, and therefore the stress in the material increases. This leads to catastrophic tool fracture (breakage) when the stresses became higher than the material yield strength. The cutting time limit before the breakage occurs defines the cutting tool life.

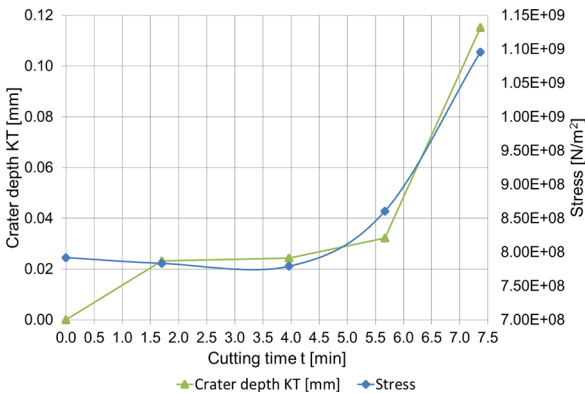


Fig. 11. FEM simulated stress and crater depth KT as function of cutting time t for cutting tool edge

On the other hand, maximal crater depth KT can be predicted from the yield strength and actual stress. With maximal KT thus defined the presented spatial measurement system can be used for the robust control of the process and its efficiency. Going a step further, this procedure can also cover the KT and VB

combination (or any other wear mechanism), where the cutting tool breakage can be foreseen.

4 CONCLUSIONS

This paper presents an innovative, robust and reliable direct measuring procedure for determining spatial cutting tool wear in-line on machine tools. The technique allows for the determination of 3D wear profiles, an advantage over the currently used 2D subjective techniques (microscopes, etc.). The use of the proposed measurement system removes the need for manual inspection and minimizes the time used for wear measurement. The measurement data thus obtained are actually realistic 3D models of the cutting tool/wear, where we can clearly see what the existing conditions of the cutting tool are. With information on three-dimensional deviations, this method outperforms traditional 2D deviation methods in accuracy, efficiency and reliability.

Besides tool wear, this work also upgrades existing tool life methodologies with spatial tool wear information. A new methodology for tool life prediction, based on FEM stress simulation is presented. Because it is known that the geometry of the cutting tool directly affects tool life, cross-section profiles of the worn cutting inserts have been used to build an accurate 3D model of the cutting edge. For this, the measurement system has been experimentally tested on a case study machining 100Cr6 bearing steel on a CNC lathe. The cutting tool wear has been measured directly on the machine tool, without the need to remove the cutting insert from the machine tool and analyse it under the microscope. In addition to the presented conventional results (VB , KT), this new spatial tool wear measuring system, allows tool wear volume V_{Wear} to be measured and analysed.

A constructed FEM model was run to predict tool life. This model compared unworn and worn insert geometries and used stress analysis for the FEM. The mechanical loading was same for worn and unworn inserts and was experimentally defined. From the obtained stress results, the cutting time limit before breakage occurs (tool life) can be more accurately defined/predicted. These predictions for the case study are also correlated with the fractures occurring on the cutting tool. The results show that FEM simulations can be used to determine the time limit before fracturing of the cutting tool/tool life.

The results of this work show that novel tool wear and tool life diagnostics represent an objective and robust method of tracking tool wear progress, without interrupting the machining process, as well

as the performances of the machining process itself. Additionally, the tool life/tool fracturing can be robustly predicted in-line. To summarize, our work shows that the automation of tool wear diagnostics in-line on a machine tool can beneficially influence the productivity, efficiency and quality of the machining process.

5 REFERENCES

- [1] Cheng, K. (2009). *Machining Dynamics, Fundamentals, Applications and Practices*. Springer, London.
- [2] Kopač, J. (2008). *Machining: Theoretical Basis and Technological Information*. Faculty of Mechanical Engineering, Ljubljana. (in Slovene)
- [3] ISO 3685 (1993): *Tool-Life Testing with Single-Point Turning Tools*. International Organization for Standardization, Geneva.
- [4] Grzesik, W. (2008). *Advanced Machining Processes of Metallic Materials*. Elsevier B.V., Amsterdam.
- [5] Ee, K.C., Balaji, A. K., Jawahir, I.S. (2003). Progressive tool wear mechanisms and their effects on chip-curl/chip-form in machining with grooved tools: an extended application of the equivalent toolface (ET) model. *Wear*, vol. 255, no. 7-12, p. 1404-1413, DOI:10.1016/S0043-1648(03)00112-1.
- [6] Kurada, S., Bradley, C. (1997). A review of machine vision sensors for tool condition monitoring. *Computers in Industry*, vol. 34, no. 1, p. 55-72, DOI:10.1016/S0166-3615(96)00075-9.
- [7] Dutta, S., Pal, S. K., Mukhopadhyay, S., Sen, R. (2013). Application of digital image processing in tool condition monitoring: A review. *CIRP Journal of Manufacturing Science and Technology*, vol. 6, no. 3, p. 212-232, DOI:10.1016/j.cirpj.2013.02.005.
- [8] Siddhpura, A., Paurobally, R. (2013). A review of flank wear prediction methods for tool condition monitoring in a turning process. *The International Journal of Advanced Manufacturing Technology*, vol. 65, no. 1-4, p. 371-393, DOI:10.1007/s00170-012-4177-1.
- [9] Dimla Snr, D.E. (2000). Sensor signals for tool wear monitoring in metal cutting operations—a review of methods. *International Journal of Machine Tools and Manufacture*, vol. 40, no. 8, p. 1073-1098, DOI:10.1016/S0890-6955(99)00122-4.
- [10] Govekar, E., Gradišek, J., Grabec, I. (2000). Analysis of acoustic emission signals and monitoring of machining processes. *Ultrasonics*, vol. 38, no. 1-8, p. 598-603, DOI:10.1016/S0041-624X(99)00126-2.
- [11] Teti, R., Jemielniak, K., O'Donnell, G., Dornfeld, D. (2010). Advanced monitoring of machining operations. *CIRP Annals - Manufacturing Technology*, vol. 59, no. 2, p. 717-739, DOI:10.1016/j.cirp.2010.05.010.
- [12] Venkata Rao, K., Murthy, B.S.N., Mohan Rao, N. (2013). Cutting tool condition monitoring by analyzing surface roughness, work piece vibration and volume of metal removed for AISI 1040 steel in boring. *Measurement*, vol. 46, no. 10, p. 4075-4084, DOI:10.1016/j.measurement.2013.07.021.
- [13] Kurada, S., Bradley, C. (1997). A machine vision system for tool wear assessment. *Tribology International*, vol. 30, no 4, p. 295-304, DOI:10.1016/S0301-679X(96)00058-8.
- [14] Lanzetta, M. (2001). A new flexible high-resolution vision sensor for tool condition monitoring. *Journal of Materials Processing Technology*, vol. 119, no. 1-3, p. 73-82, DOI:10.1016/S0924-0136(01)00878-0.
- [15] Niranjan Prasad, K., Ramamoorthy, B. (2001). Tool wear evaluation by stereo vision and prediction by artificial neural network. *Journal of Materials Processing Technology*, vol. 112, no. 1, p. 43-52, DOI:10.1016/S0924-0136(00)00896-7.
- [16] Jurkovic, J., Korosec, M., Kopac, J. (2005). New approach in tool wear measuring technique using CCD vision system. *International Journal of Machine Tools and Manufacture*, vol. 45, no. 9, p. 1023-1030, DOI:10.1016/j.ijmactools.2004.11.030.
- [17] Devillez, A., Lesko, S., Mozer W. (2004). Cutting tool crater wear measurement with white light interferometry. *Wear*, vol. 256, no. 1-2, p. 56-65, DOI:10.1016/S0043-1648(03)00384-3.
- [18] Dawson, T.G., Kurfess, T.R. (2005). Quantification of tool wear using white light interferometry and three-dimensional computational metrology. *International Journal of Machine Tools and Manufacture*, vol. 45, no. 4-5, p. 591-596, DOI:10.1016/j.ijmactools.2004.08.022.
- [19] Wang, W.H., Wong, Y.S., Hong, G.S. (2006). 3D measurement of crater wear by phase shifting method. *Wear*, vol. 261, no. 2, p. 164-171, DOI:10.1016/j.wear.2005.09.036.
- [20] Weckenmann, A., Nalbantic, K. (2003). Precision measurement of cutting tools with two matched optical 3D-sensors. *CIRP Annals - Manufacturing Technology*, vol. 52, no. 1, p. 443-446, DOI:10.1016/S0007-8506(07)60621-0.
- [21] Astakhov, V.P. (2004). The assessment of cutting tool wear. *International Journal of Machine Tools & Manufacture*, vol. 44, no. 6, p. 637-647, DOI:10.1016/j.ijmactools.2003.11.006.
- [22] Keyence (2010). *High-accuracy 2D Laser Displacement Sensor*. Keyence.
- [23] Standa. Translation Stage with DC motor, from <http://www.standa.it>, accessed on 2014-21-2
- [24] Cerce, L., Pusavec, F., Dugar, J., Kopac, J. (2013). Further development of the spatial cutting tool wear measurement system. *Journal of Production Engineering*, vol. 16, no. 2, p. 5-10.
- [25] Tamizharasan T., Senthil Kumar N. (2012). Optimization of Cutting Insert Geometry Using DEFORM-3D: Numerical Simulation and Experimental Validation. *International Journal of Simulation Modelling*, vol. 11, no. 2, p. 65-76, DOI:10.2507/IJSIMM11(2)1.200.
- [26] Zorev, N.N. (1966). *Metal Cutting Mechanics*. Pergamon Press, Oxford.
- [27] Zhao, Z., Hong, S.Y. (1992). Cryogenic properties of some cutting tool materials. *Journal of Materials Engineering and Performance*, vol. 1, no. 5, p. 705-714, DOI:10.1007/BF02649252.
- [28] Sandvik. Cemented Carbide, from <http://www.sandvik.com>, accessed on 2015-2-10.

Influence of the Operating and Geometric Characteristics of a Bottom-hinged Flap Gate on the Discharge Coefficient of a Side Weir

Matej Müller^{1,*} – Gorazd Novak² – Franc Steinman³ – Gašper Rak³ – Tom Bajcar⁴

¹ DHD Ltd, Digital Hydrodynamics, Slovenia

² Hidroinštitut, Institute for Hydraulic Research, Slovenia

³ University of Ljubljana, Faculty for Civil and Geodetic Engineering, Slovenia

⁴ University of Ljubljana, Faculty of Mechanical Engineering, Slovenia

Bottom-hinged flap gates on side weirs are often used for the regulation of flow diversion in case of water abstraction for a variety of needs. In this study, a new equation for the discharge coefficient of a bottom-hinged flap gate on a side weir was proposed on the basis of discharge measurements. The equation was divided into two parts. The first part covers the impact of the sharp-crested side weir and the second the influence of the position and the width of the flap gate. In this manner, the discharge coefficient can be calculated with other authors' equations for a sharp-crested side weir, which then must be multiplied by the new proposed coefficient. Very good agreement was found between the obtained discharge coefficients and the one calculated with the proposed equation. Furthermore, the results were compared with the equations of other authors for the discharge coefficients of sharp- and broad crested side weirs. The agreement was found to be very good. Additionally, measurements of water levels along the edge of the flap gate and measurements of the velocity field were carried out with a computer-aided visualization method. From these measurements, it was possible to show that the contraction of the water jet varies with the gate-opening angle. It was also found that the side weir with a flap gate has the most favorable hydrodynamic shape around the gate-opening angle of 33°, where the discharge coefficient reaches its maximum.

Keywords: side weir, discharge coefficient, flap gate, overflow gate, visualization method

Highlights

- A new coefficient is proposed for the correction of the discharge coefficient of a sharp-crested side weir due to the opening gate angle of a bottom-hinged flap gate on the side weir.
- Contraction of the water jet and the discharge coefficient of a side weir with a flap gate are dependent on the gate-opening angle of the flap gate on a side weir.
- The side weir with a flap gate has the most favorable hydrodynamic shape around the gate-opening angle of 33°, where the discharge coefficient reaches its maximum.
- The discharge coefficient of a flap gate on a side weir has its minimum at the gate-opening angle of 0°, where it can be considered as a broad-crested side weir.

0 INTRODUCTION

Side weirs are structures used for flow diversion in case of water abstraction for a variety of needs such as irrigation or for flood water diversion. The latter structures are also known as flood overflows and have proven to be highly useful for the diversion of flood water in wastewater treatment plants as well as for the diversion of water from river channels, for example, when excess water has to be diverted from a river channel to a retention area.

For the proper design of such structures, it is important to know the flow capacity of side weirs, which has already been investigated by various authors. If we define dQ as the flow through an infinitely small stripe ds along the side weir, the general equation for the specific flow over the side weir can be written as follows [1]:

$$q_s = -\frac{dQ}{ds} = \frac{2}{3}\sqrt{2g}C_d(h-p)^{3/2}, \quad (1)$$

where $(h-p)$ represents the overflow height over the side weir, g represents the gravitational acceleration, and C_d is an empirical coefficient. Several equations have been proposed for the calculation of the coefficient C_d for the sharp-crested side weir and for the broad-crested weir. Most of the authors have considered the impact of the inflow Froude number in their equation [2] and [3], some have also considered the impact of the overflow height [4] and [5], but only a few have taken into account the impact of the length of the side weir. The impact of the width of a broad-crested side weir has also been investigated [6] and [7]. Fig. 1 shows the geometric and hydraulic parameters

that have been proven to have the greatest impact on the coefficient C_d [2].

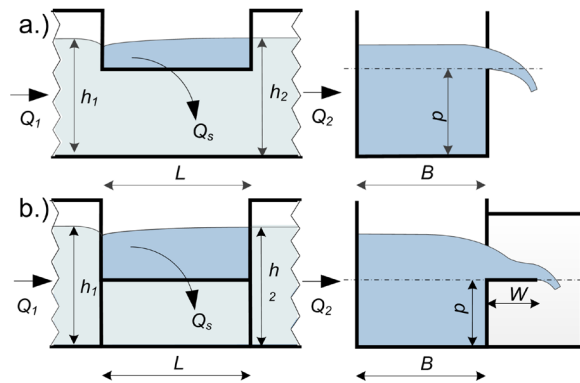


Fig. 1. Sketch of a) a sharp-crested rectangular side weir, and b) a broad-crested side weir

In Fig. 1, h_1 represents the water level of the approaching flow in the main channel, h_2 the water level of the outflow in the main channel downstream of the side weir, W the width of the flap gate or of the broad-crested side weir, B the width of the main channel, L the length of the side weir, Q_1 the discharge of the approaching flow in the main channel, Q_2 the discharge of the outflow in the main channel downstream of the side weir, and Q_s the discharge over the side weir.

The need for the regulation of the lateral discharge over the side weir often appears, for example, with the regulation of the water level in the reservoir in the emergence of a flood wave. Therefore, bottom-hinged flap gates are often used on side weir structures to regulate the amount of the lateral discharge over the side weir at different reservoir water levels.

Good knowledge about the discharge capacity of such structures is necessary for the appropriate design and operation of flap gates. Several hydraulic analyses of such gates on weirs have been made by various authors [8] and [9], although available studies of the discharge capacity of flap gates are virtually non-existent. Furthermore, the hydraulic conditions at such structures lack deep analyses, for example of the three-dimensional velocity field. In this paper, a new equation for the coefficient C_d of a flap gate on a side weir is proposed; in addition, measurements of the velocity field in the horizontal plane have been made to explain the obtained dependence of the C_d from the gate-opening angle φ . Fig. 2 shows the characteristic parameters of the flap gate on the side weir used in this study. W denotes the width of the flap gate and φ the gate-opening angle.

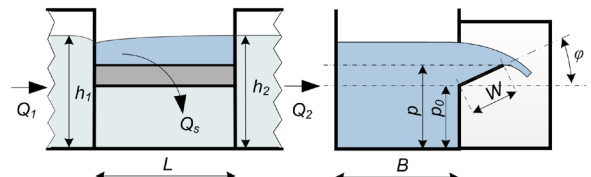


Fig. 2. Sketch of a rectangular side weir with a flat bottom - hinged flap gate

1 METHODS

Within the experimental work, discharge, water surface and velocity field measurements were performed. The discharge measurements were performed with the help of a triangular Thomson weir on the upstream end of the model (inflow of water into the model) and a rectangular weir that was placed inside of the channel, on the downstream end of the model (outflow of water out of the main channel). Since such a weir for the measurement of discharges, should be wider than 0.3 m, according to the ISO standard [10], a rating curve of the weir was obtained with the help of the upstream Thomson weir (which was in accordance with the ISO standard) and with the side weir closed. It was found that the correlation between the obtained rating curve and the one according to the ISO standard is very good, since the maximum difference in flow rates does not exceed the value of 1.4 % (for spill heights greater than 3.5 cm, for which the measurements were conducted).

In addition to the discharge measurements, the upstream water levels were also measured to determine a new equation for C_d . The water levels were measured with a point gauge of 0.1 mm precision. Furthermore, measurements of the velocity field in a horizontal plane located just above the edge of the flap gate were carried out. The measurements were made with the computer-aided visualization method based on the advection-diffusion equation. This method is implemented in ADMflow software, developed jointly by University of Ljubljana, Faculty of Mechanical Engineering and Abelium [11].

The method has been verified with a number of cases; it has already been used for the measurements of the velocity fields of a free surface flow specific for a case of a side weir. It was found that the most suitable tracer for the measurements in such cases are hydrogen bubbles, which can be produced with galvanization [12]. It has been shown that the uncertainty of the method is $\pm 5\%$ [11].

2 EXPERIMENTAL SET-UP

A physical model of the side weir with a bottom-hinged sharp edged flat flap gate was constructed and placed in a 6 m long rectangular channel with the width of 0.2 m. The flap gate was hinged on the sharp-crested side weir and supported with a threaded metal rod, which was then used to fine-tune the position of the flap gate (angle φ). A 0.25 mm thick copper wire was placed approximately 0.15 m upstream of the upstream edge of the side weir. The wire was attached to a specially designed fork, which was constructed out of a 2 mm thick electrically isolated wire. Both the thin wire and the fork were placed at an appropriate distance from the side weir; in this way the water flow in the area of the side weir was not disturbed. The thin copper wire could then be adjusted to the height at which the velocity field was measured at that particular time (the height position of the wire was adjusted to the height of the illuminated plane). At the same location (about 0.15 m upstream of the upstream edge of the side weir), a copper plate of negligible thickness (<1 mm) was placed on the bottom of the channel. The copper wire and the plate were connected to a power supply; in this way, a galvanization process started and hydrogen bubbles were produced, which served as a tracer.

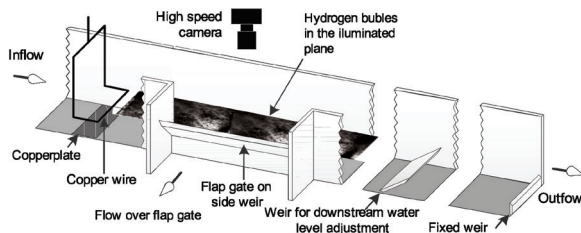


Fig. 3. A sketch of the established physical model and the measurement apparatus

The velocities were measured in the illuminated plane, 5 mm above the overflow edge of the gate. A height-adjustable weir was placed in the main channel about 1.5 m downstream of the downstream edge of the side weir, which served for the regulation of the downstream water in the main channel. The position of this weir influenced the upstream conditions and was required to obtain a variety of different Froude numbers and water levels, and thus affected the size of the lateral outflow over the side weir. In actuality, such a regulation would be represented with a gated weir in the river channel.

The fact that the impact of the surface tension is negligible at such model dimensions and that the main channel was already shown in previous studies [12], in

which the measurements of the hydraulic conditions at a side weir with a similar length as used in this study made in a 150 mm wide channel were additionally verified with the measurements made in a wider channel (0.5 m) with a longer side weir. The research showed a good correlation between the measurements in the narrow and wider channel.

In this study, various lengths L of the side weir (0.15 m, 0.2 m and 0.25 m) and various heights of the weir p (0.05 m, 0.075 m and 0.1 m) were considered. Furthermore, all lateral discharge measurements were made for different upstream Froude numbers F_1 (0.1 to 0.41) and different overflow heights h_{1-p} (0.03 m to 0.1 m), in which both were varied randomly. In all described variants, 7 different positions of the gate (different φ) were considered (0° , 10° , 20° , 33° , 45° , 70° and 90°).

A total of 380 measurements with different variants of the above-described parameters were carried out. In every measurement, the inflow and outflow discharges as well as the upstream and downstream water levels were obtained.

To confirm and explain the resulting dependence of C_φ from φ , additional velocity measurements were carried out. In order to investigate this dependence, all hydraulic parameters were fixed for all the additional measured variants. At all 7 variants, F_1 and h_{1-p} and the geometric properties (L , B , p) remained the same, only φ was varied (0° , 10° , 20° , 33° , 45° , 70° , and 90°). In addition to the velocity measurements in the horizontal plane, the upstream and downstream water levels and the water levels along the edge of the flap gate were measured for all 7 variants.

3 RESULTS

The analysis of the discharge coefficient C_d of the flap gate on a side weir has shown that C_d is highly dependent of the opening gate angle φ . The approximate trend of the variation of C_d with φ can be recognized if all the measured C_d against φ are placed in a graph (Fig. 4).

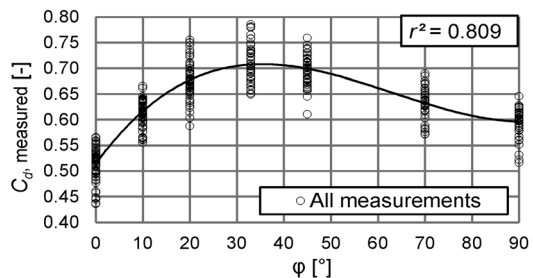


Fig. 4. From the measurements obtained C_d in dependence of φ

The trend approximately follows a third-degree polynomial function. In this case, the correlation factor r^2 is equal to 0.809. The fact that this trend follows a polynomial function was already shown [8] and [9]; however, their studies were made for flap gates on the weir that were placed perpendicular to the water flow and not on the side weir. Fig. 4 also shows the range of C_d values at each φ , which is between 10 % and 15 %. This range is the result of other influential hydraulic parameters of the water flow, such as F_1 and h_1 , and other influential geometric parameters, such as L and p . All of these parameters were also considered in the new equation for C_d of the flap gate on a side weir.

3.1 The New Equation for C_d

3.1.1 Equation Derivation

It was already shown that the C_d is mostly affected by the following ratios [2]:

$$C_d = f(h_1/p, L/B, F). \quad (2)$$

For the equation of C_d , a function was chosen in which the ratios from Eq. (2) were considered as the products of several power functions. Similarly, it was already shown that the C_d of a broad-crested side weir is, in addition to those already mentioned ratios from Eq. (2), also affected by the ratio [7]:

$$C_d = f(h_1 - p/W). \quad (3)$$

Because of the finding that the C_d in the case of a flap gate on a side weir is also affected by the value of the opening gate angle φ (Fig. 4), the latter was also included in the new equation as a polynomial function. A side weir with a flat, bottom-hinged flap gate can be considered to be a sharp-crested side weir without a gate, when the gate is fully closed (i.e. when $\varphi = 90^\circ$). Therefore, the new equation for C_d was divided into two parts. In the first part (C_{d0}), the influence of the ratios of the parameters from the Eq. (2) were captured, and in the second part (C_φ) the influence of φ and the ratios from Eq. (3) were captured. The divided equation reads:

$$C_d = C_{d0} \cdot C_\varphi, \quad (4)$$

where C_{d0} denotes the discharge coefficient of the sharp-crested side weir and C_φ denotes the influence of the flap gate.

Before the new equation was developed, an analysis of the dependence of C_d from the parameters in Eq. (3) was conducted. For this purpose, trend lines were produced, which are shown in Fig. 5.

It was found that the dependence of C_d on $(h_1 - p/W)$ is relative to φ , as the trend line in Fig. 4 for $\varphi = 0^\circ$ indicates a downward trend, while the trend line for $\varphi = 33^\circ$ indicates an upward trend. The downward trend at broad-crested weirs has already been shown by other authors ([6] and [7]), while the upward trend at $\varphi = 33^\circ$ is quite logical, since the effect of the gate width W decreases with the increase of the overflow height $(h_1 - p)$ and is at some point negligible (at $W/(h_1 - p) \ll 1$). The trend line for $\varphi = 90^\circ$ is approximately horizontal, as in this case this ratio has no effect on the C_d . The different trends of C_d in dependence on the ratio $W/(h_1 - p)$ at different values of φ were captured in the new equation for C_d with an additional exponent in C_φ .

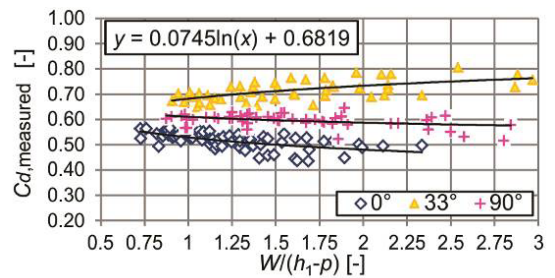


Fig. 5. Measured C_d in dependence of the ratio $W/(h_1 - p)$

A similar equation was already produced [6] for the broad-crested weir, where the ratio $W/(h_1 - p)$ was used as an exponent. However, in our case a logarithmic function was used for the additional exponent instead of a power function, as it was found to suit better the measured data, as well as such a function is quite logical, because it causes the coefficient C_d to stabilize from a certain value of the ratio $W/(h_1 - p)$ on. The proposed form of the new equation for the C_d of a bottom-hinged flap gate on a side weir is as follows:

$$C_d = a \left(\frac{h_1}{p} \right)^b (F_1)^c \left(\frac{L}{B} \right)^d \cdot (f \cdot \phi^j + g \cdot \phi^k + h \cdot \phi^l + i)^{m \cdot \ln(W/(h_1 - p)) + n}, \quad (5)$$

where φ is given in radians and the coefficients $a, b, c, d, f, g, h, i, j, k, l, m, n$ represent unknowns, which were determined on the basis of all 380 measurements and with the use of the generalized reduced gradient (GRG) method. Table 1 shows the obtained values for all unknowns.

With the parameters a to n , the correlation factor between the values that were obtained from the measurements and the values that were calculated from Eq. (5) is C_d , is $r^2 = 0.856$.

Table 1. Values of the unknowns in Eq. (5)

a) Unknowns a to g						
A	b	c	d	f	g	
0.482	0.023	-0.080	0.150	0.3086	-1.7499	
b) Unknowns h to n						
h	i	j	k	l	m	n
1.5359	0.9423	2.0996	1.4039	1.1314	2.7	2.0

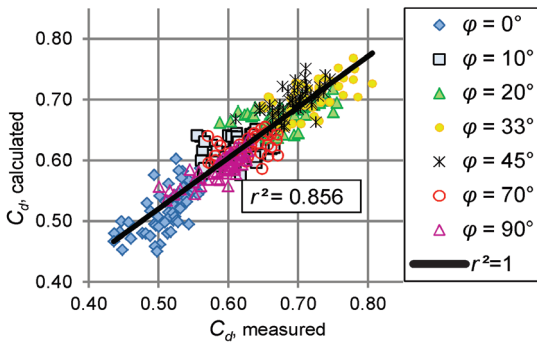


Fig. 6. Correlation between the measured and the calculated values of C_d

Furthermore, the average difference between these values does not exceed 3.2 %, the maximal difference does not exceed 13.9 %, and the standard deviation is 0.06, which is similar to what other authors found in their studies [2]. Fig. 6 shows the correlation between the measured and the calculated values of C_d .

According to Eq. (3), Eq. (4) can be divided into two parts:

$$C_{d0} = a \left(\frac{h_1}{p} \right)^b (F_1)^c \left(\frac{L}{B} \right)^d, \quad (6)$$

$$C_\phi = (f \cdot \phi^j + g \cdot \phi^k + h \cdot \phi^l + i)^{m \cdot \ln(W/(h_1-p)) + n}, \quad (7)$$

when the value ϕ is 1.5708 rad, which is equivalent to the angle 90° , Eq. (7) reduces to the value of 1, regardless to the values W , h_1 or p . Thus, Eq. (3) reduces itself to $C_d = C_{d0}$, which is entirely logical, as the side weir with a flap gate in a fully closed gate position (i.e. at $\phi = 90^\circ$) is equivalent to a sharp-crested side weir and the ratio $W/(h_1-p)$ does not have any impact on the value of C_d .

3.1.2 Verification Using Other Experimental Data for Sharp-Crested Weirs

The comparison of our measurements of C_d for the gate angle $\phi = 90^\circ$ with the calculated values from

equations developed from other authors showed very good agreement. Furthermore, the comparison of our measurements of C_d for the gate angle $\phi = 90^\circ$ with those calculated after Eq. (6) also showed very good agreement, as the average difference does not exceed 2.8 %. The best agreement of our measurements with the equations from other authors was found by the comparison with the study from [4], in which the side walls in the side channel were also considered, as was done in our case. Furthermore, the measured values are in good agreement with the calculated values according to the equation in [13], where the average difference does not exceed 3.7 % and the maximum difference 8 %. The calculated values from the equations of other authors and our measured values of C_d are mainly located within the 10 % range [14] and [15]; however, it must be noted that other authors did not consider the side walls in the side channel. The agreement of our measured values of C_d and the calculated values by the equation in [5] and [16] is out of the 10 % range. However, it should be noted that the trends are very similar. Furthermore, the values calculated from the equations of other authors differ; for example, the mean difference between [5] and [15] is 35 %, and the difference between [3] and [5] is more than 50 % (Fig. 7).

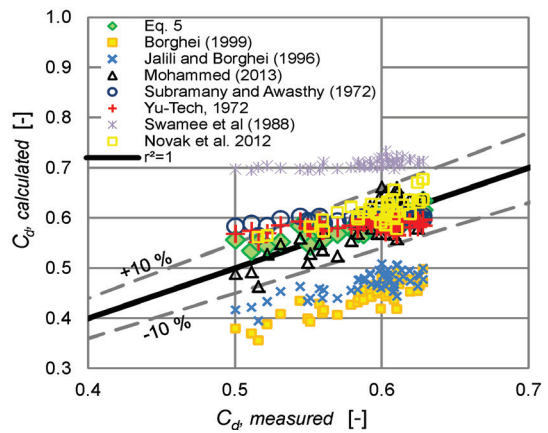


Fig. 7. Comparison of the measured C_d at $\phi = 90^\circ$ and calculated from the Eq. (6) and from equations of other authors

3.1.3 Verification Using Other Experimental Data for Broad-Crested Weirs

As already mentioned, the side weir with the position of the flap gate at $\phi = 0^\circ$ can be considered to be a broad-crested side weir, for which the width of the gate W represents the width of the broad-crested weir. Therefore, at values of $\phi = 0^\circ$, Eq. (5) reduces

to an equation for a broad-crested side weir, and the coefficient C_ϕ is in this case equal to:

$$C_\phi(\phi = 0^\circ) = C_W = i^{m \cdot \ln(W/(h_1-p)) + n} \quad (8)$$

where C_W denotes the correction factor for C_d for the case of a broad-crested side weir. The comparison of the calculated coefficients C_W after Eq. (8) for the measured variants where the gate was fully opened ($\phi = 0^\circ$) with the calculated values after the equations for a broad-crested weir from other authors, showed good agreement. From the correlation of the values calculated with Eq. (8) and values calculated after the equation in [7], a correlation factor r^2 of 0.97 was obtained and from the correlation with [6] a value of $r^2 = 0.95$. Furthermore, in the first case, the average difference is less than 1.3 % and in the second, even lower than 1 %, while the maximum difference does not exceed 5 % in either one. It should be noted that the equation in [7] was made for a broad-crested side weir, and the equation in [6] was made for a broad-crested weir. Fig. 8 shows the correlation between the calculated values according to Eq. (8) and according to other authors for all measured variants where the gate was fully opened ($\phi = 0^\circ$).

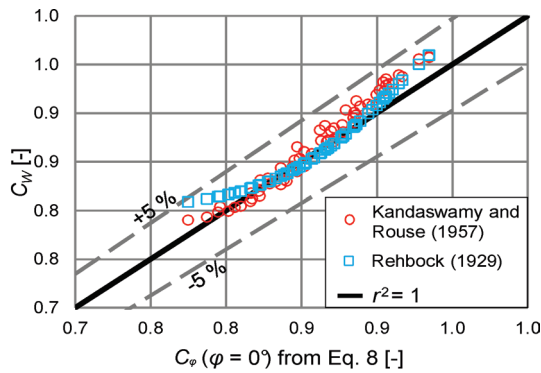


Fig. 8. Correlation between C_ϕ according to the Eq. (8) and the calculated C_W according to other authors for all measurements with the flap gate fully opened ($\phi = 0^\circ$)

3.1.4 Verification Using Other Experimental Data for Bottom-Hinged Flap Gates on Weirs

Fig. 9 shows the dependence of C_ϕ on ϕ according to Eq. (7) for different ratios $W/(h_1-p)$ which vary from 0.6 to 2.8, which is for the range for which the measurements were conducted. It can be seen that according to Eq. (7) the trend of C_ϕ in dependence of $W/(h_1-p)$ turns at $\phi = 7.5^\circ$.

According to Eq. (7), C_ϕ is approximately 1 when the $W/(h_1-p) < 0.5$ (i.e. in the case when the overflow height (h_1-p) is two times greater than the width of

the gate W). Therefore, in this case, the impact of the flap gate on C_d is negligible.

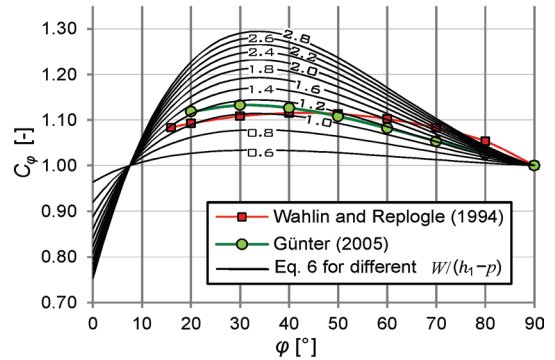


Fig. 9. Dependence of C_ϕ on $W/(h_1-p)$ according to the Eq. (7) and the comparison of C_ϕ with the equations from other authors

A much greater impact of the flap gate on C_d was found to be at higher values of the ratio $W/(h_1-p)$ (i.e. in the case when the overflow height (h_1-p) is smaller than the width of the flap gate W), where C_ϕ reaches a value of 1.3 at the angle $\phi = 33^\circ$. Fig. 9 also shows that the calculated values of C_ϕ according to Eq. (7) matches very well with the formula stated by Günter in his book about weirs [8]. The agreement of C_ϕ according to Eq. (7) and the equation in [9] was found to be less good, but still satisfactory. However, the authors did not consider the impact of the ratio $W/(h_1-p)$ on C_ϕ ; moreover, those studies were made for weirs and not for side weirs.

3.2 Verification with Additional Measurements

In order to verify the obtained equation for C_ϕ , additional measurements were carried out, in which (h_1-p) and F_1 were fixed for all measured variants and only ϕ was varied for 7 different opening gate angles ϕ . In this way, it was possible to assess the effect of ϕ on C_ϕ and remove the influence of other parameters. First, the coefficients C_d were obtained from the measurements. Then, using the value obtained for C_d at the angle of 90° , the coefficients C_ϕ were calculated. All geometric and other measured hydraulic parameters from the conducted additional measurements are listed in Table 2.

The agreement of the measured values of C_d and the calculated with Eqs. (5) and (7) was found to be good, as the maximum relative difference between them is 4 % for C_d and 2.8 % for C_ϕ .

The calculated C_ϕ according to Eq. (7), and the obtained C_ϕ from the additional measurements are given in Fig. 10.

Table 2. Geometric and other measured hydraulic parameters for the additional measurements

φ [°]	Q_l [l/s]	Q_s [l/s]	p_0 [cm]	h_1-p [cm]	L [cm]	B [cm]	F_1 [-]
0	5.92	1.9	7.5	3.54	20	20	0.26
10	6.85	2.36	7.5	3.52	20	20	0.26
20	7.54	2.68	7.5	3.51	20	20	0.26
33	8.77	2.83	7.5	3.54	20	20	0.26
45	9.70	2.74	7.5	3.50	20	20	0.26
70	11.02	2.47	7.5	3.53	20	20	0.26
90	11.40	2.42	7.5	3.68	20	20	0.24

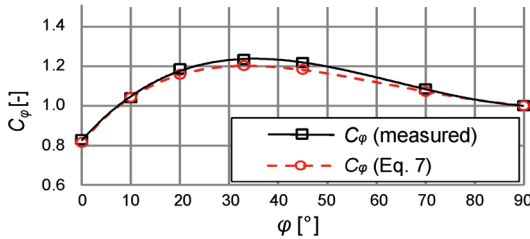


Fig. 10. Comparison of the values obtained from measurements and with the Eq. (7) calculated values of C_φ

From the comparison of the values obtained from the measurements and the values calculated from Eq. (7) for the examples of the additional measured variants, a correlation factor $r^2 = 0.99$ was found. Therefore, we can conclude that Eqs. (5) and (7) give adequate results.

4 DISCUSSION OF THE OBTAINED C_d

4.1 Water Surface and Flow Area

The lower values of C_φ in the case when the flap gate is fully opened can be explained by the fact that such a position is similar to a broad-crested side weir, where the flow rate over the weir is smaller than by sharp-crested side weirs, due to a different contraction of the water jet. By closing the gates (by increasing φ), the contraction of the water jet changes and it becomes much more similar to the water jet that occurs at sharp-crested side weirs. An example of the different contractions of the water jet at sharp- and broad-crested side weirs is shown in Fig. 1. To confirm this hypothesis, the flow area of the cross-section at the edge of the flap gate was obtained from the additional measured variants, where the water levels were measured using a point gauge.

Fig. 11 shows that the flow area A , in spite of the same inflow conditions (h_1-p) and F_1 , increases rapidly at angles from $\varphi = 0^\circ$ to $\varphi = 33^\circ$ (over 50%),

while at angles from $\varphi = 33^\circ$ to $\varphi = 90^\circ$ it increases only slightly (less than 10%).

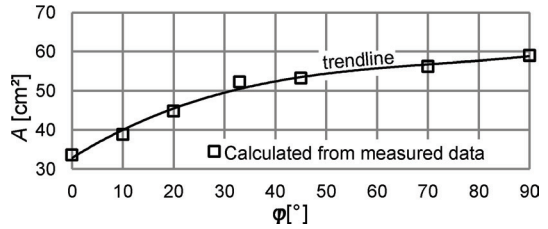


Fig. 11. The flow area in the cross-section at the edge of the flap gate in dependence of φ , with the same inflow conditions ($F_1 = 0.26$, $h_1-p = 3.5$ cm)

4.2 Velocity Field

According to the obtained flow areas A at different φ , shown in Fig. 11, and according to the obtained discharge for this same measured variants Q_s , the dependence of the average transverse (according to the axis of the main channel) velocities from the opening gate angle φ should be obtained from Eq. (9), shown in Fig. 12.

$$v_{y,q} = Q_s / A. \tag{9}$$

In order to confirm the resulting average velocity component $v_{y,q}$ and thus the measured values of A and Q_s , measurements of the velocity field were carried out with the computer-aided visualization method in the horizontal plane 5 mm above the overflow edge of the flap gate (this plane is denoted P), for all 7 additional measured variants.

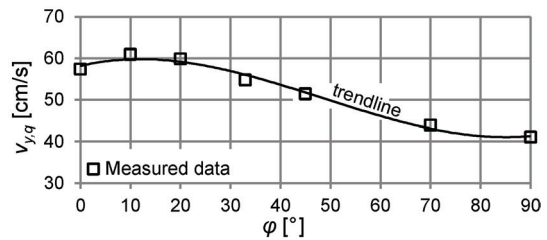


Fig. 12. From Eq. (9) calculated average y velocity components $v_{y,q}$ on the cross-section at the edge of the flap gate in dependence of φ

It can be seen from Fig. 13 that the measured vectors at $\varphi = 33^\circ$ (Fig. 13a) are much more perpendicularly oriented to the edge of the flap gate than the vectors for $\varphi = 90^\circ$ (Fig. 13b). Because of this, the velocity components in the y direction are in general greater in the first two cases. This is in good

agreement with the velocity distribution seen in Fig. 12.

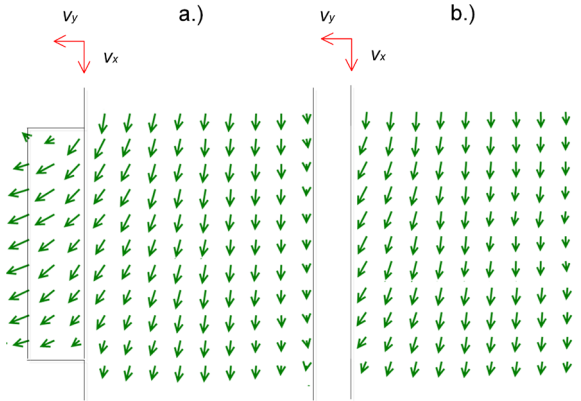


Fig. 13. The measured velocities in the horizontal plane P with the inflow conditions F_1 and $(h_1 - p)$, for a) $\varphi = 33^\circ$ and b) $\varphi = 90^\circ$

To support the above-described explanation with quantitative values, both velocity components were therefore spatially averaged over the cross-section of the flow area along the overflow edge of the flap gate. Because the computer-aided visualization method provides instantaneous velocities, the values also had to be time-averaged across a time window of 30 frames, which were captured with a high-frequency camera with a recording rate 300 frames per second. In the horizontal plane P , spatially and time-averaged velocities are denoted with $v_{y,P}$.

Fig. 14 shows a comparison of the measured velocities $v_{y,P}$ and the velocities $v_{y,q}$ calculated with Eq. (9). It can be seen that the maximal difference between them is about 10 %, which is within the range of uncertainty of all used measuring methods, considering that the error of the point gauge, used for the measurement of A and the error due to the interpolation of water levels between the measured points is around 2 %, the error of the discharge measurements does not exceed 3 %, and the error of the computer-aided visualization method was shown to be around 5 % [11].

It should be noted that for a more precise determination of the averaged y velocity component, velocity measurements in horizontal planes that are higher than the measured plane P would be needed, as most likely the velocity profile at the edge of the flap gate is not constant along the vertical. The biggest impact of the height-distributed velocity profile is most likely to occur at higher φ , where the height of the water jet at the edge of the flap gate is the greatest. It is precisely at this gate-opening angle where the maximal differences between the measured velocities

$v_{y,P}$ and the calculated velocities $v_{y,q}$ appear. However, because the purpose of these measurements in this study was only to verify the trend of the obtained velocities from Fig. 12, the accuracy of the conducted measurements was completely satisfactory. The correlation between $v_{y,P}$ and $v_{y,q}$ shows a very good agreement, since r^2 is 0.982.

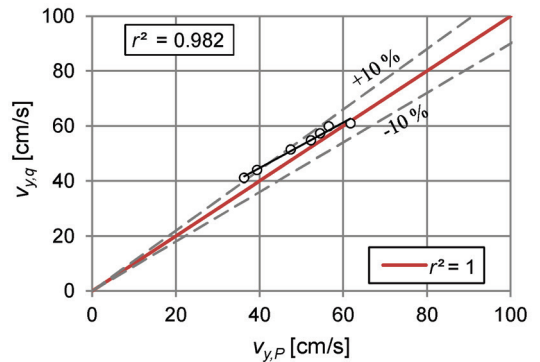


Fig. 14. Comparison of $v_{y,P}$ and $v_{y,q}$

5 CONCLUSIONS

In this study, a new equation for the discharge coefficient C_d of a bottom-hinged flap gate on a side weir was proposed on the basis of 380 measurements. The equation was divided into two parts: the first part covers the impact of the sharp-crested side weir, while the second part covers the influence of the position φ and width W of the flap gate. In this way, the coefficient C_d can also be calculated with the help of an equation for a sharp-crested side weir from another author, which then has to be multiplied by the coefficient C_φ that represents the second part of the proposed equation.

For the verification of the proposed equation for C_φ , additional discharge measurements were carried out with the same inflow conditions, F_1 and $(h_1 - p)$, and different gate-opening angles φ . The analysis showed very good agreement with the proposed equation.

For all the additionally measured variants, measurements of water levels along the edge of the flap gate and measurements of the velocity field in the horizontal plane P , which is located just above the edge of the gate, were carried out with a computer-aided visualization method. From these measurements, it was possible to show that the contraction of the water jet and the flow area of the vertical cross-section along the edge of the gate vary with the gate-opening angle φ . The latter has evidently a significant impact on the flow over the side weir with flap gates.

Furthermore, the measurements of the velocity field helped to explain the obtained dependence of C_φ from φ . It was found that the position of the flap gate has a significant impact on the discharge coefficient C_d , as the hydrodynamic shape of the weir changes with the position of the flap gate. (among others factors). It was also found that the side weir with a flap gate has the most favorable hydrodynamic shape around the gate-opening angle $\varphi = 33^\circ$, where the coefficient C_d reaches its maximum.

The proposed equation will contribute to a better and more accurate design of overflow spillways with flap gate regulation, and it will also contribute to more appropriate operation of such structures, for which it is very important to know the flow capacity at different operating stages. In addition, the results will be very useful for the calibration and verification of two- and three-dimensional numerical models, which have become increasingly used for hydraulic analysis of such structures in recent years [17] and [18].

In this study, a flat flap gate without the impact of the downstream water level in the side channel was investigated. In further research, it would be very useful to analyze the dependence of the discharge coefficient C_d from the flap gate shape form (different curvatures) and the height of the downstream water level in the side channel. Furthermore, it would be interesting to compare the obtained results with the results of a numerical model, which in this case would have to be a three-dimensional model with a suitable turbulence model.

6 ACKNOWLEDGEMENTS

This work is in part supported by the Slovenian Research Agency (ARRS), grant L2-4270.

7 REFERENCES

- [1] De Marchi, G. (1934). Essay on the performance of lateral weirs. *L'Energia Elettrica Milan*, vol. 11, no. 11, p. 849-860.
- [2] Singh, R., Manivannan, D., Satyanarayana, T. (1994). Discharge coefficient of rectangular side weirs. *Journal of Irrigation and Drainage Engineering*, vol. 120, no. 4, p. 814-819, DOI:10.1061/(ASCE)0733-9437(1994)120:4(814).
- [3] Swamee, P.K., Pathak, S.K., Mohan, M., Agrawal, S.K., Ali, M.S. (1994). Subcritical flow over rectangular side weir. *Journal of*

- Irrigation and Drainage Engineering*, vol. 120, no. 1, p. 212-217, DOI:10.1061/(ASCE)0733-9437(1994)120:1(212).
- [4] Mohammed, A.Y. (2013). Numerical analysis of flow over side weir. *Journal of King Saud University - Engineering Sciences*, vol. 27, no. 1, p. 37-42, DOI:10.1016/j.jksues.2013.03.004.
- [5] Borghei, S., Jalili, M., Ghodsian, M. (1999). Discharge coefficient for sharp-crested side weir in subcritical flow. *Journal of Hydraulic Engineering*, vol. 125, no. 10, p. 1051-1056, DOI:10.1061/(ASCE)0733-9429(1999)125:10(1051).
- [6] Rehbock, T. (1929). Discussion of "Precise measurements" by Turner K., B. Trans., vol. 93, p. 1143-1162.
- [7] Kandaswamy, P.K., Rouse, H. (1957). Characteristics of flow over terminal weirs and sills. *Journal of the Hydraulics Division*, vol. 83, no. 4, p. 1-13.
- [8] Günter, P. (2005). *Überfälle und Wehre: Grundlagen und Berechnungsbeispiele*. Vieweg Verlag, Wiesbaden.
- [9] Wahlin, B.T., Replogle, J.A. (1994). *Flow Measurement Using an Overshot Gate*, UMA Engineering, Inc., Washington.
- [10] ISO 1438:2008(E). (2008). *Hydrometry - Open Channel Flow Measurement Using Thin-Plate Weirs*. International Organization for Standardization, Geneva.
- [11] Bajcar, T., Širok, B., Eberlinc, M. (2009). Quantification of flow kinematics using computer-aided visualization. *Strojniški vestnik - Journal of Mechanical Engineering*, vol. 55, no. 4, p. 215-223.
- [12] Novak, G., Steinman, F., Müller, M., Bajcar, T. (2012). Study of velocity field at model sideweir using visualization method. *Journal of Hydraulic Research*, vol. 50, no. 1, 129-133, DOI:10.1080/00221686.2011.648766.
- [13] Novak, G., Kozelj, D., Steinman, F., Bajcar, T. (2013). Study of flow at side weir in narrow flume using visualization techniques. *Flow Measurement and Instrumentation*, vol. 29, no. 3, p. 45-51, DOI:10.1016/j.flowmeasinst.2012.10.008.
- [14] Yu-Tech, L. (1972). Discussion: Spatially varied flow over side weir. *Journal of the Hydraulics Division*, vol. 98, no. 11, p. 2046-2048
- [15] Subramanya, K., Awasthy, S.C. (1972). Spatially varied flow over side weirs. *Journal of the Hydraulics Division*, vol. 98, no. 1, p. 1-10.
- [16] Jalili, M.R., Borghei, S.M. (1996). Discussion: Discharge coefficient of rectangular side weir. *Journal of Irrigation and Drainage Engineering*, vol. 122, no. 2, p. 132, DOI: 10.1061/(ASCE)0733-9437(1996)122:2(132).
- [17] Milési, G., Causse, S. (2014). 3D numerical modeling of a side-channel spillway. Gourbesville, P., Cunge, J., Caignaert, P. (eds.). *Advances in Hydroinformatics*, Springer Singapore, p. 487-498, DOI:10.1007/978-981-4451-42-0_39.
- [18] Namaee, R.M., Rostami, M., Jalaledini, S., Habibi, M.A. (2014). 3-dimensional numerical simulation of flow over a broad-crested side weir. Gourbesville, P., Cunge, J., Caignaert, P. (eds.). *Advances in Hydroinformatics*, Springer Singapore, p. 511-523, DOI:10.1007/978-981-4451-42-0_41.

Cohesive Zone Parameters Selection for Mode-I Prediction of Interfacial Delamination

Mohsen Moslemi^{1,*} – Mohammadreza Khoshrovan²

¹ Young Researchers and Elite Club, Tabriz Branch Islamic Azad University, Tabriz, Iran

² University of Tabriz, Department of Mechanical Engineering, 5166614766, Tabriz, Iran

In order to determine the normal cohesive strength of composite laminates, a new test methodology was proposed. The values of cohesive zone parameters (the cohesive strength and the separation energy) for mode I interlaminar fracture of E-glass/epoxy woven fabrication were computed from a series of experimental tests. Cohesive zone model simulation based on interface finite elements was conducted. A modified form of the Park-Paulino-Roesler (PPR) traction-separation law together with a bilinear mixed-mode damage model was used to simulate the damage processes, using Abaqus cohesive elements. The numerical results were compared with experimental tests and confirmed the adequacy of normal cohesive strength. To ensure the sufficient dissipation of energy that successfully predicts delamination onset and propagation, cohesive zone length and minimum number of cohesive elements at cohesive zone length were determined. Interfacial penalty stiffness and the resistance curve of the composite specimen were also computed. The results show that the modified PPR model accurately simulates the fracture process zone ahead of the crack tip as compared to the bilinear model.

Keywords: cohesive zone model, delamination, normal cohesive strength, finite element prediction

Highlights

- Interlaminar Cohesive strength of composite material was determined.
- Cohesive zone modelling of delamination.
- Bilinear and modified PPR damage models.
- Experimental estimation of resistance curve.
- Cohesive zone length estimation.

0 INTRODUCTION

Delamination is a defect type that frequently occurs in laminated composite materials, described as the separation of a layer or group of layers from their adjacent ones, due to out-of-plane shear loads. Delamination usually initiates from discontinuities, such as matrix cracks and free edges, or manufacturing faults, such as embedded defects and machining process such as water-jet cutting [1]. Therefore, it is important to detect and analyse the progressive growth of delamination in order to predict the performance and to improve reliable and safe designs. Ultrasonic C-scan is one of the most efficient techniques for tracing delamination in laminated composite materials [2]. Mode-I interface cracking is one of the most frequently modes of delamination in composite layered materials that is due to the loss of cohesion between layers of material.

The delamination resistance of polymer matrix composites has been extensively investigated in the framework of fracture mechanics [3]. In order to model crack propagation, it was assumed that the delamination propagates when the available strain energy release rate is greater than or equal to a critical value, which is considered to be a mechanical

parameter of the interface. Techniques such as the virtual crack closure (VCC), the J-integral, and the virtual crack extension are some of the most prevalent procedures that are used to predict delamination growth. These techniques are used to compute the distribution and components of the strain energy release rate. However, there are some difficulties when these techniques are performed using finite element codes. Another method to the numerical modelling of the delamination growth can be developed within the framework of damage mechanics. Models formulated according to damage mechanics are based on the concept of the cohesive crack model, which considers a zone of vanishing thickness ahead of the crack front in order to describe more realistically the fracture nature without the use of stress singularity. The cohesive zone model was first developed by Dugdale [4], who demonstrated the concept that stresses in the material are confined by the yield stress and that a thin plastic zone is generated in front of the crack tip. Barenblatt [5] proposed a cohesive zone concept to study the fracture nature of brittle materials and to introduce a separation mechanism at the atomic scale in order to describe the real separation of materials, and to remove stress singularity at the crack tip. Hillerborg et al. [6] suggested a model similar to the

*Corr. Author's Address: Young Researchers And Elite Club, Tabriz Branch Islamic Azad University, Tabriz, Iran, m.moslemi@tabrizu.ac.ir

Barenblatt model. Their model allowed for existing cracks to grow as well as the initiation of new cracks. A cohesive zone model was frequently used to the model fracture analysis of a different variety of materials such as metals, polymers, concrete [7], ceramics, functionally graded materials [8], and fibre-reinforced materials [9]; its range of applications will continue to expand. An important issue in conjunction with the use of the cohesive zone model is the specification of the traction-separation law. In particular, the related fracture parameters, such as cohesive strength and fracture toughness, as well as the shape of the traction-separation law, must be determined. In the case of the traction-separation law, there are some models in the literature that can be used. For example, traction-separation based on an exponential form, a trapezoidal form and the bilinear form of Zhang and Paulino [8] are traction-separation laws that have been widely adopted. Since there are no available standardized tests and due to the existence of some difficulties corresponding to the direct measurement of the these parameters, in most cases they are determined by the comparison of a measured fracture property with numerical predictions based on an idealized cohesive zone model, cf. [7], [10] and [11]. However, cohesive strength and fracture toughness are found to have higher importance in comparison to the specific traction-separation shape that chosen for the cohesive zone modelling. Turon et al. [11] proposed a methodology to estimate the constitutive parameters for the finite element simulation of progressive delamination using a bilinear cohesive zone model. According to their methodology, the cohesive strength is proportional to the length of the cohesive zone, and this parameter should be modified with respect to the cohesive zone length. It suggests that as the cohesive strength decreases, the length of the cohesive zone should be artificially lengthened to ensure that it spans enough elements of a given size. Yuan and Li [12] investigated the effects of the cohesive law on ductile crack propagation and recommended obtaining realistic computational results; the cohesive law must be defined with proper parameters.

The objective of this research is to provide a suitable methodology for the fracture characterization of delamination under pure mode I loading. In this paper, a simple structure test is proposed to compute the normal interlaminar cohesive strength of composite laminates. The values for the critical mode I strain energy release rate (G_{Ic}) and mode-I cohesive strength (σ_{Ic}) were computed at room temperature. These parameters and assumed damage models, including modified PPR model [13] and triangular traction law,

were used with the Abaqus COH3D8 cohesive element to simulate bond line failure in structures made from E-glass/Epoxy specimen. The resistance curve of the composite specimen computed using the experimental method and a guideline methodology was proposed for selection of mode I cohesive zone length and the minimum required number of element in the cohesive zone length to obtain successful prediction of the delamination onset and propagation.

1 COHESIVE ZONE MODEL THEORY

Cohesive damage zone models relate traction to separation at an interface where a crack may initiate. Crack initiation is related to the cohesive strength, i.e., the maximum traction on the traction-separation law. When the area under the traction-separation law reaches the fracture toughness, the traction declines to zero and new crack surfaces are generated. This phenomenon is shown in Fig. 1 for two different types of traction-separation law.

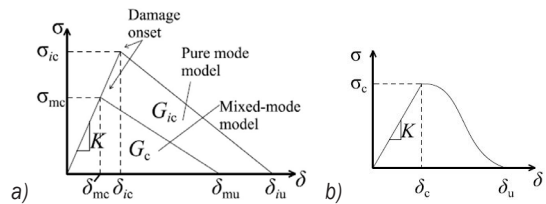


Fig. 1. Traction-separation law
a) triangular model b) modified PPR model

Fracture simulation of materials using cohesive elements requires substantial experience for determining the mesh requirements and the accurate values of parameters that characterize the traction-separation law. In this work, in order to simulate Mode-I fracture of E-glass/epoxy woven composite laminate using cohesive elements, two types of traction separation law, including mixed-mode Triangular traction-separation response and modified PPR model, which is potential-based model, were used and compared to experimental results. The objective is to determine an appropriate methodology to predict interlaminar crack growth in composite laminates. As shown in Fig 1, the subscript m referred to mixed mode and subscript c and u referred to critical and ultimate (failure) values, respectively, and $i = I, II$ and III referred to pure modes of fracture. The area under the curves represents the corresponding critical strain energy. In order to determine the mixed-mode traction-separation law, the properties required to be defined are the three critical strain energy release rates (G_{Ic}), the penalty stiffnesses (K_i) and the

cohesive strengths (σ_{ic}). In the present work, Mode III is assumed to be identical to Mode II, so that the shear strengths in the two orthogonal directions, σ_{IIc} and σ_{IIIc} also critical strain energies G_{IIc} , G_{IIIc} are equal. In the case of the simulation of Mode-I fracture, in order to predict delamination onset, analysis is more sensitive to the parameters σ_{Ic} and G_{Ic} than other interfacial properties. Therefore, in this work, the double cantilever beam (DCB) test and the normal cohesive strength (NCS) test were carried out to determine G_{Ic} and σ_{Ic} , respectively. Other fracture parameters were determined by the calibration of cohesive parameters. In other words, numerical results are fit with experimental results according to the methodology described in [7], [10] and [11].

1.1 Damage Initiation Criterion

As shown in Fig. 1, the initial response of the cohesive elements at each damage model is based on linear elastic fracture mechanics (LEFM) and is assumed to be linear until a crack initiation criterion is satisfied. The penalty stiffness, K_i , of each traction-separation response law that relates traction to the separation of cohesive elements before crack initiation is defined as below:

$$K_i = \frac{\sigma_{ic}}{\delta_{ic}}, \quad (1)$$

where $i = I, II$ and III is fracture modes, σ_{ic} and δ_{ic} are the cohesive strength and critical separation of pure modes of fracture, respectively. In the present work, the penalty stiffness for all modes of fracture are considered to be the same, i.e., $K_I = K_{II} = K_{III} = K$. Several methodologies have been proposed to determine the penalty stiffness of cohesive elements. The magnitude of the penalty stiffness must be high enough to avoid interpenetration of the crack surfaces and to avoid artificial compliance from being defined into the model by the cohesive elements. However, a more than enough value can lead to numerical problems. Turon, et al. [11] assumed that whenever the through-the-thickness Young's modulus of the adjacent sub-laminate, E_3 , is small enough compared to $K \times t$, the effective elastic properties of the material will not be affected by the cohesive face. Where t is the thickness of adjacent sub-laminate of composite specimen. Therefore, an equation to calculate the interface stiffness for Mode I is suggested, as mentioned below:

$$K = \alpha \cdot \frac{E_3}{t}, \quad (2)$$

where α is a parameter larger than 1. Turon et al. [11] recommended considering $\alpha = 50$. This value is used for derivation of the penalty stiffness in the analysis presented in this work. After the linear part of the constitutive law, traction at crack tip reaches its maximum value and consequently damage initiates. In order to simulate delamination onset in cohesive elements, there are four well-known crack initiation criteria: maximum stress, quadratic stress, maximum strain and quadratic strain criterion. In this analysis, the quadratic stress criterion that is expressed in Eq. (3) was used. Under mixed-mode loading, an interaction between modes must be taken into account. This criterion model readily takes into account the interaction of the traction components in the prediction of damage onset. Moreover, due to the high sensitivity of failure initiation to the strain and displacement, a stress-based criterion gives an accurate failure prediction as compared to other models, such as strain-based or displacement-based criteria. The quadratic stress criterion is defined as:

$$\left\{ \frac{\langle \sigma_z \rangle}{\sigma_{Ic}} \right\}^2 + \left\{ \frac{\tau_{xz}}{\tau_{IIc}} \right\}^2 + \left\{ \frac{\tau_{yz}}{\tau_{IIIc}} \right\}^2 = 1, \quad (3)$$

where x, y, z refer to Cartesian coordinate as shown in Fig. 4a. The Macaulay bracket, $\langle \rangle$, states that the compressive stress does not contribute to crack onset. Whenever the damage initiation criterion of Eq. (3) for the cohesive element is satisfied, the stiffness of the element is declined according to the corresponding constitutive law that is illustrated in Fig. 1.

1.2 Damage Propagation Criterion

After damage initiation, the softening procedure occurs. This procedure is governed by the corresponding traction separation law as below.

1.2.1 Bilinear Traction-Separation Model

As shown in Fig. 1a, in the mixed-mode constitutive law, σ_{mc} and δ_{mc} represent the cohesive strength and critical separation (separation at which crack initiates), respectively. Moreover, δ_{mu} refers to the separation at which failure occurs. The softening relation of cohesive elements that are governed by bilinear constitutive law can be expressed as:

$$\sigma_i = (1-d)K_i\delta_i, \quad (4)$$

where d is a variable that relates damage condition, which has the magnitude $d = 0$ when the interface

is undamaged, and the magnitude $d = 1$ when the interface is completely fractured. In numerical analysis of damage evolution, there are two crack evolution criteria: energy- and displacement-based. In the analysis presented herein, the energy-based Benzeggagh and Kenane (BK) [14] damage evolution criterion was used, as expressed in Eq. (5).

$$G_c = G_{Ic} + (G_{IIc} - G_{Ic}) \left(\frac{G_{shear}}{G_T} \right)^\eta \quad (5)$$

In Eq. (5), η referred to the BK material parameter, $G_{Shear} = G_{II} + G_{III}$ and $G_T = G_I + G_{II} + G_{III}$.

1.2.2 Modified PPR Model

In this model, the traction force in the interface is obtained by differentiating a potential function with respect to the interface separation. Fig. 1b shows the typical modified PPR traction-separation law of cohesive zone modelling. Park et al. proposed this potential based model for mixed mode fracture [15]. This law can be used for a wide variety of ductile and brittle fractures. Since it behaves nonlinearly prior to damage, it is required to develop a user defined element in ABAQUS for this model. Bhattacharjee et al. [13] developed a modified version of the PPR model for analysis of tearing in thin soft materials. In their model, as with the triangular constitutive law, a linear elastic response was assumed before damage initiation ($\delta < \delta_c$). Therefore, this modified version of the PPR model allows for a straightforward implementation of the model in the commercial finite element code ABAQUS, using tabular capability. After damage initiation, the softening relationship in this model can be expressed as [13]:

$$\sigma = A \left[w \left(1 - \frac{\delta}{\delta_u} \right)^\alpha \left(\frac{w}{\alpha} + \frac{\delta}{\delta_u} \right)^{w-1} - \alpha \left(1 - \frac{\delta}{\delta_u} \right)^{\alpha-1} \left(\frac{w}{\alpha} + \frac{\delta}{\delta_u} \right)^w \right] \quad (6)$$

where δ is normal displacement, and A , w , α , δ_u are PPR parameters that can be determined by satisfying all boundary conditions, including:

$$\begin{aligned} \sigma &= \sigma_c \text{ at } \delta = \delta_c, \quad \sigma = 0 \text{ at } \delta = \delta_u, \\ \lim_{\delta \rightarrow \delta_c} \frac{\partial \sigma}{\partial \delta} &= 0, \quad G = \int_0^{\delta_u} \sigma d\delta, \end{aligned} \quad (7)$$

where G is the total strain energy release rate. By applying the above-mentioned boundary conditions, it can be expressed as:

$$\begin{aligned} w &= \frac{\alpha(\alpha-1)\lambda^2}{1-\alpha\lambda^2}, \quad A = \frac{\sigma_c}{C}, \\ C &= \left[w(1-\lambda)^\alpha \left(\frac{w}{\alpha} + \lambda \right)^{w-1} - \alpha(1-\lambda)^{\alpha-1} \left(\frac{w}{\alpha} + \lambda \right)^w \right], \end{aligned} \quad (8)$$

where

$$\lambda = \frac{\delta_c}{\delta_u} \quad (9)$$

δ_u can be determined using the following equation as:

$$G = \frac{1}{2} K \delta_c^2 + \int_{\delta_c}^{\delta_u} \sigma d\delta \quad (10)$$

In numerical damage simulation, the corresponding the damage variables can be defined using Eq. (4) and the corresponding traction in Eq. (6). After generating the damage variable at all the displacements, the modified PPR model can be directly implemented in ABAQUS using the tabular capability as a function of relative displacement.

1.3 Cohesive Zone Length

As shown in Fig. (2), the length of the cohesive zone l_{cz} is introduced as the distance between the crack tip and the point where the maximum cohesive traction is achieved.

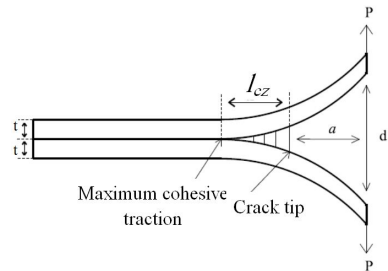


Fig. 2. Cohesive zone length of DCB specimen

The length of the cohesive zone at the initiation of crack growth is independent of applied load and crack length. This means that the cohesive zone length at the crack initiation is a material property. There are several models in the literature that estimated the length of the cohesive zone [4] to [6], [16] and [17]. All of the models for estimation of the cohesive zone length have similar forms as mentioned in Eq. (11).

$$l_{cz} = RE \frac{G_{Ic}}{\sigma_{Ic}^2}, \quad (11)$$

where G_{Ic} is the critical strain energy release rate, σ_{Ic} is the normal cohesive strength, and R is a parameter

that depends on each cohesive zone model. For instance, Irwin's model [17] carried out with $R = 0.31$ or in Dugdale [4] and Barenblatt [5] models, the value for R is considered to be 0.4.

2 FINITE ELEMENT SIMULATION

Three-dimensional finite element models are developed in ABAQUS 6.12 [18] to model the delamination onset and growth, using two different constitutive laws. The DCB model was composed of two layers of eight-noded solid elements, C3D8R (adherent layers), which were connected with a layer of zero thickness eight-node cohesive element, COH3D8, (cohesive layer). Adherent layers were connected to the cohesive layer by surface-to-surface tie constraints. Fig. 3 illustrates the deformed shape of the DCB specimen during crack propagation. A more refined mesh near the crack tip, the outer surface of specimen and in the damage propagation region was used. Boundary conditions included applying a vertical displacement and horizontally restraining the upper and lower edge node of the arms (Fig. 3). In order to predict an accurate propagation of delamination, it is necessary to have an adequate fine finite element discretization in the cohesive zone length to achieve a good estimation of the interlaminar stress fields. When the cohesive zone is discretized by too few numbers of elements, the distribution of tractions ahead of the crack tip is not represented accurately. Thus, in order to achieve successful FEM results, it is necessary to have a minimum number of elements in the cohesive zone length. The number of cohesive elements in the cohesive zone is:

$$N_e = l_{cz} / l_e, \quad (12)$$

where l_e is the length of the cohesive elements in the direction of crack propagation and l_{cz} is the cohesive zone length. There are several guidelines for the

minimum number of elements in the cohesive zone length. However, this number is not well established.

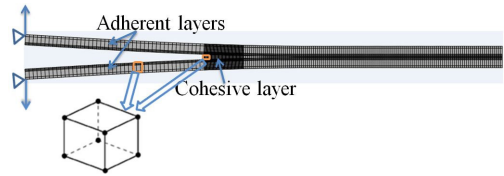


Fig. 3. Deformed shape of simulated DCB with 3D elements

3 EXPERIMENTAL APPROACHES

3.1 Mode I Fracture Toughness Measurement

3.1.1 The DCB Test

Fig. 4a shows the geometry and dimensions of the DCB specimens. In the process of specimen fabrication, the E-glass/epoxy composite plate with a thickness of $2h = 4.2$ mm was first prepared. The E-glass fibres were impregnated with a ML506 epoxy resin and HA11 hardener. The laminates were fabricated with the hand lay-up technique, and the pre-crack length was produced by positioning a 13 μ m thick Teflon insert at the mid-plane of the plate. In order to produce plates with the desired fibre volume fraction, special pressure tool was applied in order to squeeze out excess resin. Then, the plate was left at room temperature for 24 h to dry. After that, the plate was trimmed with a water jet machine along the longitudinal direction in order to obtain narrow specimens with the desired dimension and initial crack length. After trimming, the nominal length (l) and the nominal width (b) of the DCB specimen were 108 and 25 mm, respectively. The initial crack length (a) was 40 mm. Fibre volume fractions, V_f , measured using the resin burn-off method. Table 1 lists the mechanical property of E-glass/epoxy woven fabrication with $V_f = 49\%$ that was used in this research. All of the tests on DCB specimen were

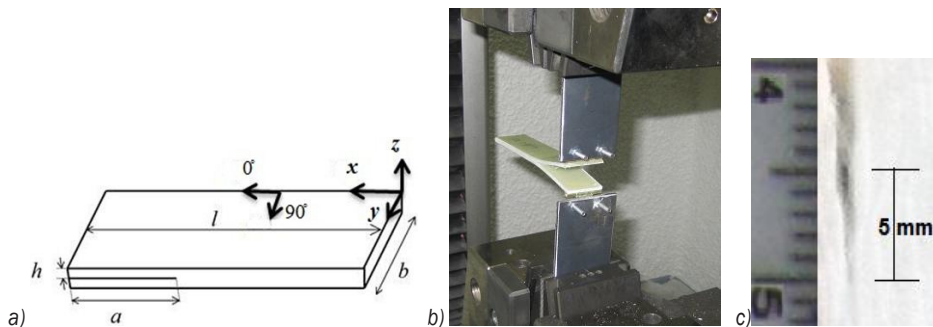


Fig. 4. a) DCB specimen, b) typical DCB test, c) crack length measurement during propagation

completed on a ZWICK electro-mechanical loading frame at room ambient temperature. Fig. 4b shows a typical DCB test. All DCB tests were carried out using displacement control at the crosshead speed of 1 mm/min according to ASTM D5528 standard [19]. Three specimens with $a = 40$ mm crack length were tested. A load-displacement response was recorded for each specimen during the test. In this work, the crack length was monitored by bonding a strip of paper with the graduations printed on it to the specimen's edge and by taking photos during the experiments with 5 s intervals using a 5 megapixel digital camera. The experimental magnitudes of P - δ - a as a function of time were determined. The time of each P - δ data point was computed using the applied displacement and the corresponding loading rate. The time for each value of crack length is the one at which the corresponding photo was taken. The photo in Fig. 4c was taken during a test and shows the crack tip, allowing the crack length measurement. These experimental results were then used to verify the adequacy of the three-dimensional finite element scheme utilized to obtain G_{Ic} .

3.1.2 Data reduction Method for G_{Ic}

In order to calculate the mode-I critical strain energy release rate, there are many commonly used data reduction methods, including compliance calibration method (CCM) that is based on the Irwin-Kies principle, direct beam theory (DBT) and the Corrected Beam Theory. In the present work, the corrected beam theory proposed by de Moura et al. [20] was used. Only one specimen is sufficient to obtain the resistance curve (R -curve) of the specimen, which is the main advantage of the presented method. According to this theory, mode-I critical strain energy release rate can be computed as:

$$G_{Ic} = \frac{3P\delta}{2b(a+|\Delta|)}, \quad (13)$$

where P , a and b are load, crack length and specimen width, respectively. The parameter Δ is the crack length correction to account the crack tip rotation and deflection. According to the beam theory, the relationship between the compliance and the crack length is expressed by:

$$C^{1/3} = \frac{2(a+|\Delta|)}{h(E_1 b)^{1/3}}. \quad (14)$$

The crack length correction can be obtained using the linear regression of $C^{1/3}$ versus crack length data.

3.2 Normal Cohesive Strength Measurement

The objective of the NCS test is to determine the Mode I cohesive strength (σ_{Ic}) as an essential parameter for description of the traction separation law of cohesive elements. The fabrication of an NCS specimen is similar to that of a double cantilever beam except for the delaminated area. In the process of NCS specimen fabrication, first a 14-layer woven rectangular plate $[0/90]_{14}$ was produced. After the 7th layer of fabrication, a 13 μm thick Teflon layer was inserted at all sides of the plate so that a $10\text{ mm} \times 10\text{ mm}$ square area at the middle of plate was released. This area is the cohesive area of NCS specimen, as shown in Fig. 5a. After that, the plate was trimmed to a 80×50 rectangular dimension so that the cohesive area was located at the middle of rectangular specimen. The specimen was bonded to fixture surfaces. Prior to bonding, the surfaces of both fixture and specimen, were lightly roughened with the sandpaper on the bonding face and cleaned with acetone. The area of bond is large enough compared to the cohesive area so that debonding would not occur between the specimen and fixture surfaces the testing procedure. Fig. 5a shows the NCS specimen after testing, and Fig. 5b shows a typical NCS test.

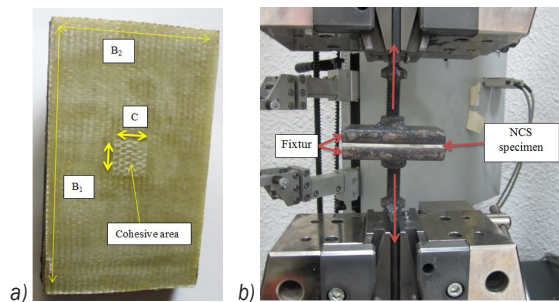


Fig. 5. a) NCS specimen after test, b) NCS test

As shown in Fig. 5a, the dimensions of rectangular plates B_1 and B_2 are 80 mm and 50 mm, respectively, and the width of cohesive the square area (C) is 10 mm. All of the NCS tests were carried out using displacement control at the crosshead speed of 0.5 mm/min until fracture. In this process, three NCS failure tests were completed. In order to prevent slippage during the test, the specimen was accurately balanced and a very little clamping force was required. Decohesion between the fibre and matrix in the NCS cohesive area is the dominant failure mode. Thus, it is obvious that the bulk matrix behaves differently than the thin cohesive layer due to constraint effects induced by the adhesion between the fibre and matrix.

As a result, the bulk matrix properties could not be used to determine normal cohesive strength, and this parameter should be determined using an NCS test method. For the purposes of data reduction, all specimens were assumed to have failed instantly. The specimen failure is assumed at its maximum load value. The normal cohesive strength values (σ_{Ic}) were computed using Eq. (15) as:

$$\sigma_{Ic} = \frac{P_{max}}{A_{NCS}}, \quad (15)$$

where P_{max} is the maximum load in which failure occurs and A_{NCS} is the cohesive area of the NCS specimen.

4 RESULTS AND DISCUSSION

4.1 Experimental Results

Fig. 6 shows the load-displacement response of three NCS experiments. The measured load is initially negligible, corresponding to the clearance of the fixture. The test was preceded until a maximum load was achieved and followed by a sudden load drop, indicating specimen failure.

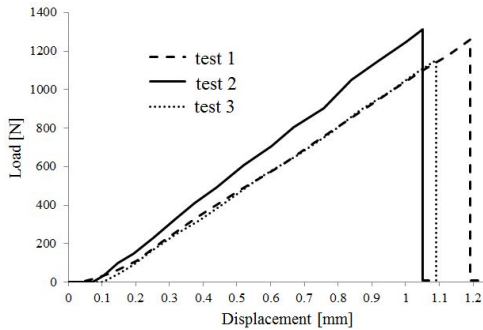


Fig. 6. Load-displacement response of NCS test

The mean value of maximum loads of Fig. 6 was considered as P_{max} . Using Eq. (15) for data reduction and substituting this value for P_{max} , the cohesive strength of composite material computed and is equal to 12.42 MPa. To calculate the experimental resistance curve, the numerical values of $P-\delta-a$ parameters were recorded during crack propagation and were used to obtain the critical fracture energies versus crack length. Fig. 7 shows the experimentally obtained R -curve of the material. To simulate the crack propagation using cohesive elements, the mean value of G_{Ic} was considered as the fracture toughness of the material. Table 2 lists the cohesive properties of E-glass/epoxy woven composite laminate.

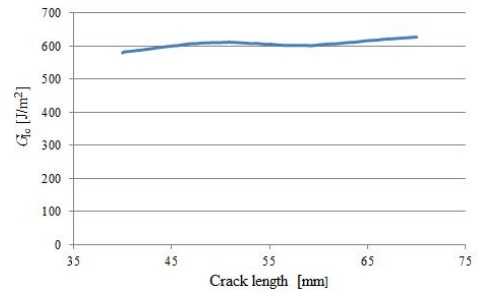


Fig. 7. R -curve of E-glass/epoxy specimen

Table 1. Mechanical properties of E-glass/epoxy

E_1 [GPa]	E_2 [GPa]	E_3 [GPa]	ν_{12}	G_{12} [GPa]	G_{13} [GPa]	G_{23} [GPa]
18.43	18.43	3.57	0.15	2.85	2.85	2.85

Table 2. Interfacial property of E-glass/epoxy

σ_{Ic} [MPa]	τ_{IIc} [MPa]	τ_{IIIc} [MPa]	G_{Ic} [J/m ²]	G_{IIc} [J/m ²]	G_{IIIc} [J/m ²]	η
12.42	22.64	22.64	604	720	720	1.8

4.2 Cohesive Zone Model Results

FEM models of each specimen were carried out using the Ply elastic properties of adherent layers that are given in Table 1 and the interfacial properties obtained previously and listed in Table 2. It should be mentioned that when using Eq. (2) for interfacial penalty stiffness, the value of $K = 85 \times 10^6$ N/mm³ is used for all DCB simulations.

4.2.1 Determination of Cohesive Zone Length

Cohesive zone length was previously introduced as the distance between the maximum traction and the crack front. Therefore, in order to calculate the distribution of traction in the cohesive layer of model and the corresponding cohesive zone length, a very refined mesh using element size of 0.125 mm was used in the area near the crack tip of the DCB specimen. The distribution of tractions ahead of the crack tip at the delamination onset of the DCB specimen is illustrated in Fig. 8. At the crack initiation point, traction at the crack tip vanished as expected from the cohesive zone theory. According to this analysis, the cohesive zone length of material is 3.76 mm, as shown in Fig. 8.

Using the material property that shown in Table 1 and 2 and Eq. (11), the parameter R is computed as 0.27. This value is closest to the Irwin [17] (0.31) model. The cohesive zone length is a material property that has a high order of importance regarding obtaining a successful prediction of delamination onset. This

parameter was previously introduced as a function of normal cohesive strength by Turon et al. [11]. Thus, using an absolute value for normal cohesive strength, this parameter as a material property is determined.

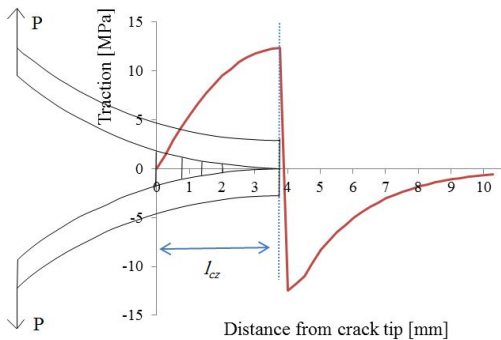


Fig. 8. Distribution of traction ahead of crack tip

4.2.2 Investigation of Mesh Refinement

In order to investigate the effect of mesh refinement in the cohesive zone length on numerical prediction of delamination onset, several DCB specimens were simulated with different sizes of cohesive elements in the cohesive zone length. The predicted load-displacement responses obtained using DCB models are compared to the experimental solution in Fig. 9. In this analysis, cohesive element sizes (in the direction of crack propagation) range from 0.125 mm to 2 mm. The results illustrate that for all mesh sizes a converged solution was obtained but it is necessary to apply a mesh size, l_e , less than 1 mm to accurately predict delamination initiation. The analysis using coarser meshes significantly overpredicts the strength of the DCB specimen, and the response does not follow the experimental results. Cohesive zone length, l_{cz} , for the material described in Tables 1 and 2 was determined as 3.76 mm. Therefore, for a mesh size smaller than 1 mm, more than three elements would span the cohesive zone length, which is enough for an accurate prediction of the fracture onset.

There are several guidelines for the minimum required element in cohesive zone length. For example, Moës and Belytschko [21] proposed using more than 10 elements, while Falk et al. [16] suggested between 2 and 5 elements. In the work of Dávila et al. [22], the minimum required element length to predict the delamination in a DCB model was 1 mm, and using more than 3 elements in cohesive zone length of simulated DCB specimen was recommended. The difference in predictions from using a coarse mesh in the modelling of delamination in a DCB specimen is

due to the magnitude of tractions ahead of the crack tip.

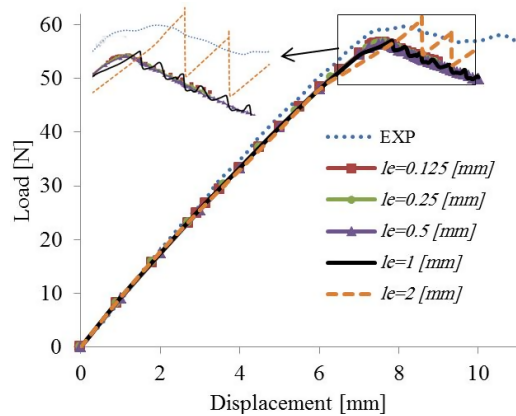


Fig. 9. Damage simulation using different mesh refinement

4.2.3 Comparison of Damage Models

A study also was conducted to investigate the adequacy of the two mentioned traction separation laws used to simulate damage propagation. The objective was to determine how the used models reproduce crack initiation and propagation. Fig. 10 shows the load-displacement of the cohesive zone model and experimental work on a DCB specimen.

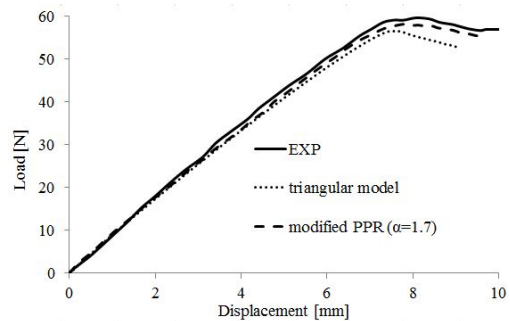


Fig. 10. Load displacement response of experimental and damage models

In the current study, the value of shape parameter α in the PPR model varied from 1 to 4; the result was that increasing the value of the shape parameter α increased the rate at which material loses its stiffness once damage was initiated. In other words, increasing parameter α decreases the fracture process zone effect ahead of the crack tip. In the case of $\alpha < 2$, there is a gradual fall in the load, but in the case of $\alpha > 2$ a sudden drop in the load-displacement response is achieved, which means a large number of cohesive elements failed at the same time. For clarity, the results are not shown in this figure. In this study, a

value of $\alpha = 1.7$ was found to be the optimum value for the numerical prediction of damage propagation. As shown in Fig. 10, the modified PPR model was found to be adequate to reproduce the experimentally observed behaviour of the composite specimen, and reproduced approximate smooth crack initiation and propagation while the bilinear model depicted sudden damage propagation. The maximum difference between the experimental and bilinear models is 8.8 % while for PPR it is 2.6 %. This means the modified PPR model accounted fracture process zone which created ahead of crack tip.

5 CONCLUSION

A methodology for the delamination characterization of composite laminates under pure Mode I was proposed.

- An NCS test has been proposed to compute the Mode-I cohesive strength as a cohesive parameter.
- The Mode-I critical strain energy release rate versus the crack length of E-glass/epoxy composite laminate was computed using corrected beam theory for data reduction.
- A mixed-mode triangular constitutive relationship between stress (σ) and relative displacements (δ) of cohesive elements and modified PPR damage model were considered to simulate delamination onset and propagation.
- The results of the three-dimensional finite element analysis with cohesive parameters (σ_{1c} , G_{1c}) enclosed the adequacy of cohesive parameters.
- Accurate damage prediction was achieved using the modified PPR model, and it was considered by the authors to be an accurate model for damage characterization of material.
- Modified PPR models accurately described the fracture process zone, which was created ahead of the crack tip as compared to bilinear model.
- To ensure the sufficient dissipation of energy, cohesive zone length as a material property was determined.
- Numerical analysis with different discretizations of the cohesive zone length showed that numerical predicted responses correlate well with the experimental solutions when at least 3 elements span the cohesive zone length.

6 ACKNOWLEDGMENT

This work has been funded by University of Tabriz, and its authors would like to thank the University of Tabriz for the grant.

7 REFERENCES

- [1] Karpiliski, A. (2006). An Introduction to the diagnosis of the delamination process for glass/epoxy composites during high-pressure abrasive water-jet cutting. *Strojniški vestnik - Journal of Mechanical Engineering*, vol. 52, no. 7, p. 532-538.
- [2] Hasiotis, T., Badogiannis, E., Tsouvalis, N.G. (2011). Application of ultrasonic C-scan techniques for tracing defects in laminated composite materials. *Strojniški vestnik - Journal of Mechanical Engineering*, vol. 57, no. 3, p. 192-203, DOI:10.5545/sv-jme.2010.170.
- [3] Brunner, A., Blackman, B., Davies, P. (2008). A status report on delamination resistance testing of polymer-matrix composites. *Engineering Fracture Mechanics*, vol. 75, no. 9, 2779-2794, DOI:10.1016/j.engfractmech.2007.03.012.
- [4] Dugdale, D. (1960). Yielding of steel sheets containing slits. *Journal of the Mechanics and Physics of Solids*, vol. 8, no. 2, p. 100-104, DOI:10.1016/0022-5096(60)90013-2.
- [5] Barenblatt, G. (1962). The mathematical theory of equilibrium cracks in brittle fracture. *Advances in Applied Mechanics*, vol. 7, no. 1, p. 55-129, DOI: 10.1016/j.ech.2007.03.012.
- [6] Hillerborg, A., Mod er, M., Petersson, P.-E. (1976). Analysis of crack formation and crack growth in concrete by means of fracture mechanics and finite elements. *Cement and Concrete Research*, vol. 6, no. 6, p. 773-781, DOI:10.1016/0008-8846(76)90007-7.
- [7] Song, S.H., Paulino, G.H., Buttlar, W.G. (2006). Simulation of crack propagation in asphalt concrete using an intrinsic cohesive zone model. *Journal of Engineering Mechanics*, vol. 132, no. 11, p. 1215-1223, DOI:10.1061/(ASCE)0733-9399(2006)132:11(1215).
- [8] Zhang, Z.J., Paulino, G.H. (2005). Cohesive zone modelling of dynamic failure in homogeneous and functionally graded materials. *International Journal of Plasticity*, vol. 21, no. 6, p. 1195-1254, DOI:10.1016/j.ijplas.2004.06.009.
- [9] Khoshravan, M.R., Moslemi, M. (2014). Investigation on mode III interlaminar fracture of glass/epoxy laminates using a modified split cantilever beam test. *Engineering Fracture Mechanics*, vol. 127, p. 267-279, DOI:10.1016/j.engfractmech.2014.06.013.
- [10] Song, S.H., Paulino, G.H., Buttlar, W.G. (2006). A bilinear cohesive zone model tailored for fracture of asphalt concrete considering viscoelastic bulk material. *Engineering Fracture Mechanics*, vol. 73, no. 18, p. 2829-2848, DOI:10.1016/j.engfractmech.2006.04.030.
- [11] Turon, A., Davila, C.G., Camanho, P.P., Costa, J. (2007). An engineering solution for mesh size effects in the simulation of delamination using cohesive zone models. *Engineering Fracture Mechanics*, vol. 74, no. 10, p. 1665-1682, DOI:10.1016/j.engfractmech.2006.08.025.
- [12] Yuan, H., Li, X. (2014). Effects of the cohesive law on ductile crack propagation simulation by using cohesive zone models. *Engineering Fracture Mechanics*, vol. 126, p. 1-11, DOI:10.1016/j.engfractmech.2014.04.019.
- [13] Bhattacharjee, T., Barlingay, M., Tasneem, H., Roan, E., Vemaganti, K. (2013). Cohesive zone modelling of mode I tearing in thin soft materials. *Journal of the Mechanical*

- Behavior of Biomedical Materials*, vol. 28, p. 37-46, DOI:10.1016/j.jmbbm.2013.07.015.
- [14] Benzeggagh, M., Kenane, M. (1996). Measurement of mixed-mode delamination fracture toughness of unidirectional glass/epoxy composites with mixed-mode bending apparatus. *Composites Science and Technology*, vol. 56, no. 4, p. 439-449, DOI:10.1016/0266-3538(96)00005-X.
- [15] Park, K., Paulino, G.H., Roesler, J.R. (2009). A unified potential-based cohesive model of mixed-mode fracture. *Journal of the Mechanics and Physics of Solids*, vol. 57, no. 6, p. 891-908, DOI:10.1016/j.jmps.2008.10.003.
- [16] Falk, M.L., Needleman, A., Rice, J.R. (2001). A critical evaluation of cohesive zone models of dynamic fracture. *Le Journal de Physique IV*, 11(PR5), Pr5-43-Pr45-50.
- [17] Irwin, G. (1997). Plastic zone near a crack and fracture toughness.
- [18] *Abaqus/CAE user manual*. Abaqus 6.12 Documentation.
- [19] ASTM D5528:2007. *Standard Test Method for Mode I Interlaminar Fracture Toughness of Unidirectional Fiber-Reinforced Polymer Matrix Composites*, ASTM International West Conshohocken.
- [20] De Moura, M., Campilho, R., Gonçalves, J. (2008). Crack equivalent concept applied to the fracture characterization of bonded joints under pure mode I loading. *Composites Science and Technology*, vol. 68, no. 10-11, p. 2224-2230, DOI:10.1016/j.compscitech.2008.04.003.
- [21] Moës, N., Belytschko, T. (2002). Extended finite element method for cohesive crack growth. *Engineering Fracture Mechanics*, vol. 69, no. 7, p. 813-833, DOI:10.1016/S0013-7944(01)00128-X.
- [22] Dávila, C.G., Camanho, P.P., de Moura, M. F. (2001). Mixed-mode decohesion elements for analyses of progressive delamination. *Proceedings of the 42nd AIAA/ASME/ASC*, DOI:10.2514/6.2001-1486.

Modelling of an Electrohydraulic Proportional Valve with a Synchronous Motor

Andrzej Milecki* – Dominik Rybarczyk

Poznan University of Technology, Institute of Mechanical Technology, Poland

This paper presents the design of proportional valve with a Permanent Magnet Synchronous Motor (PMSM). The proposed valve is described, and its history is briefly reviewed. Basic equations describing the valve are formulated and its simulation model is implemented in MATLAB-Simulink software. Selected nonlinearities are included in this model. In order to determine the basic parameters of the discussed proportional valve, a test stand is built, which enables valve investigations. In this test stand, a valve control system based on programmable logic controller (PLC) with a touch panel and inverter module is implemented and used for investigations. The valve flow characteristics and step responses obtained in simulations are presented. These characteristics are compared with results obtained in experimental investigations. As a result, the valve simulation model is modified and improved.

Keywords: proportional valve, electrohydraulic, synchronous motor

Highlights

- Proposing a new type of hydraulic proportional valve in which the synchronous motor is used.
- Proposing a theoretical description and simulation model of the valve with a synchronous motor.
- Presenting the proposed laboratory investigation results of the valve.
- Improving the simulation model of the valve based on the outcomes of the investigations.

0 INTRODUCTION

Electrohydraulic servo-drives can be controlled by two types of electro-valves: servo- and proportional valves. The servo-valves are used in high-accuracy applications. Proportional valves respond acceptably to the requirements stated in most industrial cases and are much cheaper than servo-valves. Therefore, these elements are commonly used in many industrial electrohydraulic drives. Proportional valves are activated by solenoids and can provide a smooth and continuous variation in flow or pressure in response to an electrical input valve. The basics of the design of proportional valves were established approximately 30 years ago and no significant progress in this area has been visible since then [1] and [2]. Many investigations and related publications about electrohydraulic servo drives have been focused on the improvement of the properties of these drives, via the implementation of modern forms and types of control [3]. Only a few works deal with improvements of the parameters of electrohydraulic drive elements, as well as with finding new ways to provide very accurate movement of valve parts, such as a valve's spool. Thus far, in proportional valves, proportional electromagnets are commonly used as the slider driving part [4]. Only in a few solutions can stepping or DC motors be found, even though they have been known for many years. Based on that, we decided to apply a new type of drive device, a permanent magnet synchronous

motor (PMSM) as electromechanical actuator in the proportional valve (this motor is characterized by very good properties and can assure very good positioning accuracy).

Over the previous decade, only a few papers focused on the applications of different types of motors in hydraulic proportional valves have been published. Murrenhoff [5] described the cross-cutting trends in the design and the development of electrohydraulic valves. He presented an interesting solution, using the direct drive in a proportional valve. In another solution, the use of a stepping motor to transfer the ball screw, which was moving the mechanism with four independent flow sliders, was proposed. The design and investigations of valve in which a piezo actuator was used were described in [6]. Such a valve is characterized by very good dynamic parameters in comparison with valves controlled by proportional electromagnets.

Boes et al. [7] pointed out the advantages of valves with integrated control electronics. The use of powerful processors and a decentralized control system allowed the easy integration of electrohydraulic valve with other elements.

Myszkowski and Milecki [8] described the use of a stepping motor in the valve to obtain a very low velocity of the electrohydraulic drive. It is worth emphasizing that the drive was able to move with a very low constant speed equal to 1 mm/s. However, the drive maximum speed was only 0.125 mm/s,

which was rather low and reduced the number of possible applications.

In another study [9], an unconventional electro-hydraulic proportional flow control valve based on a switching solenoid and a fuzzy-logic controller was proposed. The switching solenoid's non-linear force/stroke characteristic was linearized by a fuzzy-logic controller. The obtained laboratory investigations of this valve were quite satisfactory, assuring low cost.

Šimic et al. [10] presented a new approach to the modelling and simulation of hydraulic spool valves by using simple mathematical expressions to describe the geometry of the sliding spool metering edge. Consequently, different shapes of spool-metering edges in combination with other functional elements could be used in design of hydraulic valves.

The literature overview has shown that only in one paper [11] was the use of an electric servo motor for control of the proportional valve described. However, this solution was significantly different from commonly used designs. The servo-motor that was used in a valve was able to produce torque of as much as 15 Nm. The cam mechanism used allowed the motor shaft to move in the range of only a few degrees of arc. The maximum valve flow was as much as 400 dm³/min; therefore that valve was much bigger than the one considered in this paper.

1 VALVE CONSTRUCTION

The schematic of the valve proposed in this paper is presented in Fig. 1. The valve spool (3) is actuated by a permanent magnet synchronous motor (1). In the proposed valve the motor type 8LVA22 (B&R company) is used. Its basic parameters are power 105 W, current 2.9 A, nominal torque: 0.65 Nm. This motor is connected to the spool (3) by a flexible bellows coupling (2). The second ending of the spool is directly connected to a ball screw (5), whose nut (6) is fixed to the valve body. The rotation of the motor causes the rotation of the ball screw and the axial movement of the spool and its control edges. This movement is proportional to the angular motor displacement and the pitch of the thread used. The direction of rotation determines the direction of spool translation and the opening or closing of valve gaps. It results in the flow of oil to and from the actuator chambers and the displacement of the piston. The spool diameter is 10 mm. There are three rectangular gaps in the body with dimensions of 2.5 mm × 2 mm. The valve size is 10 (below 64 dm³/min).

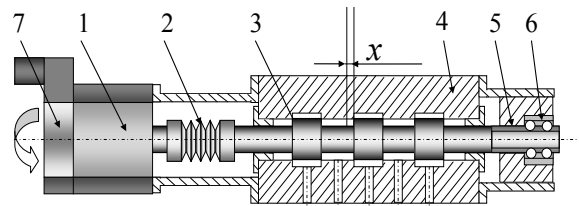


Fig. 1. Scheme of proportional valve with synchronous motor

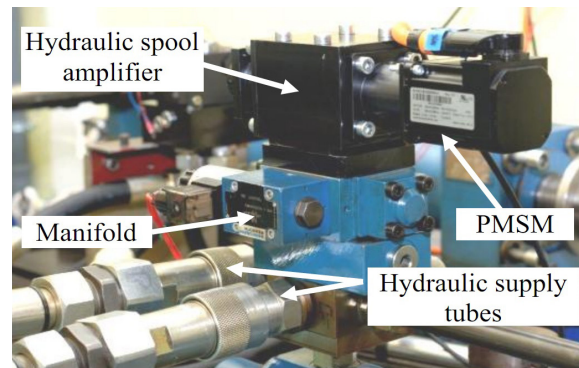


Fig. 2. View of proportional valve with PMSM

The rotor position is measured by an absolute encoder type EnDat 2.2 (7), providing a current position, even after a power failure, with a very high positioning accuracy, equal to 262144 pulses on revolution. As a result, the drive is able to assure the linear resolution of 0.5 mm [12] and [13]. The photo of the valve is presented in Fig. 2. The valve is connected to the cylinder by a specially designed manifold.

2 VALVE MODELING AND BASIC INVESTIGATIONS

In order to investigate the designed and built valve, a test stand was arranged. Its schematic diagram is presented in Fig. 3. A valve control system is based on PLC working under a real time operating system Automation Runtime with a Power Panel 500 touch panel and ACOPOS servo-controller used for PMSM control [14]. A HySense QG100 flow meter is used, whose parameters are max. flow $Q = 30$ dm³/min, max. pressure $p = 30$ MPa, non-linearity ± 0.5 %, 1640 pulses per dm³. It is connected to the counter module in the PLC unit. As a communication interface between the PLC and the servo controller, a Powerlink interface is used. The view of the control system is shown in Fig. 4. In the synchronous motor controller, two feedback loops are used. The inner one is a velocity feedback in which a P type regulator is used. The second one is the positioning loop with a PI regulator. Their parameters are set using autotuning mode, based on the detection of one or two points of the process frequency response using relay excitation

described by Åström and Hägglund [15]. The following values of parameters are used: $k_v = 0.4$ l/s for the velocity loop and $k_p = 220$, integrative time $T_i = 0.0004$ s for positioning loop.

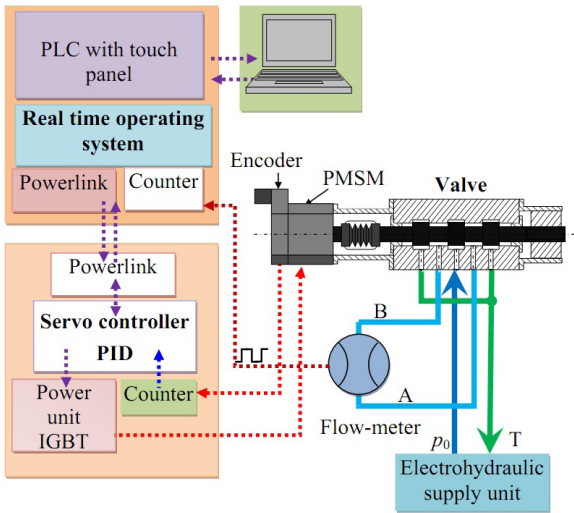


Fig. 3. The scheme of control stand

The valve flow through the sharp-edged nozzles is turbulent [2] and [9], which can be described using the following general equation:

$$Q = K_Q \sqrt{\Delta p} \cdot x, \quad (1)$$

where K_Q is a flow coefficient, Δp pressure drop on a valve, and x a spool displacement (± 2.5 mm).

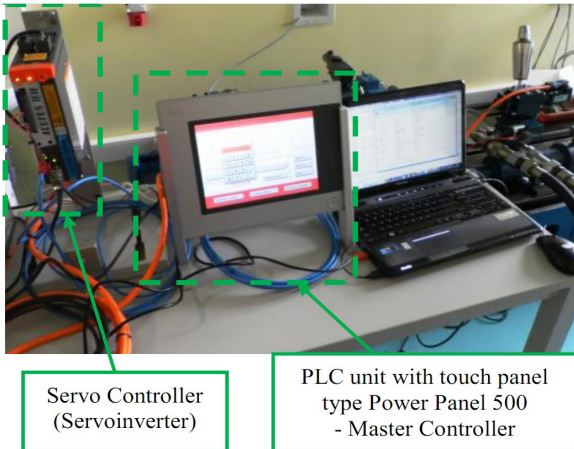


Fig. 4. A view of proportional valve with a synchronous motor

The flow coefficient K_Q depends on the following parameters:

$$K_Q = \mu_d \cdot \sqrt{2 / \rho} \cdot w, \quad (2)$$

where μ_d is the discharge coefficient, ρ oil density: $780 \text{ dm}^3/\text{min}$, w width of the gap (6 mm).

The value of the discharge coefficient μ_d depends mainly on the geometry of the slot. In the case of the proportional valve considered in this paper, this value is usually taken as 0.64 [2]. Using Eq. (1), the theoretical calculations of valve flow Q for spool displacements in a range of ± 2.5 mm and for pressures 4 MPa, 6 MPa, 12 MPa and 14 MPa are made and shown in Fig. 5. In order to verify these calculations, the real valve is investigated. A flow Q changes for two supply pressures, 6 MPa and 12 MPa, are measured. Due to the applied flow meter, it was possible to measure flow only until $30 \text{ dm}^3/\text{min}$. It can be noted that the characteristics of a real valve are curved when the input signal increases. Most probably, this is caused by the valve spool's non-symmetry. In the test stand (Fig. 3), both gaps are connected serially. If one of these gaps is smaller than the other, the pressure drop on the first one is bigger. As a result, the flow saturation occurs in this gap, which is determined by pressure square root characteristic, described by Eq. (1). This is visible in the presented laboratory results.

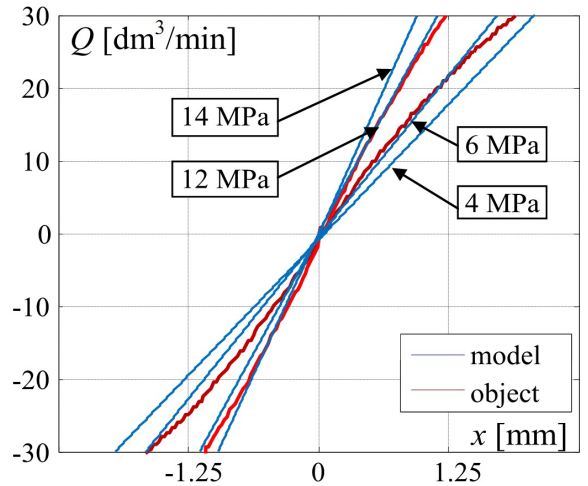


Fig. 5. The flow characteristics

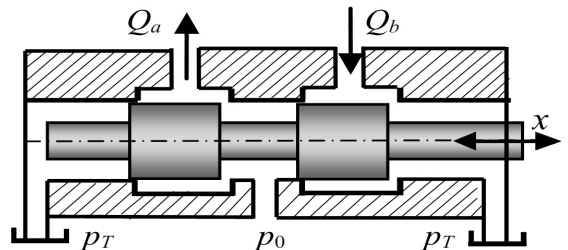


Fig. 6. A four-edge hydraulic amplifier

The hydraulic part of proportional valve is a four-edge amplifier, shown in Fig. 6. Its static behaviours

can be characterized using so-called square root equations, which describe the oil flow through the hydraulic nozzles. These flows can be described by following equations:

$$\text{for } x > 0: \begin{cases} Q_a(t) = K_Q \sqrt{p_0 - p_a(t)} \cdot x(t) \\ Q_b(t) = K_Q \sqrt{p_b(t)} \cdot x(t) \end{cases}, \quad (3)$$

$$\text{for } x < 0: \begin{cases} Q_a(t) = K_Q \sqrt{p_a(t)} \cdot x(t) \\ Q_b(t) = K_Q \sqrt{p_0 - p_b(t)} \cdot x(t) \end{cases}, \quad (4)$$

where x is a spool displacement [mm], Q_a flow through the gap A [dm³/min], Q_b flow through the gap B [dm³/min], K_Q flow coefficient, p_0 supply pressure [Pa], and p_a, p_b pressures in chambers A and B [Pa].

The spool dynamics can be described by the following PMSM motion equation:

$$m \frac{d^2 x(t)}{dt^2} + D \frac{dx(t)}{dt} = \frac{2\pi}{P} K_T i(t) = K_i i(t), \quad (5)$$

where m is the mass reduced in motor axis (0.2 kg), D viscous friction coefficient (120 Ns/m), P ball screw pitch (2.5 mm/rev.), T PMS motor torque, K_T torque coefficient (0.23 Nm/A).

In the first approach, the electric circuit of PMS motor is described by the second order transfer function:

$$L \frac{di(t)}{dt} + Ri(t) = U(t), \quad (6)$$

where L is 4.1 mH, $R = 2$ Ohm coil inductance and resistance, i current, U supply voltage.

After the Laplace transformation of Eqs. (5) and (6), and their combination we obtain:

$$X(s) = \frac{K_T / D}{T_1 s^2 + s} \cdot \frac{1/R}{T_2 s + 1} U(s). \quad (7)$$

The drive transfer function is as follows:

$$G(s) = \frac{X(s)}{U(s)} = \frac{k_d}{s(T_1 s + 1)(T_2 s + 1)}, \quad (8)$$

where $T_1 = m/D$ and $T_2 = L/R$ are time constants.

Using Eqs. (3), (4) and (7), a simulation model of the proportional valve with PMSM is prepared in Matlab-Simulink software (Fig. 7). It includes square root flow non-linearity, which is modelled using the function *Sqrt*. A simplified model of the PMSM is also included. The rotor position and the valve spool position are simultaneously measured by element characterized by coefficient k_m and fed back to the PI type, position controller. The measured position is derived in order to obtain a velocity signal, used in inner feedback loop.

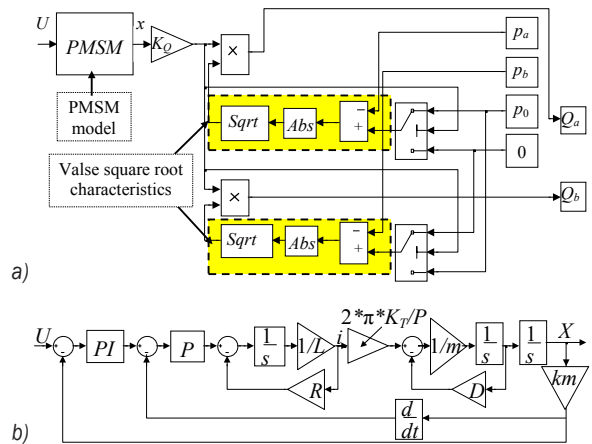


Fig. 7. Matlab-Simulink simulation models of the: a) valve, b) PMSM (simplified)

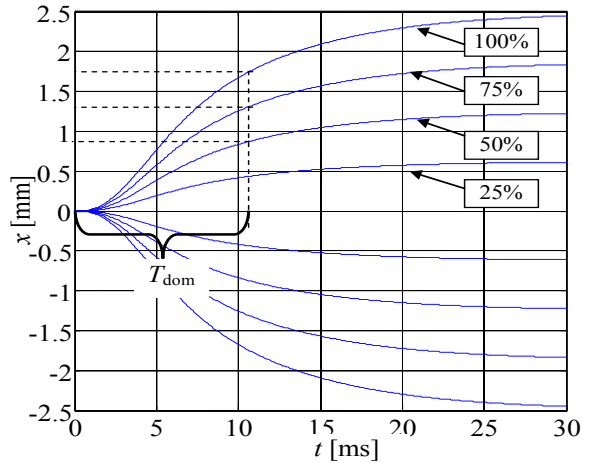


Fig. 8. The step responses of the valve spool

The valve step responses obtained by simulation (spool displacement x) are shown in Fig. 8. The time constant T_{dom} , which represents the time it takes the system's step to reach 0.63 of its final value, is equal to about 11 ms.

3 MODEL IMPROVEMENT

In order to verify the correctness of the proposed simulation model, the real valve step responses are measured. The results are shown in Fig. 9. The recorded curves indicate that the valve is characterized by a significant time delay, which is caused by a PLC controller and communication interface, which is used to control the PMSM.

Curves collected during several experimental investigations showed that the delay time constant T_0 is equal to 10 ms. This delay is included into the following transfer function:

$$G(s) = \frac{X(s)}{U(s)} = \frac{k_d \cdot e^{s \cdot T_0}}{(T_1 \cdot s + 1) \cdot (T_2 \cdot s + 1)} \quad (9)$$

In this transfer function, the transport delay T_0 and time constants T_1 and T_2 are used. The value of dominant time constant T_{dom} depends on the assumed step signal values and varies from 7 to 12 ms (Fig. 9). These changes are most probably caused by a maximum current limitation of the motor. This current saturation is included in the model, shown in Fig. 10.

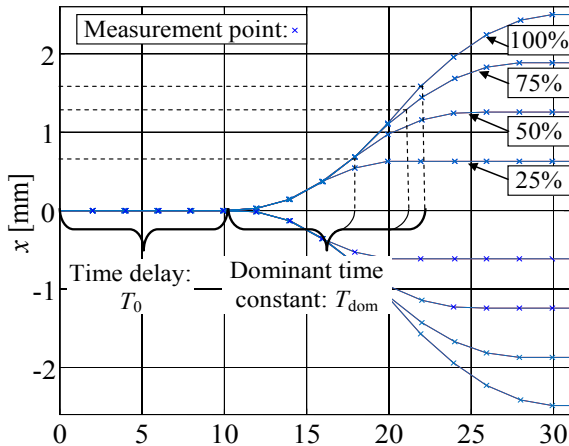


Fig. 9. Step responses of the valve spool

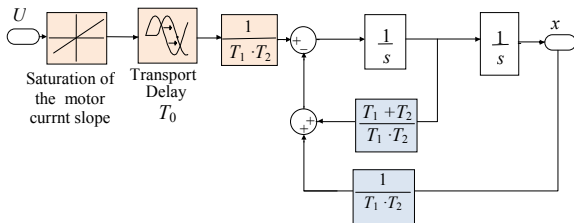


Fig. 10. Non-linear model of the PMS motor

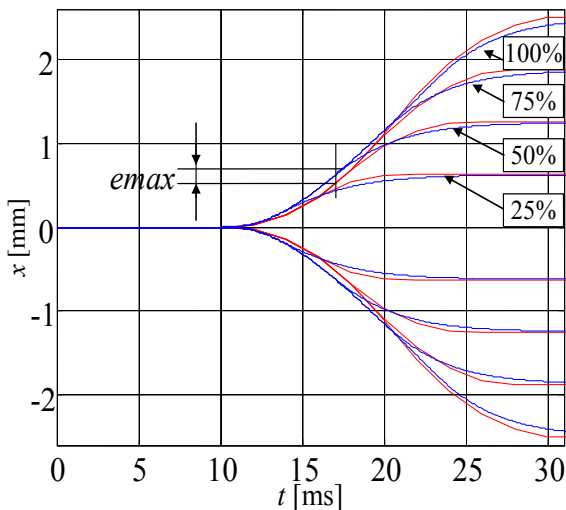


Fig. 11. The model and real valve step response

In Fig. 11, the step responses obtained in simulation with the use of model shown in Fig. 10 are presented. For comparison, curves obtained in experimental investigations are also shown in this figure. The maximum difference between the model and the real object curves e_{max} is about 9 %. Consequently, one may conclude that the simulation results fit quite well with the results obtained in laboratory tests. The improved simulation model can then be regarded as suitable for the modelling and simulation of the proportional valve with PMSM drive.

4 CONCLUSIONS

In this paper, the theoretical description of a proportional valve with a PM synchronous motor is presented. Based on this description, a computer simulation model of a proposed valve with PMSM is proposed and implemented in MATLAB-Simulink software. This model is then compared with a real valve and improved. The study includes the laboratory examination of basic characteristics, such as valve flow and step response. The chosen simulation results are shown and discussed. The laboratory investigations of the proposed valve with PMSM are presented and compared with the simulation results. The simulation model proposed in the paper fits reflected the real situation very well.

The proportional valve with a permanent magnet synchronous motor that is presented in this paper represents an interesting alternative to servo-valves. It may assure better properties (especially dynamic and accuracy ones) than electrohydraulic standard proportional valves with solenoids do.

5 ACKNOWLEDGMENT

This paper was supported by the Polish Ministry of Science and Education, grant no. 02/23/DSPB/1208, Poland.

6 REFERENCES

- [1] Chapple, P. (2003). *Principles of Hydraulic System Design*. Coxmoor Publishing Company, Oxford.
- [2] Cundiff, S.J. (2000). *Fluid Power Circuits and Control Fundamental and Applications*. CRC Press, Boca Raton, London, New York, Washington.
- [3] Ming, X., Jin, B., Chen, G., Ni, J. (2013). Speed-Control of Energy Regulation Based Variable-Speed Electrohydraulic Drive. *Strojniški vestnik - Journal of Mechanical Engineering*, vol. 59, no. 7-8, p. 433-442, DOI:10.5545/sv-jme.2012.911.

- [4] Muraru, V., Muraru, C. (2000). Optimization of the proportional solenoids for electrohydraulic control systems. *Proceedings of the 1st FPNI-PhD Symposium*, p. 157-166.
- [5] Murrenhoff, H. (2003). Trends in valve development. *Ölhydraulik und Pneumatik*, vol. 46, no. 4, p. 1-36.
- [6] Herakovič, N. (1995). Piezoactuator for a single-stage servovalve with high dynamic response (Piezoaktorbetätigung für ein einstufiges hochdynamisches Servoventil), *Ölhydraulik & Pneumatik*, vol. 39, no. 8, p. 601-605. (in German)
- [7] Boes, Ch., Lenz, W., Mueller, J. (2003). Digital servo valves with fieldbus interface in closed loop applications. *The 8th Scandinavian International Conference on Fluid Power*, Tampere.
- [8] Myszkowski, A., Milecki, A. (2009). Modelling of electrohydraulic servo drive used in very low velocity applications. *International Journal of Modelling, Identification and Control*, vol. 7, no. 3, p. 246-254, DOI:10.1504/IJMIC.2009.027211.
- [9] Renn, J.C., Tsai, C. (2005). Development of an unconventional electro-hydraulic proportional valve with fuzzy-logic controller for hydraulic presses. *The International Journal of Advanced Manufacturing Technology*, vol. 26, no. 1-2, p. 10-16, DOI:10.1007/s00170-003-1973-7.
- [10] Šimic, M., Debevec, M., Herakovič, N. (2014). Modelling of hydraulic spool-valves with specially designed metering edges. *Strojniški vestnik - Journal of Mechanical Engineering*, vol. 60, no. 2, p. 77-83, DOI:10.5545/sv-jme.2013.1104.
- [11] Wiegandt, W. (2010). Development of a servomotor driven proportional valve. *7th International Fluid Conference*, Aachen.
- [12] Rybarczyk, D., Milecki, A. (2015). Modeling and control of proportional valve with synchronous motor. *Solid State Phenomena*, vol. 220-221, p. 457-462, DOI:10.4028/www.scientific.net/SSP.220-221.457.
- [13] Sędziak D., Regulski R. (2015). Design and investigations into piezobender controlled servovalve. *Solid State Phenomena*, vol. 220-221, p. 520-526, DOI:10.4028/www.scientific.net/SSP.220-221.520.
- [14] B&R, Motion control, from <http://www.br-automation.com/en-gb/products/motion-control/>, accessed on 2015-02-20.
- [15] Åström K., Hägglund T. (1995). *PID controllers: Theory, Design and Tuning*. Instrument Society of America, Research Triangle Park.

Computerised Design and Simulation of Meshing and Contact of Formate Hypoid Gears Generated with a Duplex Helical Method

Yu Zhang¹ – Hongzhi Yan^{1,*} – Tao Zeng^{1,2}

¹ Central South University, State Key Laboratory of High-Performance Complex Manufacturing, China

² Changsha Haliang Kaishuai Precision Machinery Co., China

The duplex helical method has higher machining efficiency for face-milling spiral bevel and hypoid gears. An accurate and practical approach for calculating the basic machine-tool settings of spiral bevel and hypoid gears manufactured with the duplex helical method is proposed in the present work. The gear tooth surface vector functions and curvature parameters based on basic machine, and head-cutter settings are calculated. Two types of curvature parameters for pinion tooth surfaces are obtained by utilizing the conjugation of gear and pinion tooth surfaces, and the conjugation of pinion tooth surfaces and pinion head-cutter surfaces at the reference point. Next, the basic machine settings for generating pinions in accordance with the two types of curvature parameters for pinion tooth surfaces are determined. Finally, a numerical examples using the duplex helical method are performed and validated by comparing with experimental results. New hypoid gear software has been developed using the new approach.

Keywords: duplex helical method, spiral bevel and hypoid gears, face milling, basic machine settings, curvature parameter

Highlights

- A new exact calculation approach for basic machine-tool settings is proposed.
- Three reference points are used to determine the optimal machine settings.
- Based on the optimal approach tooth bearings and functions of transmission error on the both sides are favorable.
- Hypoid gear design software has been developed using the new approach.

0 INTRODUCTION

Spiral bevel and hypoid gear drives are widely employed as transmission elements in vehicles, aircrafts, ships, and other gear reducers. There are currently two main methods of producing spiral bevel [1] and hypoid gears [2] in the production environment: the single indexing method referred to as “face milling” [3], and the continuous indexing method referred to as “face hobbing” [4]. In both face milling and face hobbing, the gear may be cut using either a generating method or a non-generating (formate) method [4]. However, the pinion of a pair of mating hypoid gears is always cut using the generating method to satisfy the required contact characteristics. The non-generating method offers higher productivity than the generating method because the generating roll is eliminated in the former method. The manufacturing of face-milled spiral bevel and hypoid gear sets can be accomplished by using the five-cut process [5] or by using the duplex helical method or completing process [6]. The five-cut process consists of five independent operations: two operations to finish the gear, and three operations to finish the pinion [5].

Generalized theory and application of bevel and hypoid gears generated by the five-cut process have

been comprehensively presented by several gear scientists [7] to [9]. The generating method and the formate method of the five-cut process for face-milled spiral bevel and hypoid gears have been described in detail in [10] and [11]. Litvin et al. developed the principle and the calculation processes for the five-cut process independently in a manner that is different from Gleason’s technology described in [12] and [13]. Astoul et al. [14] presented a new design method of spiral bevel gears based on an optimization process to reduce their quasi-static transmission error. Cao et al. [15] proposed a new method to design pinion machine tool-settings for spiral bevel gears by controlling contact path and transmission errors based on the satisfaction of contact the condition of three given control points on the tooth surface. Su et al. [16] proposed a new approach to designing and implementing a seventh-order polynomial function of transmission error for spiral bevel gears in order to reduce the running vibration and noise of gear drive and improve the loaded distribution of the tooth.

Computerised design, manufacturing and simulation of meshing, and contact stress analysis of spiral bevel and hypoid gears are the subjects of research performed by many scientists [17] and [18]. Lin et al. [19] developed a numerical tooth contact

analysis technique for simulating the single flank test of the gear geometry data measured on a gear measuring centre. Fan developed a new generalized tooth surface generation algorithm and a tooth contact analysis (TCA) approach [3], and presented a new generic model of generating spiral bevel and hypoid gears, this model is applicable to both face-milling and face-hobbing processes based on the universal motion concept (UMC) [20]. Simon [21] presented a new method for computer-aided tooth contact analysis in mismatched spiral bevel gears. In addition, Tamizharasan and Senthil Kumar [22] proposed an attempt to minimize flank wear of uncoated carbide inserts while machining AISI 1045 steel by finite element analysis, this simulation method can provide a reference for the finite element simulation of spiral bevel and hypoid gears.

The principle and machining character of the duplex helical method are evidently different from that of the five-cut process. The cutters used for the duplex helical method have alternate (inside and outside) blades. The head cutter is mounted on the cradle that has a helical motion with respect to the gear blank; the work spindle is mounted on the sliding base that have an infeed motion with the rotation of the cradle. When a single cutter is used in one operation, both sides of the tooth slot are finished from a solid blank during machining. The advantages of using this method are as follow [6]: (1) the higher machining efficiency, (2) the assurance of uniform gears and, therefore, greater accuracy, since the size of the teeth is not dependent upon the manual controls of the operator, (3) the reduction of spoilage by manual mistake, and (4) the smoother bending of the bottom and sides of the teeth.

The duplex helical method was invented several decades earlier by Gleason [5], although only some formulas and calculating instructions for the duplex helical method for hypoid gears have been published. However, as Gleason's technology is confidential, the public has little knowledge of its principle and method in detail thus far. To the best knowledge of the authors of this paper, Gonzalez-Perez et al. dealt with conversion of the specific machine-tool settings of a given hypoid generator to the neutral machine-tool settings and adjustment the contact pattern by considering parabolic profiles on the blades of the head-cutter [23]. Fong proposed a mathematical model of a universal hypoid generator and applied it to simulate virtually all primary spiral bevel and hypoid cutting methods, including the duplex helical method, the supplemental kinematic flank correction motions, such as modified generating roll ratio, helical

motion, and cutter tilt were included in the proposed mathematical model [24].

In this paper, the authors present a new method that is used to accurately calculate basic machine-tool settings for formate hypoid gears. The new method aims to: (i) present the generalized theory of the duplex helical method in detail, (ii) obtain the desired meshing quality for the duplex helical method by using precise calculation.

1 CALCULATION OF BASIC MACHINE-TOOL SETTINGS FOR GENERATING GEAR

The coordinate system $S_m\{X_m, Y_m, Z_m\}$ is rigidly connected to the cutting machine (Fig. 1). The top, bottom (A-A) and right (B-B) of Fig. 1 are the machine front view, the machine bottom view and the side view (the projection of the head cutter). The cradle rotates about the Y_m axis; the \mathbf{p} axis and \mathbf{g} axis are projections of gear and pinion axes in the $X_mO_mY_m$ plane, respectively. The points M, M_1 and O_0 are the reference points of the tooth surface and the projection of M on the cutting edge and the centre of the head cutter, respectively. O_2 is the cross point of the gear, and O_m is the machine centre. The process for calculation of the machine-tool settings of the duplex helical method is the same as that of the five-cut process, details of which can be found in [10].

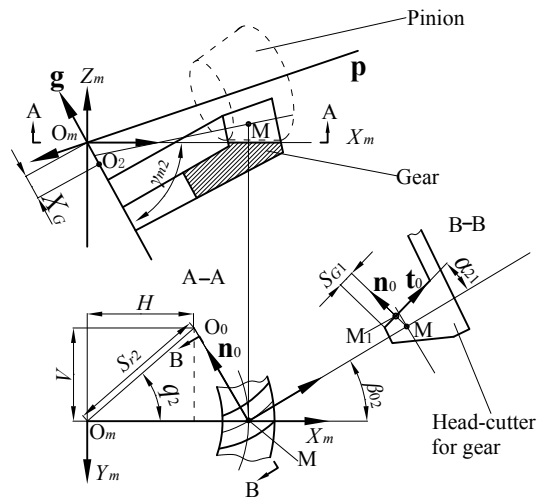


Fig. 1. Coordinate system applied for gear generation

The unit vectors of the Y_m axis, \mathbf{g} axis, and \mathbf{p} axis can be represented in the coordinate system S_m by the following equations:

$$\mathbf{e} = [0 \quad 1 \quad 0], \tag{1}$$

$$\mathbf{g} = [-\cos \gamma_{m2} \quad 0 \quad \sin \gamma_{m2}], \quad (2)$$

$$\mathbf{p} = [-\cos(\Sigma - \gamma_{m2}) \quad 0 \quad -\sin(\Sigma - \gamma_{m2})]. \quad (3)$$

The unit normal \mathbf{n}_0 , the unit vector \mathbf{t}_0 and the position vector \mathbf{a}_0 of a point on the outside blade edge of the gear to the head cutter-generating surface (drive or convex side) can be defined in the coordinate system S_m by the following equations:

$$\mathbf{n}_0 = [-\cos \alpha_{21} \sin \beta_{02} \quad -\cos \alpha_{21} \cos \beta_{02} \quad -\sin \alpha_{21}], \quad (4)$$

$$\mathbf{t}_0 = [-\sin \alpha_{21} \sin \beta_{02} \quad -\sin \alpha_{21} \cos \beta_{02} \quad \cos \alpha_{21}], \quad (5)$$

$$\mathbf{a}_0(u) = u\mathbf{t}_0 + \begin{bmatrix} H - X_G \cos \gamma_{m2} + r_{cG1} \sin \beta_{02} \\ r_{cG1} \cos \beta_{02} - V \\ X_G \sin \gamma_{m2} \end{bmatrix}. \quad (6)$$

Here, u is a profile parameter. The position vector of point M_1 on the blade edge can be represented by $\mathbf{a}_0(s_{G1})$ when u is equal to s_{G1} as denoted in Fig. 1.

2 CALCULATION OF BASIC MACHINE-TOOL SETTINGS FOR GENERATING PINION

2.1 Calculation of Pinion Curvature Parameters Based on Gear Tooth Surfaces

To facilitate the description of this paper, the following definitions are made: Σ_2 is the gear tooth surface. Σ_1 is the pinion tooth surface. Σ_g is the gear head-cutter surface or the generating tooth surface of the gear. Σ_p is the pinion head-cutter surface or the generating tooth surface of the pinion. M_1 is the reference point of the drive side. M_2 is the reference point of the coast side. The pinion is the driving wheel and left hand, gear is the driven wheel and right hand. The driving side is the convex side of gear, the concave side of pinion, the inside blades of the gear head-cutter and the outside blades of the pinion head-cutter. The coast side is the concave side of the gear, the convex side of the pinion, the outside blades of the gear head-cutter and the inside blades of the pinion head-cutter.

The formate-cut gear tooth surface is a copy of the surface of the head-cutter, which is a surface of revolution. Therefore, the vectors $\mathbf{a}_0(s_{G1})$, \mathbf{t}_0 , \mathbf{n}_0 of generating gear are the same as the vectors of the gear tooth surface.

A rotation angle θ_1 of the gear about the \mathbf{g} -axis is necessary for tangency at M_1 of the gear and pinion tooth surfaces Σ_2 and Σ_1 . The position vector of the reference point (M_1) $\mathbf{r}_{1dr}(\theta_1)$, the unit normal $\mathbf{n}_{1dr}(\theta_1)$

and the unit vector $\mathbf{t}_{1dr}(\theta_1)$ in the pinion tooth surface can be represented as:

$$\mathbf{r}_{1dr}(\theta_1) = E\mathbf{e} + \mathbf{a}_1(\theta_1), \quad (7)$$

$$\mathbf{a}_1(\theta_1) = \mathbf{a}_0(s_{G1}) \cdot \mathbf{R}[\mathbf{g}, \theta_1], \quad (8)$$

$$\mathbf{n}_{1dr}(\theta_1) = \mathbf{n}_0 \cdot \mathbf{R}[\mathbf{g}, \theta_1], \quad (9)$$

$$\mathbf{t}_{1dr}(\theta_1) = \mathbf{t}_0 \cdot \mathbf{R}[\mathbf{g}, \theta_1]. \quad (10)$$

Here, $\mathbf{R}[\mathbf{g}, \theta_1]$ is a transformation matrix that denotes the rotation angle θ_1 about the vector \mathbf{g} . Unit vector \mathbf{e} is given in Eq. (1).

The vectors $\mathbf{a}_1(\theta_1)$, \mathbf{e} , \mathbf{g} , \mathbf{p} and are determined in the coordinate system $S_2 \{ \mathbf{t}_{1dr} \times \mathbf{n}_{1dr}, \mathbf{t}_{1dr}, \mathbf{n}_{1dr} \}$ by the following equations:

$$\mathbf{a}_2(\theta_1) = \mathbf{a}_1(\theta_1) \cdot \mathbf{M}_{2m}, \quad (11)$$

$$\mathbf{e}_2 = \mathbf{e} \cdot \mathbf{M}_{2m}, \quad (12)$$

$$\mathbf{g}_2 = \mathbf{g} \cdot \mathbf{M}_{2m}, \quad (13)$$

$$\mathbf{p}_2 = \mathbf{p} \cdot \mathbf{M}_{2m}. \quad (14)$$

Here, matrix \mathbf{M}_{2m} represents the coordinate transformation from S_m to S_2 .

The meshing equation for hypoid gears can be represented as:

$$f_{12}(\theta_1) = \mathbf{v}_{12}(\theta_1) \cdot \mathbf{n}_{1dr} = 0. \quad (15)$$

Here, the relative velocity \mathbf{v}_{12} of the gear and pinion tooth surfaces Σ_2 and Σ_1 at M_1 can be obtained from the abovementioned vectors. The parameter θ_1^* can be obtained by solving Eq. (15). The related parameters can be obtained by inserting the value of θ_1^* into Eqs. (7) to (11).

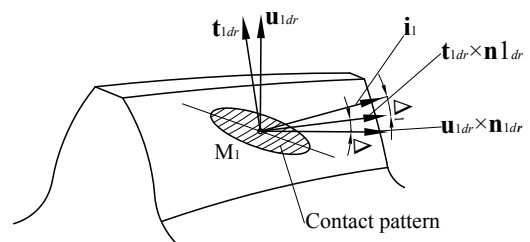


Fig. 2. The principal directions on the tangent plane

Fig. 2 shows the principal directions on the tangent plane at the reference point. The so-called first principal direction denotes the direction of maximum curvature of tooth surface; the second principal direction denotes the direction of minimum curvature of the tooth surface. In general, the two directions are perpendicular to each other. The first or second principal curvature or torsion is the curvature or

torsion in the corresponding first or second principal direction.

The first principal curvature A_2 in the gear tooth surface is represented as:

$$A_2 = \frac{1}{R_{n1}}. \quad (16)$$

Here, R_{n1} denotes the radius of curvature of the inside blade of the gear head-cutter. The first principal torsion B_2 and the second principal curvature C_2 of the gear tooth surface are equal to 0.

According to the Baxter method [25], the induced normal curvatures ΔA , ΔC , and torsion ΔC of the two conjugate tooth surfaces (Σ_2 and Σ_1) at M_1 can be represented as:

$$\theta_v = \theta_v(\theta_1^*), \quad (17)$$

$$\Delta C = \Delta C(\theta_1^*), \quad (18)$$

$$\Delta A = \Delta C \tan^2 \theta_v, \quad (19)$$

$$\Delta B = -\Delta C \tan \theta_v. \quad (20)$$

Here, the θ_v is the direction angle of the contact line that is formed between the tooth surfaces Σ_2 and Σ_1 , θ_v and ΔC can be obtained from the relative angular velocity ω_{12} , the relative velocity v_{12} , and the relative acceleration a_{12} of the gear and pinion tooth surfaces Σ_2 and Σ_1 at M_1 .

The first principal curvature A_0 , the first principal torsion B_0 , and the second principal curvature C_0 of the pinion tooth surface (drive side) at M_1 for the two principal directions of the gear tooth surface (Fig. 2) can be represented as:

$$\begin{cases} A_0 = A_2 - \Delta A \\ B_0 = -\Delta B \\ C_0 = -\Delta C \end{cases}. \quad (21)$$

Based on the generalised Euler and Bertrand formulas [13], the curvature parameters of the pinion tooth surface (drive side), along the two principal directions of the pinion tooth surface, can be represented as:

$$A_{1dr} = A_0 \cos^2 \Delta - 2B_0 \sin \Delta \cos \Delta + C_0 \sin^2 \Delta. \quad (22)$$

$$C_{1dr} = C_0 \cos^2 \Delta + 2B_0 \sin \Delta \cos \Delta + A_0 \sin^2 \Delta, \quad (23)$$

$$B_{1dr} = B_0 (\cos^2 \Delta - \sin^2 \Delta) + (A_0 - C_0) \sin \Delta \cos \Delta. \quad (24)$$

Here, Δ is the angle between the first principal direction of the gear tooth surface and the pinion tooth surface on the tangent plane (Fig. 2). \mathbf{u}_{1dr} can be represented as:

$$\mathbf{u}_{1dr} = (\mathbf{t}_{1dr} \times \mathbf{n}_{1dr}) \sin \Delta + \mathbf{t}_{1dr} \cos \Delta. \quad (25)$$

In the same way, all of the related parameters and vectors (including the curvature parameters A_{1co} , B_{1co} , C_{1co}) of the coast side of the pinion tooth surface can be obtained.

2.2 Calculation of Pinion Curvature Parameters Based on Pinion-Generating Surfaces

The configuration in Fig. 3 is the same as that in Fig. 1. The coordinate system $S_m \{X_m, Y_m, Z_m\}$ is rigidly connected to the cutting machine (Fig. 3). The top (A-A), bottom and middle of Fig. 3 are the machine front view, top view and side view (projection of the head cutter), respectively. The cradle rotates about the \mathbf{G} axis. The \mathbf{p} axis is the projection of the pinion spindle in the $X_m O_m Y_m$ plane. The points O_m , O_0 and O_1 are the machine centre, the centre of the head cutter, and the cross point of the pinion, respectively.

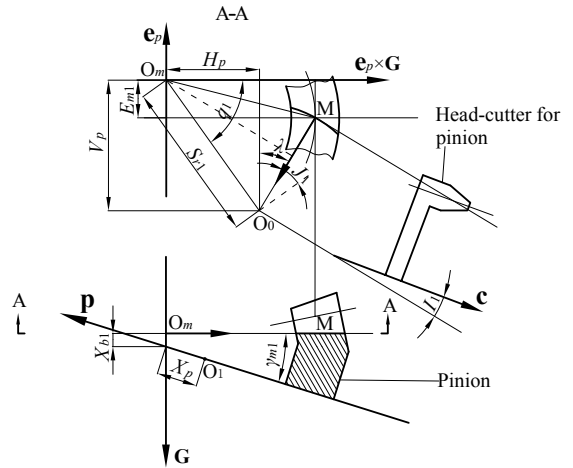


Fig. 3. Coordinate system applied for pinion generation

The manufacturing coordinate system of the gears and pinions and the installation coordinate system of the hypoid gear set are represented in the coordinate system S_m . Taking backlash and other factors into account, for tangency at the reference point M_2 of the gear and pinion tooth surfaces Σ_2 and Σ_1 , the position vector \mathbf{r}_2 of the reference point, the unit normal \mathbf{n}_2 and the unit vector \mathbf{u}_2 of the coast side of the pinion tooth surface at the reference point M_2 can be represented as:

$$\mathbf{r}_2 = \mathbf{r}_{1co} \cdot \mathbf{R}[\mathbf{p}, \theta_2], \quad (26)$$

$$\mathbf{n}_2 = \mathbf{n}_{1co} \cdot \mathbf{R}[\mathbf{p}, \theta_2], \quad (27)$$

$$\mathbf{u}_2 = \mathbf{u}_{1co} \cdot \mathbf{R}[\mathbf{p}, \theta_2]. \quad (28)$$

Here, the matrix $\mathbf{R}[\mathbf{p}, \theta_2]$ is a transformation matrix that denotes the rotation angle θ_2 (known parameter) about the vector \mathbf{p} .

The pinion cradle spindle \mathbf{G} does not always coincide with the Y_m axis (Fig. 3), and it can be represented in the coordinate system S_m as:

$$\mathbf{G} = \mathbf{G}(\alpha_{G1}, \gamma_{m1}). \quad (29)$$

The position vector of the reference point M_1 and the unit vector of the blank offset direction of the generating gear and the pinion can be represented in the coordinate system S_m as:

$$\mathbf{a}_{p1}(X_p, E_{m1}) = \mathbf{r}_{1dr} + X_p \mathbf{p} + E_{m1} \mathbf{e}_p, \quad (30)$$

$$\mathbf{e}_p = \mathbf{e}_p(\alpha_{G1}, \gamma_{m1}). \quad (31)$$

The relative velocity \mathbf{v}_{p1} of the generating gear and pinion tooth surfaces Σ_p and Σ_1 at M_1 can be obtained using the vectors \mathbf{G} , \mathbf{a}_{p1} , \mathbf{p} , \mathbf{r}_{1dr} . This can be represented as:

$$\mathbf{v}_{p1} = \mathbf{v}_{p1}(\alpha_{G1}, \gamma_{m1}, X_p, E_{m1}, H_l, R_{a1}). \quad (32)$$

Here, α_{G1} , γ_{m1} , X_p , E_{m1} , H_l , R_{a1} , are unknown parameters.

The meshing equation for the generating gear and pinion tooth surfaces at M_1 may be represented in the coordinate system S_m as:

$$f_{p1} = f_{p1}(\alpha_{G1}, \gamma_{m1}, X_p, E_{m1}, H_l, R_{a1}) = \mathbf{v}_{p1} \cdot \mathbf{n}_{1dr} = 0. \quad (33)$$

Based on Eq. (33), R_{a1} can be obtained using the following equation:

$$R_{a1} = f_{p1}(\alpha_{G1}, \gamma_{m1}, X_p, E_{m1}, H_l). \quad (34)$$

To perform tangency at M_1 or M_2 of the pinion tooth surface Σ_1 and the pinion head-cutter surface Σ_p , a rotation angle θ_3 of the pinion about the \mathbf{p} axis and a rotation angle θ_3/R_{a1} of generating gear about the \mathbf{G} axis are necessary (Fig. 3). The position vector from the reference point to the crossing point \mathbf{r}_4 , the position vector from the reference point to the machine centre \mathbf{a}_4 , the unit normal \mathbf{n}_4 and the unit vector \mathbf{u}_4 of the coast side of the pinion tooth surface at the reference point M_2 can be represented as:

$$\mathbf{r}_4 = \mathbf{r}_2 \cdot \mathbf{R}[\mathbf{p}, \theta_3], \quad (35)$$

$$\mathbf{n}_4 = \mathbf{n}_2 \cdot \mathbf{R}[\mathbf{p}, \theta_3], \quad (36)$$

$$\mathbf{u}_4 = \mathbf{u}_2 \cdot \mathbf{R}[\mathbf{p}, \theta_3], \quad (37)$$

$$\mathbf{a}_4 = \mathbf{r}_4 + X_p \mathbf{p} + E_{m1} \mathbf{e}_p. \quad (38)$$

Here, matrix $\mathbf{R}[\mathbf{p}, \theta_3]$ is a transformation matrix that denotes the rotation angle θ_3 (unknown parameter) about the vector \mathbf{p} .

Based on Eqs. (33) and (34), θ_3^* can be obtained by solving the meshing equation for the coast sides of the generating gear and pinion tooth surfaces at M_2 . The angle θ_3^* can be obtained using the following equation:

$$\theta_3^* = \theta_3^*(\alpha_{G1}, \gamma_{m1}, X_p, E_{m1}, H_l). \quad (39)$$

Given a rotation angle θ_3^*/R_{a1} of the pinion-generating surface about the G -axis, the position vector \mathbf{a}_6 and the unit normal \mathbf{n}_6 can be represented as:

$$\begin{aligned} \mathbf{a}_6(\alpha_{G1}, \gamma_{m1}, X_p, E_{m1}, H_l) &= \\ &= H_l \frac{\theta_3^*}{R_{a1}} \mathbf{G} + \mathbf{a}_4 \cdot \mathbf{R} \left[\mathbf{G}, \frac{\theta_3^*}{R_{a1}} \right], \end{aligned} \quad (40)$$

$$\mathbf{n}_6(\alpha_{G1}, \gamma_{m1}, X_p, E_{m1}, H_l) = \mathbf{n}_4 \cdot \mathbf{R} \left[\mathbf{G}, \frac{\theta_3^*}{R_{a1}} \right]. \quad (41)$$

The unit vector of the pinion head-cutter axis can be obtained using the vectors \mathbf{a}_6 , \mathbf{n}_6 , \mathbf{a}_{p1} , \mathbf{n}_1 , and can be represented as:

$$\mathbf{c} = \mathbf{c}(\alpha_{G1}, \gamma_{m1}, X_p, E_{m1}, H_l, r_{n1}, r_{n2}). \quad (42)$$

The unit vector of the first principal directions of the pinion-generating surface at M_1 can be represented as:

$$\mathbf{i}_1 = \frac{\mathbf{c} \times \mathbf{n}_{1dr}}{|\mathbf{c} \times \mathbf{n}_{1dr}|}. \quad (43)$$

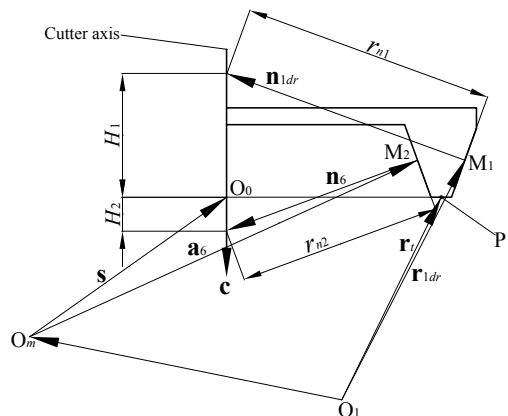


Fig. 4. Projection of pinion head-cutter in the coordinate system S_m

As in Eqs. (11) to (14), the parameters and vectors of the gear and pinion tooth surfaces are replaced by the parameters and vectors of the pinion-generating surface and the pinion tooth surface. Thus, the vectors $\mathbf{a}_3, \mathbf{e}_3, \mathbf{G}_3$ and \mathbf{p}_3 are obtained in the coordinate system $S_1 \{\mathbf{i}_1, \mathbf{n}_1 \times \mathbf{i}_1, \mathbf{n}_1\}$ from the vectors $\mathbf{a}_{p1}, \mathbf{e}_p, \mathbf{G}, \mathbf{p}$. Relative angular velocity $\boldsymbol{\omega}_{p1}$, relative velocity \mathbf{v}_{p1} , relative acceleration \mathbf{a}_{p1} of generating gear and pinion can be obtained from the abovementioned vectors.

The first principal curvature of the pinion-generating surface are represented as:

$$A_{pdr} = \frac{1}{r_{n1}}. \quad (44)$$

The first principal torsion B_{pdr} and the second principal curvature C_{pdr} of the pinion-generating surface are equal to 0. As in Eqs. (17) to (21), the curvature parameters of the pinion tooth surface, along the principal directions of the pinion-generating surface can be obtained.

The angle Δ_1 that is formed between the first principal directions of the pinion-generating surface and the pinion tooth surface on the tangent plane can be represented as:

$$\sin \Delta_1 = \mathbf{u}_1 \cdot \mathbf{i}_1. \quad (45)$$

As in Eqs. (22) to (24), the curvature parameters $A'_{1dr}, B'_{1dr}, C'_{1dr}$ of the pinion tooth surface, along the principal directions of the pinion tooth surface, can be obtained using the generalised Euler and Bertrand formulas.

In the same way, all of the related parameters and vectors (including the curvature parameters $A'_{1co}, B'_{1co}, C'_{1co}$) of the coast side of the pinion tooth surface can be obtained.

2.3 Determination of Basic Machine-Tool Settings for Generating the Pinion

The theoretical outside and inside blade angles for the pinion can be represented as: (see Fig. 4)

$$\sin \alpha_{b1} = -\mathbf{c} \cdot \mathbf{n}_{1dr}, \quad (46)$$

$$\sin \alpha_{b2} = -\mathbf{c} \cdot \mathbf{n}_c. \quad (47)$$

Theoretically, the curvature parameters of the pinion tooth surfaces along the principal directions of the pinion tooth surface should be the same as that determined by the two abovementioned methods; the theoretical outside and inside blade angles for the pinion should also be equal to the actual blade angles of the head-cutter for the generating pinion. Therefore, the seven equations can be written as follows:

$$\begin{cases} f_b^2 A'_{1dr} + A'_{1co} = f_b^2 A_{1dr} + A_{1co} \\ B'_{1dr} = B_{1dr} \\ C'_{1dr} = C_{1dr} \\ B'_{1co} = B_{1co} \\ C'_{1co} = C_{1co} \\ \alpha_{b1} = \alpha_{11} \\ \alpha_{b2} = \alpha_{12} \end{cases}. \quad (48)$$

Here, f_b denotes the tooth-bearing length unbalancing factor. The seven unknown parameters ($\alpha_{G1}, \gamma_{m1}, X_p, E_{m1}, H_1, r_{n1}, r_{n2}$) can be obtained by solving Eq. (48).

The position vector of the pinion head-cutter generating surface at the blade tip midpoint P can be represented as:

$$\mathbf{r}_t = h_{fm1} \mathbf{c} + 0.5(\mathbf{r}_{1dr} + \mathbf{r}_2). \quad (49)$$

Here, h_{fm1} denotes the pinion mean dedendum in the hypoid gear dimensions.

The position vector of the pinion head-cutter centre O_0 can be represented as:

$$\mathbf{s} = r_{n1} \mathbf{n}_{1dr} + \mathbf{r}_{1dr} + H_1 \mathbf{c} - X_p \mathbf{p} - E_{m1} \mathbf{e}_p, \quad (50)$$

$$H_1 = \mathbf{c} \cdot (\mathbf{r}_t - r_{n1} \mathbf{n}_{1dr} - \mathbf{r}_{1dr}). \quad (51)$$

Here, H_1 denotes the projection distance of M_1 on the pinion head-cutter axis.

A rotation angle θ_4 of the pinion-generating surface about the \mathbf{G} axis is necessary for meshing the contact of the pinion-generating surface and the tooth surface at P. The value of θ_4^* can be obtained by solving the meshing equation.

The root angle of the pinion δ_r can be represented as:

$$\sin \delta_r = \mathbf{p} \cdot \mathbf{n}_{pm}(\theta_4^*). \quad (52)$$

Here, $\mathbf{n}_{pm}(\theta_4^*)$ denotes the unit normal vector after a rotation angle of the pinion-generating surface about the \mathbf{G} axis θ_4^* .

Generally, δ_r is not equal to the root angle δ_{f1} of the hypoid gears' blank dimensions. Therefore, the resulting new mean dedendum b_{m1} of the pinion is different from the mean dedendum h_{fm1} of the hypoid gears' blank dimensions. Using the modified mean dedendum b_{m1} , the vectors \mathbf{r}_t, \mathbf{s} and H_1 should be recalculated.

The outside and inside cutter point radii for the pinion can be obtained as follows:

$$r_{cp1} = \frac{r_{n1}}{\cos \alpha_{b1}} - H_1 \tan \alpha_{b1}, \quad (53)$$

$$r_{cp2} = \frac{r_{n2}}{\cos \alpha_{b2}} - H_2 \tan \alpha_{b2}. \quad (54)$$

After a rotation angle θ_4^* of the pinion-generating surface about the \mathbf{G} axis, the position vector of the pinion head-cutter centre and the unit vector of the pinion head-cutter axis \mathbf{c}_1 can be redefined as:

$$\mathbf{s}_x = \mathbf{s} \cdot \mathbf{R}[\mathbf{G}, \theta_4^*] + H_1 \theta_4^* \mathbf{G}, \quad (55)$$

$$\mathbf{c}_1 = \mathbf{c} \cdot \mathbf{R}[\mathbf{G}, \theta_4^*]. \quad (56)$$

The rest of the basic machine settings for the pinion can be obtained as follow:

$$X_{b1} = -\mathbf{s}_x \cdot \mathbf{G}, \quad (57)$$

$$H_p = \mathbf{s}_x \cdot (\mathbf{e}_p \times \mathbf{G}), \quad (58)$$

$$V_p = -\mathbf{s}_x \cdot \mathbf{e}_p, \quad (59)$$

$$\sin I_1 = |\mathbf{c} \times \mathbf{G}|. \quad (60)$$

3 NUMERICAL EXAMPLE

In this section, a hypoid gear design software based on the abovementioned calculation strategy for basic machine-tool settings was developed; the software development flow chart is shown in Fig. 5.

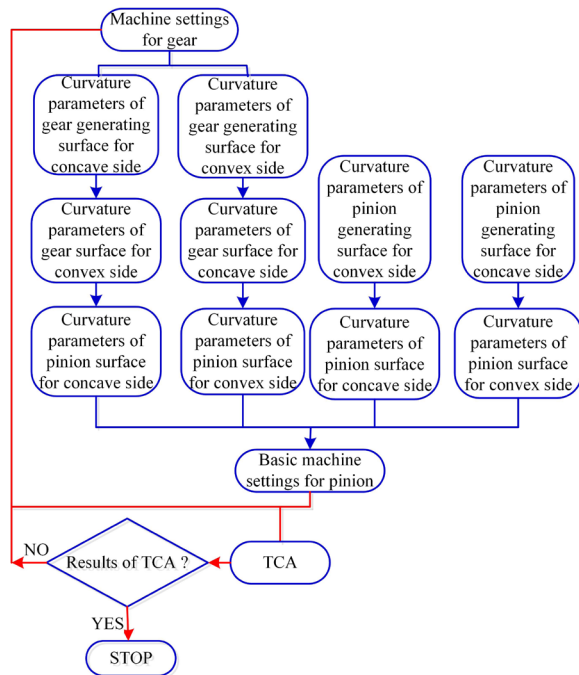


Fig. 5. Spiral bevel and hypoid gear design software development flow chart

The theoretical analysis is performed based on a hypoid gear set generated by using the duplex helical method. The design parameters for the face-milled hypoid gear set are listed in Table 1. The basic machine settings are listed in Table 2.

Table 1. Design data

Design features	Pinion	Gear
Number of teeth	7	43
Module [mm]		6.861
Face width [mm]	43.73	40.00
Pinion offset [mm]	25.4	
Shaft angle [°]	90	
Mean spiral angle [°]	45	33.75
Hand of spiral	LH	RH
Cutter radius [mm]	114.3543	114.3

Table 2. Basic machine settings for the duplex helical method

Applied settings	Pinion	Gear
Radial distance [mm]	114.2545	117.4921
Tilt angle [°]	15.7363	0.0000
Swivel angle [°]	-31.6295	0.0000°
Blank offset [mm]	25.0224	0.0000
Machine root angle [°]	-9.0996	70.2509
Machine centre to cross point [mm]	0.3431	9.6518
Sliding base [mm]	23.8256	0.0000
Ratio of roll	5.9651	0.0000
Cradle angle [°]	66.8700	70.9771
Helical motion velocity coeff [mm/rad]	11.5478	0.0000

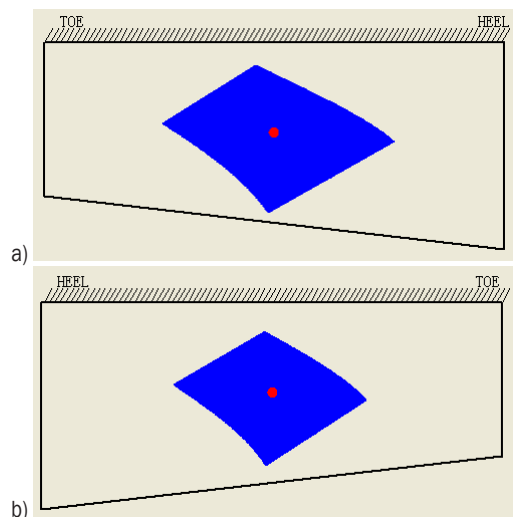


Fig. 6. Tooth bearings for the hypoid gear drive 7x43; a) drive side, and b) coast side

Figs. 6 and 7 show the tooth bearings and the transmission error functions on the drive and coast side by the duplex helical method for the hypoid gear

drive 7×43 (number of pinion teeth×number of gear teeth), respectively. In Fig. 6, the red point is the first contact point or reference point. It is observed that a continuous and negative function is obtained for transmission errors, with a maximum level on the drive side for the method of approximately 15.5" (0.004306°), and on the coast side of approximately 15.9" (0.004417°).

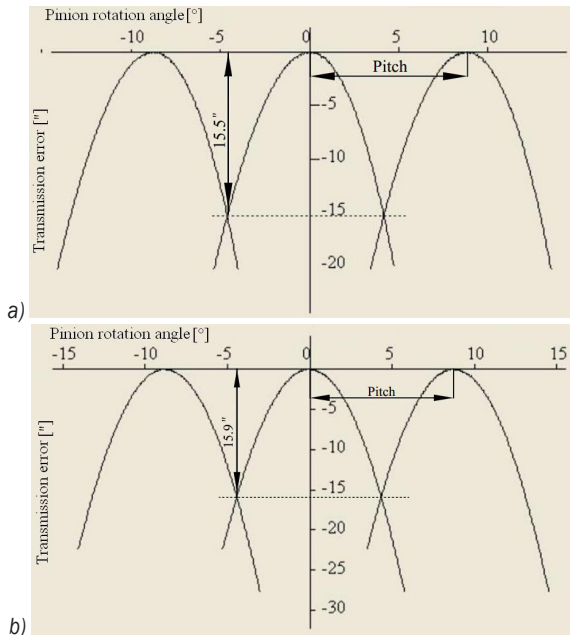


Fig. 7. Function of transmission errors for the hypoid gear drive 7×43; a) drive side, and b) coast side

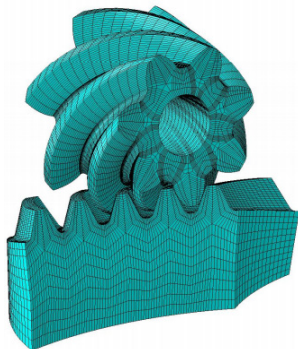


Fig. 8. Finite element model for the hypoid gear drive 7×43

The load history, especially the transfer of load between neighbouring gear pairs, is very helpful for understanding the gear mesh characteristics. Fig. 8 shows a finite element mesh; five teeth of the gear are used to save costs. Fig. 9 show the evolution of contact stresses of the pinion and gear by the method for the hypoid gear drive. The torque and the rotational speed

applied to the pinion are 500 Nm and 1000 r/min, respectively.

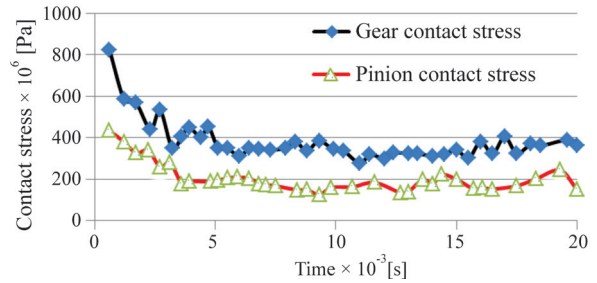


Fig. 9. Evolution of contact stresses for the hypoid gear drive 7×43



Fig. 10. Tooth bearings on the hypoid gear test machine for the hypoid gear drive 7×43; a) drive side, and b) coast side

The analysis of the comparison of contact stress evolution is as follows:

- (1) There is higher contact stress due to impact in the initial phase; with the smoothing of the rotational speed, contact stress is gradually stabilizing in Fig. 9.
- (2) The maximum gear tooth contact stress for the hypoid gear drive is about 300 MPa to 400 MPa; the maximum pinion tooth contact stress is about 150 MPa to 200 MPa after 4.5 ms. There is no problem of the appearance of areas of severe contact stress and edge contact throughout the process.

To verify the effectiveness of the generalized theory of the duplex helical method, the cutting and the rolling test experiments are done. Fig. 10 shows the tooth bearings on the hypoid gear test machine for the

hypoid gear drive 7×43 by the duplex helical method. The results of the rolling test and the results of TCA in Fig. 6 are carried out under light load. The shape and location of the tooth bearings in Fig. 10 are basically consistent with those in Fig. 6. The experiment results achieve the desired effect. Finally, all of the results proved the correctness of the generalized theory of the duplex helical method described in this paper.

4 CONCLUSIONS

The duplex helical method is an advanced and primary manufacturing method of face-milled spiral bevel and hypoid gears. It is a completing process in which the concave and convex tooth surfaces are generated simultaneously under a single set of machine settings, and it is difficult to obtain a set of optimal machine settings that can ensure both sides of TCA with good characteristics. To solve the problem, some valid conclusions are obtained through this investigation:

- (1) A general calculation method of the basic machine settings for all spiral bevel and hypoid cutting methods, including face-milling and face-hobbing, is proposed.
- (2) Three reference points (M_1 , M_2 , P) are used to calculate basic machine-tool settings for forming hypoid gears manufactured by the duplex helical method; they can accurately control the position and movement relationships between the generating gear and pinion.
- (3) The TCA and rolling test experiment results of the hypoid gear set manufactured by the duplex helical method show that the new methodology for calculating the basic machine settings achieves the desired effect. Both sides of TCA results have good characteristics.

5 NOMENCLATURE

Σ	shaft angle [°]
E	pinion offset (mm)
γ_{m2}	machine root angle of gear [°]
X_G	machine centre to back of gear [mm]
H	horizontal setting of gear head-cutter [mm]
V	vertical setting of gear head-cutter (mm)
q_2	cradle angle of gear [°]
S_{r2}	radial distance of gear [mm]
α_{21}	inside blade pressure angle (drive side or convex side) for gear [°]
α	outside blade pressure angle (drive side or concave side) for pinion [°]
α_{12}	inside blade pressure angle (coast side or convex side) for pinion [°]

β_{02}	spiral angle of the gear generating surface [°]
r_{cG1}	cutter point radius for the convex side of the gear [mm]
ΔA	the first induced normal curvature of two conjugate tooth surfaces (Σ_2 and Σ_1) at M_1
ΔB	the first induced normal torsion of two conjugate tooth surfaces (Σ_2 and Σ_1) at M_1
ΔC	the second induced normal curvature of two conjugate tooth surfaces (Σ_2 and Σ_1) at M_1
α_{G1}	pressure angle of drive side of pinion-generating surface [°]
H_p	horizontal setting for pinion head-cutter [mm]
V_p	vertical setting for pinion head-cutter [mm]
E_{m1}	blank offset for the pinion [mm]
X_p	machine centre to back for pinion [mm]
X_{b1}	sliding base for pinion [mm]
γ_{n1}	machine root angle for pinion [°]
S_{r1}	radial distance for pinion head-cutter [mm]
q_1	cradle angle for pinion [°]
I_1	tilt angle for pinion head-cutter [°]
J_1	swivel angle for pinion head-cutter [°]
R_{a1}	ratio-of-roll of pinion and generating gear
H_1	helical motion velocity coefficient represents a displacement of the pinion blank along the axis of the cradle for a rotational angle of 1 radian of the cradle [mm/rad]
r_{n1}	curvature radius of the outside blade of the pinion head-cutter (drive side or concave side) [mm]
r_{n2}	curvature radius of the inside blade of the pinion head-cutter (coast side or convex side) [mm]

Subscripts

1	pinion
2	gear
G	generating surface of gear
p	generating surface of pinion
dr	drive side
co	coast side

6 ACKNOWLEDGEMENTS

The authors express their deep gratitude to the National Natural Science Foundation of China (NSFC) (No. 51575533), National Key Basic Research Program of China (973 Program) (NKBRP) (No. 2011CB706800-G), Specialized Research Fund for the Doctoral Program of Higher Education (SRFDP) (No. 20120162110004) and National Natural Science Foundation of China (NSFC) (No. 51375159) for the financial support of the research.

7 REFERENCES

- [1] Stadtfeld, H. (2011). Tribology aspects in angular transmission systems part IV: spiral bevel gears. *Gear Technology*, no. January/February, p. 66-72.
- [2] Stadtfeld, H. (2011). Tribology aspects in angular transmission systems part VII: hypoid gears. *Gear Technology*, no. June/July, p. 66-72.
- [3] Fan, Q., Wilcox, L. (2007). New developments in tooth contact analysis (TCA) and loaded TCA for spiral bevel and hypoid gear drives. *Gear Technology*, no. May, p. 26-35.
- [4] Fan, Q. (2006). Computerized modeling and simulation of spiral bevel and hypoid gears manufactured by Gleason face hobbing process. *ASME Journal of Mechanical Design*, vol. 128, no. 6, p. 1315-1327, DOI:10.1115/1.2337316.
- [5] Gleason Works (2004). *Applied gear engineering - CAGEWin software customer/dealer training center*. The Gleason Works, Rochester.
- [6] Gleason Works (1971). *Calculation instructions generated hypoid gears duplex helical method*. The Gleason Works, New York.
- [7] Fan, Q. (2011). Optimization of face cone element for spiral bevel and hypoid gears. *Journal of Mechanical Design, Transactions of the ASME*, vol. 133, no. 9, p. 091002-091001-091002-091007, DOI:10.1115/1.4004546.
- [8] Zhang, Y., Litvin, F.L. (1995). Computerized design of low-noise face-milled spiral bevel gears. *Mechanism Machine Theory*, vol. 30, no. 8, p. 1171-1178, DOI:10.1016/0094-114X(95)00052-Z.
- [9] Wang, J., Kong, L., Liu, B., Hu, X., Yu, X., Kong, W. (2014). The mathematical model of spiral bevel gears - A review. *Strojniški vestnik - Journal of Mechanical Engineering*, vol. 60, no. 2, p. 93-105, DOI:10.5545/sv-jme.2013.1357.
- [10] Shtipelman, B.A. (1978). *Design and Manufacture of Hypoid Gears*. A Wiley-Interscience Publication, New York.
- [11] Fuentes, A., Gonzalez-Perez, I., Litvin, F.L., Hayasaka, K., Yukishima, K. (2007). Determination of basic machine-tool settings for generation of spiral bevel gears from blank data. *Proceedings of the ASME International Design Engineering Technical Conferences and Computers and Information in Engineering Conference*, p. 57-68, DOI:10.1115/detc2007-34038.
- [12] Litvin, F.L., Zhang, Y., Lundy, M., Heine, C. (1988). Determination of settings of a tilted head cutter for generation of hypoid and spiral bevel gears. *ASME Journal of Mechanisms, Transmissions, and Automation in Design*, vol. 110, no. 4, p. 495-500, DOI:10.1115/1.3258950.
- [13] Litvin, F.L., Fuentes, A. (2004). *Gear geometry and Applied Theory* (2nd edition). Cambridge University Press, New York, DOI:10.1017/CB09780511547126.
- [14] Astoul, J., Mermoz, E., Sartor, M., Linares, J.M., Bernard, A. (2014). New methodology to reduce the transmission error of the spiral bevel gears. *CIRP Annals - Manufacturing Technology*, vol. 63, no. 1, p. 165-168, DOI:10.1016/j.cirp.2014.03.124.
- [15] Cao, X.M., Fang, Z.D., Xu, H., Su, J.Z. (2008). Design of pinion machine tool-settings for spiral bevel gears by controlling contact path and transmission errors. *Chinese Journal of Aeronautics*, vol. 21, no. 2, p. 179-186, DOI:10.1016/S1000-9361(08)60023-0.
- [16] Su, J.Z., Fang, Z.D., Cai, X.W. (2013). Design and analysis of spiral bevel gears with seventh-order function of transmission error. *Chinese Journal of Aeronautics*, vol. 26, no. 5, p. 1310-1316, DOI:10.1016/j.cja.2013.07.012.
- [17] Sobolewski, B., Marciniak, A. (2013). Method of spiral bevel gear tooth contact analysis performed in CAD environment. *Aircraft Engineering and Aerospace Technology*, vol. 85, no. 6, p. 467-474, DOI:10.1108/AEAT-11-2012-0207.
- [18] Litvin, F.L., Fuentes, A., Hayasaka, K. (2006). Design, manufacture, stress analysis, and experimental tests of low-noise high endurance spiral bevel gears. *Mechanism and Machine Theory*, vol. 41, p. 83-118, DOI:10.1016/j.mechmachtheory.2005.03.001.
- [19] Lin, C.H., Fong, Z.H. (2015). Numerical tooth contact analysis of a bevel gear set by using measured tooth geometry data. *Mechanism and Machine Theory*, vol. 84, p. 1-24, DOI:10.1016/j.mechmachtheory.2014.09.010.
- [20] Fan, Q. (2007). Enhanced algorithms of contact simulation for hypoid gear drives produced by face-milling and face-hobbing processes. *ASME Journal of Mechanical Design*, vol. 129, no. 1, p. 31-37, DOI:10.1115/1.2359475.
- [21] Simon, V. (2007). Computer simulation of tooth contact analysis of mismatched spiral bevel gears. *Mechanism and Machine Theory*, vol. 42, no. 3, p. 365-381, DOI:10.1016/j.mechmachtheory.2006.02.010.
- [22] Tamizharasan, T., Senthil Kumar, N. (2012). Optimization of cutting insert geometry using DEFORM-3D: Numerical simulation and experimental validation. *International Journal of Simulation Modelling*, vol. 11, no. 2, p. 65-75, DOI:10.2507/IJSIMM11(2)1.200.
- [23] Gonzalez-Perez, I., Fuentes, A., Hayasaka, K. (2011). Computerized design and tooth contact analysis of spiral bevel gears generated by the duplex helical method. *ASME International Design Engineering Technical Conferences and Computers and Information in Engineering Conference*, p. 149-158, DOI:10.1115/detc2011-47108.
- [24] Fong, Z.H. (2000). Mathematical model of universal hypoid generator with supplemental kinematic flank correction motions. *ASME Journal of Mechanical Design*, vol. 122, no. 3, p. 136-142, DOI:10.1115/1.533552.
- [25] Baxter, M.L. (1973). Second-order surface generation. *Industrial Mathematics*, vol. 23, no. 2, p. 85-106.

High-Frequency Calibration of Piezoelectric Displacement Sensors Using Elastic Waves Induced by Light Pressure

Jernej Laloš* – Tomaž Požar – Janez Možina

University of Ljubljana, Faculty of Mechanical Engineering, Slovenia

In the study of ultrasound propagation in matter, displacement sensors are indispensable and of these, the most sensitive are piezoelectric sensors. In order to eliminate the intrinsic effects of the sensor from the measurements, the sensor has to be properly calibrated, which means that its transfer function has to be evaluated from a known sensor input signal and a measured sensor output signal. This has usually been done by comparing the sensor response signal to a known input signal, namely, an ultrasonic waveform, which can be theoretically calculated using mathematical models and numerical algorithms. Until now, the point-source-point-sensor model has been primarily used, while ultrasonic waves were induced mechanically either by a dropped ball or a capillary fracture. In this paper, a real-source-real-sensor model is presented. It provides a more faithful waveform construction and it enables the removal of the aperture effect from the calculated sensor transfer function, thus giving correct and universal sensor response characteristics. This was corroborated by high-frequency calibration measurements of the output signal of a Glaser-type conical sensor in two positions on both surfaces of a glass plate, while ultrasonic waves were induced by the radiation pressure of a nanosecond laser pulse.

Keywords: absolute sensor calibration, piezoelectric sensor, laser pulse, aperture effect, elastic waves in a plate, optodynamics, Green's function

Highlights

- An absolute, high-frequency calibration method of a Glaser-type piezoelectric displacement sensor.
- A way of incorporating the real dimensions of the sensor contact area and the stimulant signal origin area.
- Elimination of the sensor aperture effect and the source force distribution effect from the calculated transfer function.
- Detailed separation of spectral characteristics by their individual contributors.

0 INTRODUCTION

Displacement measurements are indispensable in the study of ultrasound propagation in matter. Such measurements may be carried out using sensors that operate through transduction mechanisms based on piezoelectric, electrostatic, electromagnetic or optical (mainly light interferometric) principles [1]. Of these, piezoelectric sensors are the most sensitive [2], making them especially applicable for low-amplitude measurements (~ 1 pm).

Piezoelectric sensors are being used in mechanical engineering, as well as for scientific and technological research. They are used for acoustic emission testing [3] and [4] and nondestructive examination of materials [4] and [5], in microseismology [6] and [7], wave propagation studies [8], light-matter interaction studies [9] and [10], optodynamics [11], and many other applications.

For the measurements to be accurate, it is essential that the sensor is properly calibrated [12]. Its transfer function has to be known so that the sensor's intrinsic effects can be removed from its output signal and displacement measurements exclusively obtained.

Sensor calibration should be carried out uniquely for the material on which the sensor is intended to perform future measurements. While each material has its specific acoustic impedance, an equal mechanical disturbance may produce a different sensor displacement due to their impedance mismatch.

Such calibrations have usually been carried out by comparing the response of the sensor under consideration to a known stimulant signal, namely, a surface waveform, which has been either measured by another, precalibrated sensor or calculated theoretically [12] and [13]. With the use of a precalibrated sensor, both calibrations have to be carried out using the same materials, the same sensor apertures and at the same relative positions. While this is also true for the theoretical calculation, the latter is more universal and less laborious as the parameters are easily changed in the model. Until now, the theoretical waveform calculation has been mostly carried out using mathematical approximations which consider the sensor contact area and the stimulant signal origin area to be mere points and not of real size. This was done, because such approximations were valid as the frequencies of interest were sufficiently low. For the stimulant waveform origin, a dropped ball

[13] and [14], a glass capillary fracture [13] and [15] or a pencil lead break [5] has usually been used [1], and [3]. In these cases, the contact times are rather long (about 1 μs for a dropped ball and 200 ns for a capillary fracture) and their force distributions, while concentrated in a relatively small impact area (with an estimated order of magnitude of about 10 μm to 100 μm [16]), may not be uniform over time and both may vary slightly with each repetition. All of this makes such calibrations credible only for signal wavelengths larger than the sizes of the signal origin and the sensor contact areas, which, quite undesirably, caps the calibration frequencies and results in inaccurate spectral transfer functions. Thus, the sensor aperture effect and the source force distribution effect are not addressed entirely as they are mostly avoided [13].

In this paper, an absolute high-frequency calibration of the piezoelectric Glaser-type conical sensor [1] and [3] is presented. An absolute calibration is possible, because such sensors operate without resonance and have the flattest response function among piezoelectric sensors [1]. Although this technique follows the general guidelines presented in the standard [12] and in the paper by McLaskey and Glaser [13], it improves upon them with several new features: an optodynamic interaction as the source force of the stimulant ultrasonic signal with an expanded mathematical model that incorporates real dimensions of the sensor contact area and the source force impact area and can allocate the signal's spectral characteristics to each individual contributor.

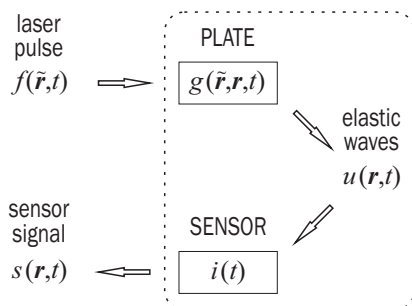


Fig. 1. Schematics of mathematical transition from the source force impulse through the plate transfer function, surface waveform and sensor transfer function to the sensor voltage output signal

The main advantage of using a laser pulse to induce the stimulant signal is that it has a very short temporal distribution and a known spatial intensity profile – both of which are independent from each other – which produces a well-determined force impulse while being consistently repeatable. The use

of a laser pulse also enables a controlled size variation of the source force impact area, which in turn allows variation in the stimulant signal frequency range. In this calibration, for example, the size of the impact area is relatively large in order to demonstrate the incorporation of the macroscopic spatial extent of the source in the expanded model. It can be, however, reduced to only a few wavelengths of laser light, which is about an order of magnitude less than from any known mechanical device, thus approximating a δ -source as closely as possible. Such concentration of laser light has to be used with caution, though, as the high fluence may exceed the laser-induced-damage threshold and the specimen, along with any surface coating on it, may become damaged.

The expanded mathematical model enables the proper stimulant waveform to be constructed and the sensor aperture effect [17] to be correctly accounted for, resulting in a proper and more accurate sensor spectral transfer function. The sensor can thus be correctly calibrated, even for higher frequencies than before, and used for measurement and identification of the individual wave-arrivals of ultrasonic waves in acoustic emission and laser ultrasound.

1 METHOD

In order for a sensor to be considered calibrated, the spectral characteristics of its transfer function have to be known. The essence of this method is, therefore, to theoretically calculate the displacement waveform that is detected by the sensor and compare it to the measured sensor output, as outlined in the standard [12] and in paper [13].

Due to the complicated nature of wave propagation in matter [8] and sensor transductivity mechanisms [15], it is convenient to introduce certain simplifications and idealizations to their mathematical description, such as the transfer function concept and the Green's function formalism.

Thus the plate and the sensor are each considered to have their own transfer functions, which transform a certain time t dependent input signal into a certain different output signal. Therefore, the plate has a transfer function $g(\tilde{r}, r, t)$ which transforms an input source force signal $f(\tilde{r}, t)$ at a position \tilde{r} into an output displacement signal $u(r, t)$ at another position r . Similarly, the sensor has a transfer function $i(t)$ which transforms an input displacement signal $u(r, t)$ to an output voltage signal $s(r, t)$. The schematics of this linear transform chain are shown in Fig. 1.

Both transfer functions are considered to be algebraically linear and time invariant. This is

significant as it allows for the output signal to be expressed as a time convolution of the input signal and the appropriate transfer function:

$$u(\mathbf{r}, t) = f(\tilde{\mathbf{r}}, t) * g(\tilde{\mathbf{r}}, \mathbf{r}, t), \quad (1)$$

$$s(\mathbf{r}, t) = u(\mathbf{r}, t) * i(t). \quad (2)$$

Since $s(\mathbf{r}, t)$ is measured and $u(\mathbf{r}, t)$ is theoretically calculated, it is useful to perform a Fourier transform deconvolution when searching for $i(t)$. Fourier transform of Eq. (2) gives:

$$S(\mathbf{r}, \omega) = U(\mathbf{r}, \omega) I(\omega). \quad (3)$$

To obtain the spectrum of the sensor transfer function $I(\omega)$, one must simply divide the other two transforms:

$$I(\omega) = \frac{S(\mathbf{r}, \omega)}{U(\mathbf{r}, \omega)}. \quad (4)$$

This is permissible because $U(\mathbf{r}, \omega)$ is not zero at any frequency $\omega \equiv 2\pi\nu$ where it is defined.

The plate transfer function $g(\tilde{\mathbf{r}}, \mathbf{r}, t)$ is a superposition of individually weighted Green's functions based upon the distance distribution between points in the source force area and the sensor contact area on the plate's surface. Green's functions, in general, are the solutions of wave equations for a δ -function source impulse and are highly specific for each material, shape and distance.

Each Green's function here is calculated using the modified numerical algorithm developed by Hsu [18]. It calculates Green's functions in the infinite plane-parallel plate approximation, which means that it accounts for the direct waves and the waves multiple reflected from the top or the bottom surface of the plate but not for those reflected from the sides of the finite plate.

Four distance distributions and four plate transfer functions are used and compared in the calibration discussion further on. One is a simple point-source-point-sensor (PP) model $g_{PP}(\tilde{\mathbf{r}}, \mathbf{r}, t)$ where both the source force and the sensor are considered to act upon and from only one point on plate's surface – such as it has been known and used until now [13]. The real-source-real-sensor (RR) model $g_{RR}(\tilde{\mathbf{r}}, \mathbf{r}, t)$ takes faithfully into account real dimensions of the source force impact area and the sensor contact area. The third and the fourth one are the point-source-real-sensor (PR) model $g_{PR}(\tilde{\mathbf{r}}, \mathbf{r}, t)$ and the real-source-point-sensor (RP) model $g_{RP}(\tilde{\mathbf{r}}, \mathbf{r}, t)$, which are in between the former two and are used to garner insight into the spectral characteristics and their contributors. Each of these plate transfer functions, of course,

produces its own waveform model and from each of those a different sensor transfer function is calculated.

Since the arrangement is such that the source force acts only normally on the plate's surface and the sensor is assumed to detect only out-of-plane displacements, only the z direction is of concern and only the g_{zz} component of the elastodynamic Green's tensor is used (this direction notation, however, is omitted for simplicity).

2 SENSOR CALIBRATION

The sensor used here is the piezoelectric Glaser-type conical sensor: 'SteveCo' KRNB-PC Point Contact Sensor, produced by KRN Services, Inc. [19]. This sensor is designed to detect small-scale, absolute out-of-plane displacements.

The detection element in this kind of a sensor is a piezoelectric crystal PZT-5A in the shape of a truncated cone covered with a nickel electrode and backed by a heavy brass mass of irregular shape surrounded by rubber and encased in a steel case [1]. The sensor is assumed to have a uniform sensitivity over its contact area, which is circular in shape with a radius of $r_{S0} = 0.5$ mm. The spatial distribution of the waveform under the sensor's aperture it therefore averaged out and combined into one output signal by the sensor. The geometric properties and electrical wiring of the sensor are specifically designed to minimize the ultrasonic and electromagnetic distorting effects. In this paper, all electrical support equipment, such as amplifiers, cables, and oscilloscope, are considered as part of the sensor.

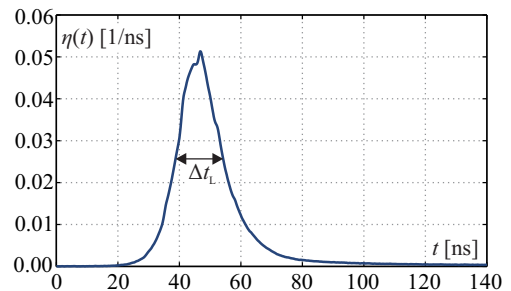


Fig. 2. Normalized temporal distribution of the incident laser pulse

The source force $f(\tilde{\mathbf{r}}, t)$ is the result of a laser pulse light pressure on the highly reflective mirror surface [9] and [10]. The laser pulse is produced by Nd:YAG laser of wavelength $\lambda_L = 1064$ nm and energy $E_L = 200$ mJ. The pulse, which was measured with a fast photodiode, has a very short temporal distribution $\eta(t)$ with a full-width-at-half-maximum of $\Delta t_L = 17$ ns, as shown in Fig. 2. It is circularly symmetric and has a

top-hat spatial profile [10] with a radius of $r_{L0} = 1.75$ mm on the plate's surface.

The substrate of the mirror is a plane-parallel disk-shaped glass plate made of UV-grade fused silica (SiO_2). It has a diameter of $d = 50$ mm and a thickness of $h = 12$ mm. Its elastic properties are: mass density $\rho = 2200$ kg/m³, Young's modulus $Y = 72$ GPa and Poisson's ratio $\mu = 0.17$. The top side of the plate is coated with a highly reflective (HR) layer with reflectivity of $R_{HR} > 99.8$ % at wavelength λ_L . This layer does not affect the reflection of the mechanical waves as its thickness is much smaller than the wavelength of even the shortest detected waves.

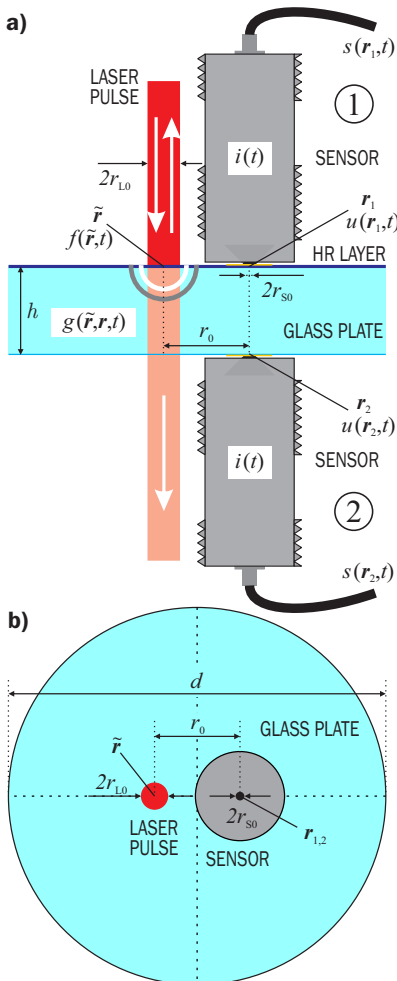


Fig. 3. Experimental setup schematic showing both positions of the piezoelectric sensor relative to the laser pulse as well as the most significant geometric properties in a) side view and in b) top view

The calibration arrangement is shown in Fig. 3. The laser pulse is incident on the top of the plate and is mostly reflected by the HR layer. The small amount

of light that does pass through the plate is absorbed only insignificantly. In this manner, the pulse delivers a force impulse of $J = 2E_L/c_0 = 1.33$ nNs normally to the plate's surface; where c_0 is the speed of light in vacuum. This impulse, in turn, generates elastic waves that propagate through the plate. These waves are therefore only light-pressure-induced and not thermoelastic or ablation-induced at all [9].

The sensor is deployed at two different positions during the calibration process. In position 1, at r_1 , it is placed on the top surface of the plate next to the laser pulse impact area at \tilde{r} with their respective centers $r_0 = 11.5$ mm apart. In position 2, at r_2 , the sensor is placed on the opposite side of the plate, directly beneath position 1.

In such an arrangement, waves reflected from the sides of the plate may reach the sensor as well: the earliest after about $8.0\mu\text{s}$ and the others well after $9.0\mu\text{s}$. It was experimentally found that the first one, the surface skimming P-wave, has such a low amplitude that it can be disregarded in this case. Therefore, for all practical purposes, the plate can be considered as infinitely large in the time period of at least the first $9.0\mu\text{s}$ after the laser pulse illumination.

Even a small amount of absorbed light by the PZT element greatly disturbs the elastic wave displacement measurement. For that reason, the sensor cannot be placed directly in the path of the laser pulse. To additionally minimize light absorption by the PZT element, a $20\text{-}\mu\text{m}$ -thick gold foil with some couplant was inserted between the sensor and the plate. This was done because gold has higher reflectivity ($R_{Au} = 99$ % [20] and [21]) at laser light wavelength λ_L than the nickel ($R_{Ni} = 73$ % [20] and [21]) that covers the sensor's tip.

The calibration measurements of the sensor output signal are averaged out of $N=200$ repetitions in each of the two sensor positions to reduce the stochastic noise and improve the signal-to-noise ratio. Each measurement has its start time set to zero by a photodiode with a rise time of 1 ns, which is triggered when the laser pulse illuminates the plate's surface. The sampling period is $\delta t=2$ ns while an individual measurement lasts $t_\Omega=9.0\mu\text{s}$, thus ending well before any significant waves reflected from the sides of the plate reach the sensor.

Since the waveform amplitudes are small, it is essential to reduce the noise in the measurements and thus improve the signal-to-noise ratio. To illustrate the importance of this, the absolute values of the fast Fourier transform (FFT) spectra of the sensor output signals for both sensor positions, $|S_r(r_1, \nu)|$ and $|S_r(r_2, \nu)|$, averaged out over 200

repeated measurements, and the absolute values of the FFT spectra of the noise in one measurement $|\Sigma_1(\nu)|$ and the noise averaged out over 200 repeated measurements $|\Sigma_{200}(\nu)|$, are shown in Fig. 4. The noise measurements were carried out under the same circumstances as the signal measurements except that, obviously, no stimulant force was introduced.

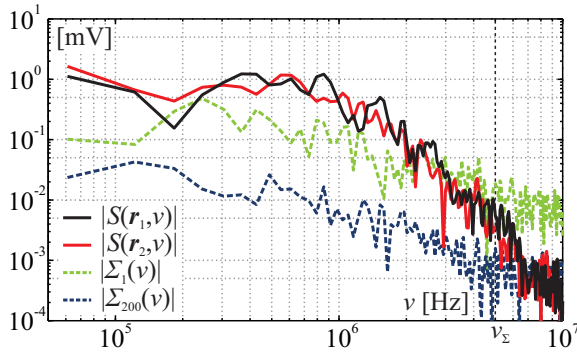


Fig. 4. A spectral comparison between the absolute values of the FFTs of the sensor output signal in both sensor positions and the sensor output noise averaged over 200 measurements and another measured only once

Comparing both noise spectra in Fig. 4, it is evident that averaging does, in fact, reduce the noise by about a decade throughout most of the frequency range. This seems consistent with signal processing theory which states that when averaging the signal over N repeated measurements, its stochastic noise could decrease by a factor of \sqrt{N} .

The figure also shows that the useful sensor response signal for both sensor positions is well above the averaged noise levels for frequencies smaller than about $\nu_\Sigma = 5$ MHz. At frequencies greater than ν_Σ , however, the signal decreases below the averaged sensor output noise and becomes unsuitable for further processing. Any sensor calibration measurement must therefore be regarded as inaccurate at frequencies above ν_Σ and cannot be used for credible sensor calibration at those frequencies.

It has to be noted here that much of the output noise is most likely due to the electronics of both amplifications stages of the sensor as they were not optimized for such high-frequency measurements. The signal-to-noise ratio could be improved even more with larger laser-pulse energies and with more numerous measurement repetitions.

The sensor output measurements and calculated input waveforms are presented in Figs. 5 and 6.

Fig. 5a shows a comparison of the two theoretically calculated sensor input waveform models in picometres: a PP model $u_{pp}(\mathbf{r}_1, t)$ calculated from

$g_{pp}(\tilde{\mathbf{r}}, \mathbf{r}_1, t)$ and an RR model $u_{RR}(\mathbf{r}_1, t)$ calculated from $g_{RR}(\tilde{\mathbf{r}}, \mathbf{r}_1, t)$, with the measured sensor output voltage $s(\mathbf{r}_1, t)$ in millivolts for the sensor in position 1. In addition, Fig. 5b shows a spectral comparison of the absolute values of their respective FFTs $|U_{PP}(\mathbf{r}_1, \nu)|$, $|U_{RR}(\mathbf{r}_1, \nu)|$ and $|S(\mathbf{r}_1, \nu)|$.

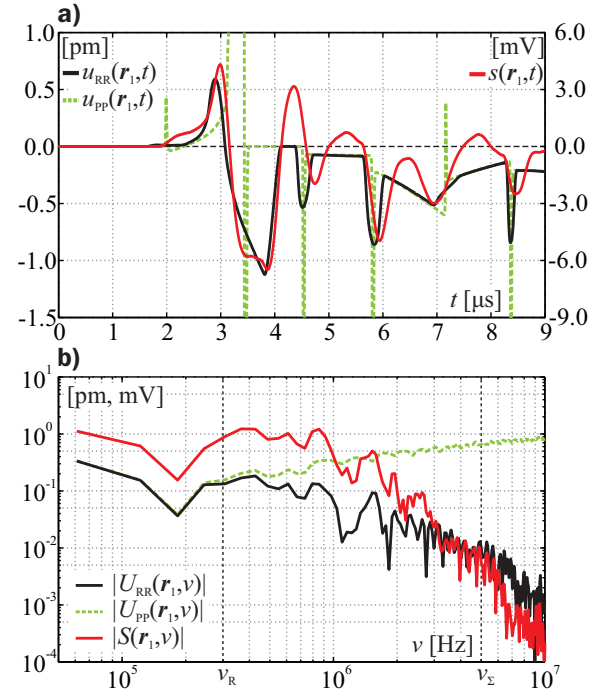


Fig. 5. a) A comparison of the two theoretically calculated sensor input waveform models and the sensor output voltage in sensor position 1 (same side as the source force) as well as b) a spectral comparison between the absolute values of their respective FFTs

Similarly, Fig. 6 shows all of these for the sensor in position 2.

The distinctive peaks and abrupt changes in slope in the waveforms in Figs. 5a and 6a indicate wave-arrivals.

The sensor transfer functions are calculated as described in section 1. The sensor input waveform models and the sensor output voltage measurements for both sensor positions are each fast Fourier transformed to obtain their spectra. The output measurement spectrum is then divided by the corresponding input waveform spectrum, as in Eq. (4), to obtain their sensor transfer function spectrum.

Before the input models and the output measurements are fast Fourier transformed, they are all multiplied by the appropriate tapered cosine (Tukey) window function [22] to avoid any spurious frequencies in the FFTs [12] due to the possible

3 DISCUSSION

artificial steps between the first and last points of the waveform models and the voltage measurements.

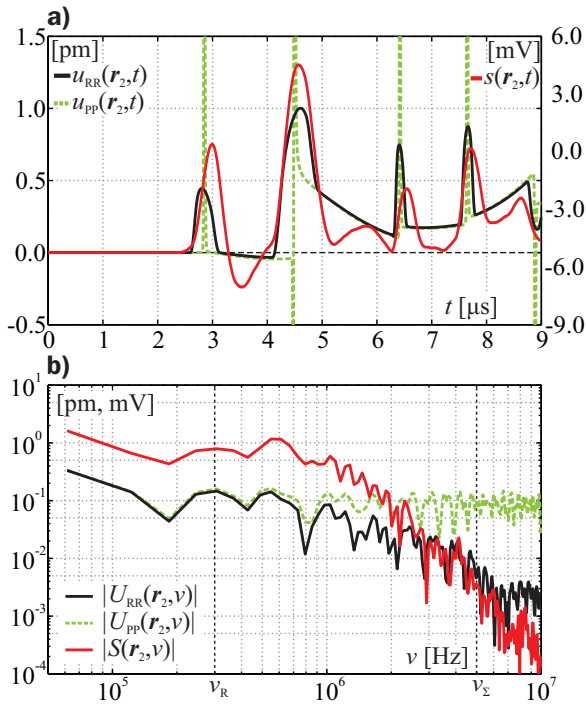


Fig. 6. a) A comparison of the two theoretically calculated sensor input waveform models and the sensor output voltage in sensor position 2 (opposite side as the source force) as well as b) a spectral comparison between the absolute values of their respective FFTs

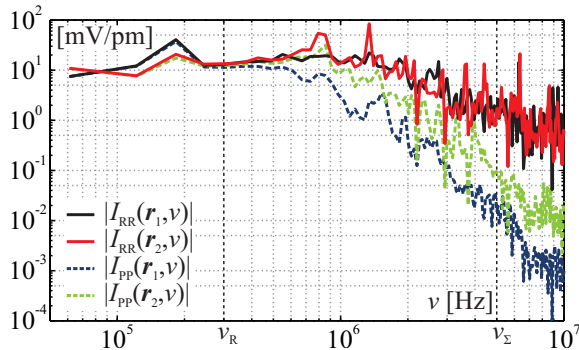


Fig. 7. A comparison of the absolute values of the calculated sensor transfer function spectra for real-source-real-sensor (RR) model and point-source-point-sensor (PP) model for both sensor positions

The absolute values of the sensor transfer function spectra for RR and PP models in both sensor positions are shown in Fig. 7 and are: $|I_{RR}(r_1, \nu)|$, $|I_{RR}(r_2, \nu)|$, $|I_{PP}(r_1, \nu)|$, $|I_{PP}(r_2, \nu)|$, respectively.

A comparison between the two theoretically calculated sensor input waveforms from the point-source-point-sensor and the real-source-real-sensor models and the sensor output voltage for both sensor positions shown in Figs. 5 and 6 shows notable differences.

Due to the unprecedented shortness of the ultrasound inducing laser pulse used here, the PP model waveform has very narrow spikes instead of the broader peaks that can be seen in the measured signals in Figs. 5a and 6a. It seems thus quite obvious that of the two models, the RR model produces a waveform that follows the contours of the measured signal much more closely than the hitherto used PP model. Most notably, although the measured sensor signal has a certain delay and a sort of ‘inertia’ compared to the RR model waveform, the duration and time distribution of the individual wave arrivals in the RR model correspond closely to the duration and time distribution of the wave arrivals in the PP model. Their respective FFT spectra show similar indications up to the sensor output noise levels at a frequency of about ν_Σ as well.

It is interesting to note that the PP model and RR model spectra for both sensor positions overlap at frequencies smaller than about $\nu_R = 300$ kHz and diverge greatly at frequencies greater than about ν_R . This indicates that the source force distribution effect and the sensor aperture effect do not show at frequencies smaller than ν_R while they are quite significant at frequencies greater than ν_R . The shortest waves at this frequency can be calculated to have wavelength of about $\lambda_R = 1.1$ cm, which is about an order of magnitude greater than the size of the source force impact area and the sensor contact area. For those area sizes, the PP model may apply for frequencies smaller than ν_R .

Furthermore, the calculated spectral sensor transfer functions in Fig. 7 also indicate the consistency of the RR model. The transfer functions of the RR model for both sensor positions seem to overlap reasonably, whereas the transfer functions of the PP model for each of the sensor positions do not. This can be further confirmed by calculating and comparing the absolute deviation D between both of the RR model transfer function spectra $D_{RR} = 0.344$ and both of the PP model transfer function spectra $D_{PP} = 0.761$. From this it is evident that the spectra of the RR model deviate much less from each other than those of the PP model. Should the spectra be made smooth, the distinction in deviation for the RR

model and the PP model would have been even more pronounced: $D_{RRsm} = 0.096$ and $D_{PPsm} = 0.788$.

It is also important to note that all of the corresponding sensor transfer functions start their divergence at a frequency of about ν_R thus indicating again that the source force distribution effect and the sensor aperture effect start to manifest themselves at frequencies greater than ν_R .

The theory shows that these distinctions can mostly be attributed to the incorporation of the sensor aperture effect and the source force distribution effect in the RR model and their exclusion from the PP model, as explained in detail further on. The schematics of the incorporation or exclusion of the source force distribution effect and the sensor aperture effect for different waveform models are illustrated in Fig. 8.

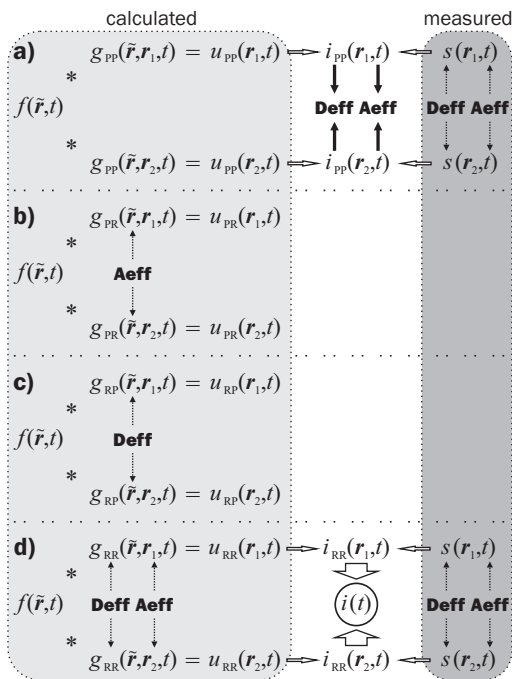


Fig. 8. Schematics of the mathematical incorporation of the source force distribution effect (Deff) and the sensor aperture effect (Aeff) for a) point-source-point-sensor (PP), b) point-source-real-sensor (PR), c) real-source-point-sensor (RP), and d) real-source-real-sensor (RR) models for both sensor positions as used and discussed here

It is worth noting that the aperture effect and the source force distribution effect are location specific, meaning that they are different at different relative positions of the source force area and the sensor contact area to each other.

Since the sensor outputs are responses to real waveform stimulations, these effects are always

intrinsically incorporated into the measured sensor output signals $s(\mathbf{r}_1, t)$ and $s(\mathbf{r}_2, t)$. In the theoretically calculated models, however, this is not necessarily the case.

As Fig. 8a illustrates, the PP model does not incorporate any force distribution and sensor aperture effects while the sensor output signals naturally do. Therefore, when the sensor transfer functions for both sensor positions, $|I_{PP}(\mathbf{r}_1, \nu)|$ and $|I_{PP}(\mathbf{r}_2, \nu)|$, are derived from such a model, each still contains the source force and sensor aperture effects. Since these effects are specific for each sensor position, these transfer functions are position specific as well. This is the single most important reason for the mismatch of the PP sensor transfer functions in Fig. 7 at frequencies greater than ν_R .

Conversely, as Fig. 8d illustrates, the RR model does incorporate the source force distribution effect and the sensor aperture effect. These effects are incorporated in the plate transfer functions $g_{RR}(\tilde{\mathbf{r}}, \mathbf{r}_1, t)$ and $g_{RR}(\tilde{\mathbf{r}}, \mathbf{r}_2, t)$, and subsequently in the sensor input waveform models $u_{RR}(\mathbf{r}_1, t)$ and $u_{RR}(\mathbf{r}_2, t)$. So, when the sensor transfer functions for both sensor positions, $|I_{RR}(\mathbf{r}_1, \nu)|$ and $|I_{RR}(\mathbf{r}_2, \nu)|$, are derived from this model they contain no such effects as the effects naturally incorporated into the measured sensor output signals are, in a way, sufficiently cancelled out by the same effects mathematically incorporated in the calculated sensor input waveforms at each sensor position. In this manner, the aperture effect and the source force distribution effect are properly accounted for in the RR model and thus eliminated from its sensor transfer functions. This is why, in Fig. 7, the RR transfer functions match quite well, even at frequencies greater than ν_R , and a single, position independent sensor transfer function $|I(\nu)|$ can be obtained from them. It should be stressed that obtaining the proper, position independent sensor transfer function was the goal of this sensor calibration in the first place.

There exist two intermediate models between the two shown above. As Figs. 8b and 8c illustrate, the PR model and the RP model contain only the sensor aperture effect and the source force distribution effect, respectively. No sensor transfer functions are derived from them as they are only meant for the study of those effects further in the discussion.

If the use of the PP model in sensor calibration at higher frequencies were unavoidable, the best advice would be to calibrate the sensor in the position of its intended use, as the non-overlapping of the PP model sensor transfer functions clearly indicates their non-universality.

All of this demonstrates the superiority of the RR model over the older PP model for high-frequency sensor calibration where the source force area and the sensor contact area are larger than the waveform wavelengths and the source force distribution effect and the sensor aperture effect become considerable.

The waveforms are in fact superpositions of many different kinds of waves each with different characteristics and each propagating with different velocities. For a quick estimate of the order of magnitude of their wavelengths, one can use the basic phase velocity equation: $\lambda=c/v$. The shortest and slowest reliably measured waves, at the noise limit frequencies of about ν_{Σ} , have wavelengths of about $\lambda_{\min}=0.7$ mm while the longest and fastest measured waves have wavelengths of several centimeters. It is difficult to measure these longer waves reliably as their arrivals span much of the measured time and only a few wavelengths are measured at best. Larger specimens would allow for longer measuring times and calibration at lower frequencies. The shortest measured waves are therefore much smaller than the sensor contact area and the longest are much longer than the source force impact area.

The presence of the sensor aperture effect can be clearly demonstrated using the point-source-real-sensor model. A spectral comparison of the absolute values of the FFTs of the sensor input waveforms of the PP and PR models for both sensor positions is shown in Fig. 9a. It is worth highlighting the PR model for position 1 as it has distinctive lobes at certain frequencies. The minima between the lobes (some indicated by arrows in Fig. 9a) can be found to occur at frequencies close to:

$$\nu_{Sn} = n \frac{c_R}{2r_{S0}}, \quad (5)$$

where n is a positive integer and c_R is the propagation velocity of the Rayleigh waves, which are estimated to have dominant amplitudes on the top surface of the plate. It can thus be calculated: $\nu_{S1} = 3.4$ MHz, $\nu_{S2} = 6.8$ MHz, $\nu_{S3} = 10.1$ MHz, $\nu_{S6} = 20.3$ MHz, and so on. The reason for their slight shift towards higher frequencies in the measurements is probably due to the presence of other waves. This lobe phenomenon is due to the fact that surface waves propagate in the direction parallel to the sensor contact area. So, whenever the waveform wavelength is a multiple of the width of the sensor contact area, its signal decreases significantly as it is averaged out by the sensor. In position 2, the lobes are not visible in the spectrum, because the waves are incident at more acute angles.

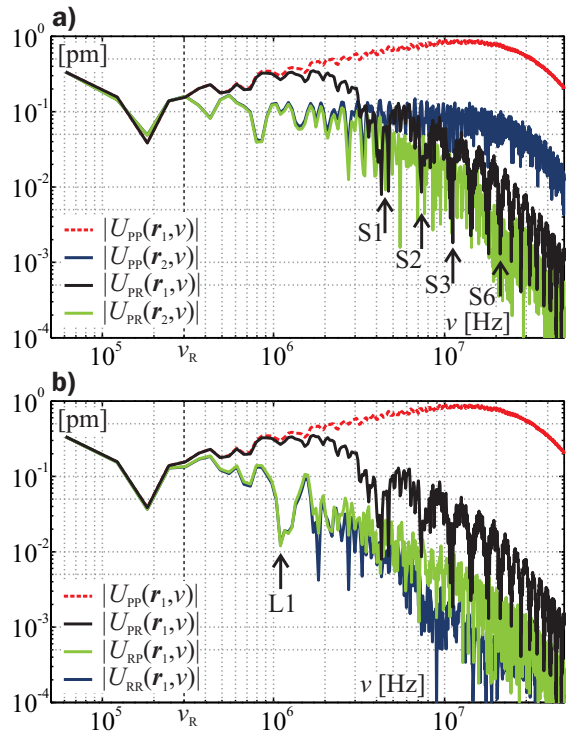


Fig. 9. A spectral comparison of the absolute values of the FFTs of the calculated sensor input waveforms a) for point-source-point-sensor (PP) and point-source-real-sensor (PR) models for both sensor positions and b) for point-source-point-sensor (PP), point-source-real-sensor (PR), real-source-point-sensor (RP) and real-source-real-sensor (RR) models for sensor in position 1

The significance of the source force distribution effect can be demonstrated with the real-source-point-sensor model. A spectral comparison of the absolute values of the FFTs of the sensor input waveforms of all models for sensor in position 1 is shown in Fig. 9b. A pronounced minimum (indicated by an arrow in Fig. 9b), not present in the PP and PR models, is observed at a frequency of about 1 MHz. It can be explained as a manifestation of the source force distribution effect. Substituting r_{S0} in Eq. (5) with the r_{L0} , one gets $\nu_{L1} = 0.97$ MHz. Here, the surface waves at this frequency are mostly canceled out by the geometry of the source force distribution relative to the sensor point position.

From Fig. 9b it can be observed that, while overlapping the lowest frequencies, the PP and the PR model spectra start diverging from the RP and the RR model spectra at a frequency of about ν_R . Furthermore, it can be observed that the former two continue to overlap until a frequency of about 1.0 MHz while the latter two continue to overlap almost up to a frequency of 2.0 MHz. Even at higher frequencies, the RP model spectrum is much closer to the RR model spectrum

than the other two and they have more similar contours as well.

In addition, it can also be observed that the one distinct lobe from the source force distribution effect is clearly present in the RR model spectrum, while none of the sensor aperture effect lobes are distinctly present in that spectrum. The sensor aperture effect is thus practically drowned out by the source force distribution effect in the RR model spectrum.

From this it can be concluded that the source force distribution effect has far greater presence in the RR model than the sensor aperture effect. This is mainly due to the fact that the source force impact area is significantly larger than the sensor contact area.

4 CONCLUSIONS

An absolute high-frequency calibration of a conical piezoelectric displacement sensor was presented here. The method uses a significantly improved theoretically calculated sensor input waveform model that incorporates the real dimensions of the source force area and the sensor contact area. In this manner, the real-source-real-sensor model enables the calculation of the proper sensor transfer function, which is devoid of the sensor aperture effect and the source force distribution effect and is therefore universal for any sensor position.

Experimentally, a Glaser-type piezoelectric displacement sensor has been calibrated on a glass plate with a high-reflectivity coating using a very short laser pulse reflection as the source force.

It was demonstrated that the critical role of incorporating the real dimensions of the source force area and the sensor contact area cannot be overlooked in the case of high-frequency ultrasound sensor calibration.

5 ACKNOWLEDGEMENTS

The research was conducted as a part of the Optodynamics programme (P2-0392), in duration from 2015-1-1 to 2019-12-31, financed by the Slovenian Research Agency.

6 REFERENCES

- [1] Požar, T., Možina, J. (2014). Detection of subnanometer ultrasonic displacements. Sattler, K.D. (Ed.). *Fundamentals of Picoscience*. CRC Press, Boca Raton [etc.], p. 553-577.
- [2] Fortunko, C.M., Boltz, E.S. (1996). Comparison of absolute sensitivity limits of various ultrasonic and vibration transducers. *Materials Science Forum*, vol. 210-213, p. 471-478, DOI:10.4028/www.scientific.net/MSF.210-213.471.
- [3] Grosse, C.U., Ohtsu, M. (Eds.). (2008). *Acoustic Emission Testing: Basics for Research, Applications in Civil Engineering*. Springer, Berlin. DOI:10.1007/978-3-540-69972-9.
- [4] Sikorski, W. (Ed). (2012). Acoustic emission. *InTech*. DOI:10.5772/2070.
- [5] Moore, P.O., Miller, R.K., Hill, E.v.K. (Eds.). (2005). *Nondestructive Testing Handbook, 3rd ed. Vol. 6, Acoustic Emission Testing*. American Society for Nondestructive Testing, Columbus.
- [6] McLaskey, G.C., Thomas, A.M., Glaser, S.D., Nadeau, R.M. (2012). Fault healing promotes high-frequency earthquakes. *Nature*, vol. 491, no. 7422, p. 101-104. DOI:10.1038/nature11512.
- [7] Goodfellow, S.D., Young, R.P. (2014). A laboratory acoustic emission experiment under in situ conditions. *Geophysical Research Letters*, vol. 41, no. 10, p. 3422-3430. DOI:10.1002/2014GL059965.
- [8] Royer, D., Dieulesaint, E. (2000). *Elastic Waves in Solids II: Generation, Acousto-optic Interaction, Applications*. Springer-Verlag, Berlin [etc.], DOI:10.1007/978-3-662-06938-7.
- [9] Požar, T., Babnik, A., Možina, J. (2015). From laser ultrasonics to optical manipulation. *Optics express*, vol. 23, no. 6, p. 7978-7990, DOI:10.1364/OE.23.007978.
- [10] Požar, T., Možina, J. (2013). Measurement of elastic waves induced by the reflection of light. *Physical Review Letters*, vol. 111, no. 18, 185501, DOI:10.1103/PhysRevLett.111.185501.
- [11] Možina, J., Diaci, J. (2011). Recent advances in optodynamics. *Applied Physics B: Lasers and Optics*, vol. 105, no. 3, p. 557-563, DOI:10.1007/s00340-011-4503-6.
- [12] ASTM Standard E1106-86(2002)e1. *Standard Method for Primary Calibration of Acoustic Emission Sensors*. ASTM International, West Conshohocken.
- [13] McLaskey, G.C., Glaser, S.D. (2012). Acoustic Emission Sensor Calibration for Absolute Source Measurements. *Journal of Nondestructive Evaluation*, vol. 31, no. 2, p. 157-168. DOI:10.1007/s10921-012-0131-2.
- [14] McLaskey, G.C., Glaser, S.D. (2010). Hertzian impact: Experimental study of the force pulse and resulting stress waves. *Journal of the Acoustical Society of America*, vol. 123, no. 3, p. 1087-1096, DOI:10.1121/1.3466847.
- [15] Cho, S.I., Lee, J.K., Lee, J.O., Jung, S.S., Lee, D.H., Seo, W.C. (2008). PZT Transducer Response to an Epicentral Acoustic Emission Signal During Glass Capillary Breakage. *Journal of the Korean Physical Society*, vol. 53, no. 6, p. 3213-3219. DOI:10.3938/jkps.53.3213.
- [16] Goldsmith, W. (2001). *Impact: The Theory and Physical Behaviour of Colliding Solids*. Dover Publications, Mineola.
- [17] Bosiger, G., Perhavec, T., Diaci, J. (2014). A Method for Optodynamic Characterization of Erbium Laser Ablation Using Piezoelectric Detection. *Strojniški vestnik - Journal of Mechanical Engineering*, vol. 60, no. 3, p. 172-178, DOI:10.5545/sv-jme.2013.1077.
- [18] Hsu, N.N. (1985). *Dynamic Green's functions of an infinite plate - a computer program*. Technical Report No. NBSIR 85-3234, National Bureau of Standards, Washington.

- [19] KRN Services, Inc. (2015). Sensors, from: <http://www.krnservices.com/sensors>, accessed on 2015-06-01.
- [20] Schneider, M., Berthe, L., Fabbro, R., Muller, M. (2008). Measurement of laser absorptivity for operating parameters characteristic of laser drilling regime. *Journal of Physics D: Applied Physics*, vol. 41, no. 15, 155502. DOI:10.1088/0022-3727/41/15/155502.
- [21] Weaver, J.H., Frederikse, H.P.R. (2009). Optical properties of selected elements. Lide, D.R. (Ed.), *CRC Handbook of Chemistry and Physics*, 89th ed. CRC Press, Boca Raton [etc.], p. 12-123-12-147.
- [22] Bloomfield, P. (2000). *Fourier Analysis of Time Series: An Introduction*, 2nd edition. John Wiley & Sons, New York, DOI:10.1002/0471722235.

Linear and Neural Network-based Models for Short-Term Heat Load Forecasting

Primož Potočnik* – Ervin Strmčnik – Edvard Govekar

University of Ljubljana, Faculty of Mechanical Engineering, Slovenia

Successful operation of a district heating system requires optimal scheduling of heating resources to satisfy heating demands. The optimal operation, therefore, requires accurate short-term forecasts of future heat load. In this paper, short-term forecasting of heat load in a district heating system of Ljubljana is presented. Heat load data and weather-related influential variables for five subsequent winter seasons of district heating operation are applied in this study. Various linear models and nonlinear neural network-based forecasting models are developed to forecast the future daily heat load with the forecasting horizon one day ahead. The models are evaluated based on generalization error, obtained on an independent test data set. Results demonstrate the importance of outdoor temperature as the most important influential variable. Other influential inputs include solar radiation and extracted features denoting population activities (such as day of the week). Comparison of forecasting models reveals good forecasting performance of a linear stepwise regression model (SR) that utilizes only a subset of the most relevant input variables. The operation of the SR model was improved by using neural network (NN) models, and also NN models with a direct linear link (NNLL). The latter showed the overall best forecasting performance, which suggests that NN or the proposed NNLL structures should be considered as forecasting solutions for applied forecasting in district heating markets.

Keywords: district heating, heat load forecasting, feature extraction, stepwise regression, autoregressive model, neural networks

Highlights

- Development of models for short-term heat load forecasting.
- Selection of relevant inputs for the best forecasting performance.
- Introduction of a neural network-based model with a direct linear link.
- Comparison of linear and neural network based models based on generalization performance.
- The best forecasting result is obtained with a neural network model with a direct linear link.

0 INTRODUCTION

Energy efficiency is specified by the European Union (EU) as a key driver of the transition toward a low-carbon society [1]; recent studies show that new district heating systems can reduce heating and cooling costs by 15 %, which represents €100 billion per year [2]. The successful operation of a district heating system requires optimal scheduling of heating resources to satisfy the heating demands. The scheduling operation requires accurate short-term forecasts of future heat load to optimally assign heating resources. Energy demand forecasting systems may also be helpful in supporting future environmentally friendly urban planning [3]. Short-term energy demand forecasting has been studied predominantly in the field of electricity load forecasting and natural gas consumption forecasting [4], and less so in district heating forecasting, although similar statistical models can be applied [5]. The sources of heat load variations in district heating systems are both seasonal and daily and are mainly a consequence of variations in outdoor temperature and the social behaviour of customers [6].

Various forecasting approaches have been applied to analyse and support the operation of district heating

systems, including a simple forecasting model [7], a grey-box forecasting approach [8], a lifting scheme combined with ARIMA models [9], and functional clustering combined with linear regression [10]. An efficient forecasting approach to energy demand forecasting based on semiparametric regression smoothing was proposed by [5]. Other approaches include a general fixed district heating model structure that can be adapted for any particular district heating system and used in cost-optimization studies [11], a forecasting method for space heating in a single-family houses [12], and nonparametric regression model [13]. Whereas linear ARX models have been successfully applied in load-forecasting applications [14], nonlinear ARX models based on neural networks have also been proposed [15].

In this paper, short-term forecasting solutions for a district heating network are investigated, and several models are proposed and compared for one day ahead forecasting of heat load. The study is based on heat load data for the district heating network of Ljubljana, which is the largest district heating network in Slovenia. Various weather related parameters are collected and included in the forecasting models, and models are constructed and tested through cross-

validation procedures to verify the generalization performance on independent data.

The paper is structured as follows. Section 1 presents the case study data applied in this paper, including the heat load data, weather-related parameters, and additional extracted features. Sections 2 and 3 present the formulation of the forecasting problem and description of various linear and neural network-based forecasting models. The results are presented in Section 4 and conclusions are summarized in Section 5.

1 DATA

This study is based on district heating data from September 2008 to February 2013, obtained from the company Energetika Ljubljana, d.o.o. The data comprise daily heat load Q , and various measurement weather data (outdoor temperature T , solar radiation S , wind speed W , relative humidity H). Q data represent the heat transfer entering the district heating system.

Fig. 1 presents the complete Q data in daily resolution with winter and summer seasons marked.

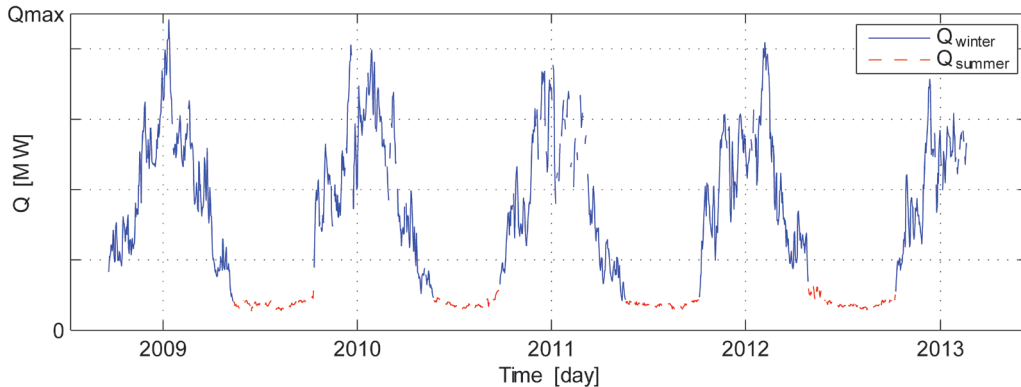


Fig. 1. Heat load data Q from September 2008 until February 2013 in daily resolution

Linear dependence $Q(T)$ between the heat load Q and outdoor temperature T on a daily scale is presented in Fig. 2. In this study, only winter data, which are more difficult to estimate due to strong weather-related influences, are analysed. The transient period between the and summer seasons is not discussed in this paper although it also presents a challenging forecasting problem.

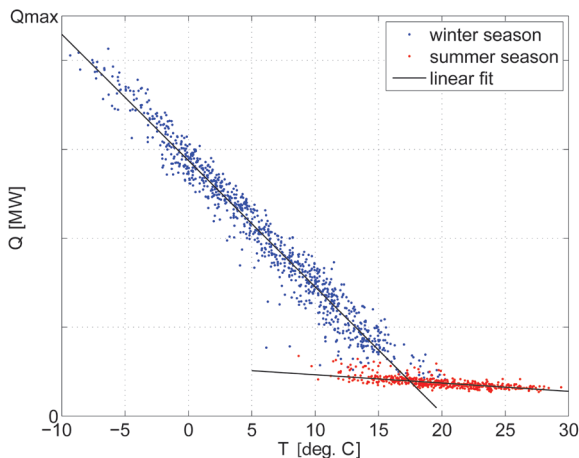


Fig. 2. Relation between heat load Q and outdoor temperature T (on daily scale) with linear fits for winter and summer seasons

1.1 Feature Extraction

Beside the original heat (Q) and weather-related time series data (T , S , W , H), additional features were extracted in order to facilitate the construction of efficient forecasting models:

- t_d linear time expressed in days since the beginning of the data,
- t_{\cos} seasonal cycle, expressed by $\cos(2\pi t_d/365)$,
- d_{work} dummy variable expressing workday,
- d_{Sat} dummy variable expressing Saturday,
- d_{Sun} dummy variable expressing Sunday or holiday.

Dummy variables denoting various days of the week are primarily related to the behavior of end users that is considerably different during the week and the weekend. Linear time and seasonal cycle features take into consideration linear trends in heat consumption and basic seasonal cycles.

2 FORECASTING APPROACH

Various forecasting model structures are explored with the aim of developing an efficient and robust forecasting model for the forecasting of heat load Q

one day in advance. At the time t expressed in the daily resolution, our aim is to forecast future heat load $Q(t+h)$ with the forecasting horizon $h = 1$ day. Longer forecasting horizons are currently not relevant because heat load forecasting is required only for short-term optimization of heating resources.

Due to a highly linear relation between the daily heat load Q and the outdoor temperature T (shown in Fig. 2), we expect linear forecasting models to sufficiently describe the heat consumption phenomena, but we also apply neural network-based nonlinear forecasting models to explore the eventual nonlinear heat demand response. Applied forecasting models are described in Section 3.

For the evaluation of forecasting models, we introduce the so-called mean absolute range normalized error (MARNE), which is a relative measure depending on the size of the district heating system and can easily be interpreted in technical or economical terms. The MARNE error is calculated as the average of the absolute differences of the forecast Q_f heat consumption and the actual heat consumption Q_a , normalized by the maximum transmission capacity of the district heating network Q_{max} :

$$MARNE = 100 \frac{\frac{1}{N_d} \sum_{t=1}^{N_d} |Q_f(t) - Q_a(t)|}{Q_{max}} [\%], \quad (1)$$

$t = 1, 2, \dots, N_d,$

where N_d is the number of days of the heat load time series, which in our case study amounts to $N_d = 1614$.

Currently, there are no direct links to estimate savings based on forecasting results. Heat load forecasts are required for short-term optimization of heating resources within the company, which may include decisions about switching particular heaters on/off at the right time and considering secondary energents if necessary. Actual savings are, therefore, very difficult to estimate and are also subject to the confidential policy of the company. Consequently, the optimality of the proposed forecasting approach can be currently estimated only through the forecasting accuracy measures, such as the MARNE measure proposed in this paper.

The generalization performance of forecasting models was evaluated based on cross-validation principle. Available data (as shown in Fig. 1) were split into training and testing subsets, containing 60 % and 40 % of data, respectively, which corresponds to the first three winter seasons of training data and the remaining two winter seasons of testing data. The forecasting errors in both data sets were denoted as $MARNE_{train}$ and $MARNE_{test}$, and the final criterion

for evaluation of model performance was testing error $MARNE_{test}$, which presents an independent measure of model accuracy and its generalization ability to perform well on novel data.

3 FORECASTING MODELS

Various model structures were examined in this study to find a suitable forecasting model for short-term heat load forecasting. The modelling approaches can be summarized into three groups as follows:

- Benchmark models
 - random walk model,
 - temperature correlation model.
- Linear models
 - regression model,
 - autoregressive models,
 - stepwise regression.
- Nonlinear neural network models
 - feedforward neural network,
 - feedforward neural network with a direct linear link.

The following paragraphs describe the structures of examined forecasting models, and the list of regressors included in each model is summarized in Table 1.

3.1 Random Walk Model

The random walk (RW) model predictor $Q(t+1)$ derives its value from past heat load $Q(t)$, with $e(t)$ denoting noise and t the arbitrary time in daily resolution:

$$Q(t+1) = Q(t) + e(t+1). \quad (2)$$

The random walk model is only considered as a basis to evaluate the other, more elaborate models, as recommended in [16] where RW model is implicitly included in the proposed mean absolute scaled error measure.

3.2 Temperature Correlation Model

The temperature correlation model (TC) correlates the heat load $Q(t+1)$ with the average daily temperature $T(t+1)$:

$$Q(t+1) = b_0 + b_1 T(t+1) + e(t+1). \quad (3)$$

The motivation for this model is the strong negative correlation between daily outdoor temperature and heat load, as described in Section 1.

3.3 Regression Model

The linear regression model (REG) expands the selection of a single temperature input of a TC model in Eq. (3) by including also delayed temperature values $T(t)$, $T(t-1)$, ..., and also informative features as described in Section 1.1. The list of included regressors is shown in Table 1.

3.4 Autoregressive Models

Autoregressive models (ARX) further expand the REG model by including as inputs as well as delayed heat load values $Q(t)$, $Q(t-1)$, Various applied ARX models differ only in the selection of additional weather-related inputs (see Table 1 for details).

The ARIX model has the same structure as the ARX model but forecasts the differences in daily heat load ΔQ instead of forecasting the absolute heat load Q .

3.5 Stepwise Regression Model

The stepwise regression model (SR) in this study is based on the initial selection of regressors provided by ARX models and is constructed by iteratively adding and removing regressors based on their statistical significance in a regression [17]. The method

begins with an initial model and then compares the explanatory power of incrementally larger and smaller models. At each step, the p -value of an F -statistic is computed in order to test models both with and without a potential input. Tested inputs are iteratively added or removed from the model until the procedure converges to a locally optimal forecasting model with statistically significant input variables. This method also resolves the collinearity problem by reducing the available set of inputs to the relevant ones.

3.6 Feedforward Neural Network

Feedforward neural network (NN) models [18] can be considered to be nonlinear auto-regressive models (NARX) that extend the ARX models with the ability to also encapsulate nonlinear system responses. In our study, a feedforward neural network with sigmoidal activation functions was applied, and the number of hidden neurons was kept low to prevent overfitting. For the same reason, the Levenberg-Marquardt learning algorithm with Bayesian regularization was applied to improve generalization.

The architecture of the NN with one hidden layer of neurons with sigmoidal activation function and a linear output layer is shown in Fig. 3. Based on the initial simulation results, the hidden layer consists of 5 hidden neurons. Increasing the number of hidden

Table 1. Summary of forecasting models and included regressors

Linear models	RW	TC	REG	ARX1	ARX2	ARX3	ARX4	SR	ARIX
Neural net models					NN2 NNLL2		NN4 NNLL4	NNSR NNLLSR	
Forecast:	$Q(t+1)$	$Q(t+1)$	$Q(t+1)$	$Q(t+1)$	$Q(t+1)$	$Q(t+1)$	$Q(t+1)$	$Q(t+1)$	$\Delta Q(t+1)$
Extracted features			t_d						
			t_{\cos}						
			d_{work}						
			d_{Sat}						
			d_{Sun}						
Outdoor temperature T		$T(t+1)$	$T(t+1)$	$T(t+1)$	$T(t+1)$	$T(t+1)$	$T(t+1)$	$T(t+1)$	$T(t+1)$
			$T(t)$						
			$T(t-1)$						
			$T(t-2)$						
			$T(t-3)$						
Regressors:		$Q(t)$		$Q(t)$	$Q(t)$	$Q(t)$	$Q(t)$	$Q(t)$	$Q(t)$
				$Q(t-1)$	$Q(t-1)$	$Q(t-1)$	$Q(t-1)$		
				$Q(t-2)$	$Q(t-2)$	$Q(t-2)$	$Q(t-2)$		
				$Q(t-3)$	$Q(t-3)$	$Q(t-3)$	$Q(t-3)$	$Q(t-3)$	$Q(t-3)$
Solar radiation S				$S(t+1)$	$S(t+1)$	$S(t+1)$	$S(t+1)$	$S(t+1)$	
Wind speed W				$S(t)$	$S(t)$	$S(t)$			
Relative humidity H							$W(t+1)$	$W(t+1)$	
								$H(t+1)$	

neurons did not improve the generalization ability of the model.

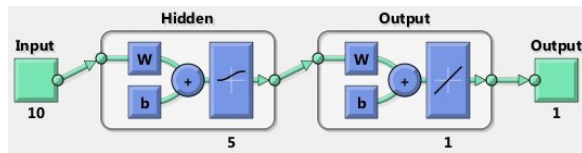


Fig. 3. Feedforward neural net (NN)

3.7 Feedforward NN with Direct Linear Link

In addition to the classic neural network architecture described above, an additional NN architecture with a direct linear link (NNLL) was applied due to the strong linear relationship between the input and output variables. The advantage of the NNLL architecture is its improved ability to directly model linear mappings with the additional capacity to add nonlinear responses. The NNLL architecture is presented in Fig. 4 where a direct linear link from the inputs to the output layer is shown. In this configuration, the hidden layer can be considered as a nonlinear feature extractor that provides additional features to the linear regression model implemented by a linear output layer. In our case study, only 2 nonlinear hidden layer neurons were used to prevent unnecessary overfitting.

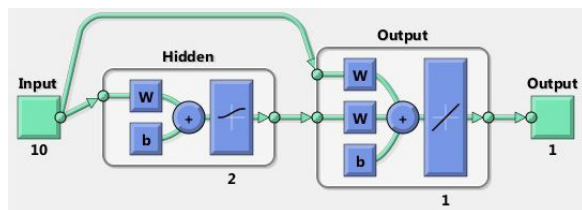


Fig. 4. Feedforward neural net with direct linear link (NNLL)

The training procedure for all neural network models (NN and NNLL) included 200 repeated random initializations followed by gradient-based learning (until learning converged). The results reported include the average and the best result obtained from 200 training realizations.

4 RESULTS

This section presents forecasting results obtained by applying the described forecasting models (Section 3) to the forecasting problem defined in Section 2. For all applied models both training and testing errors (MARNE) are presented, although only the testing error that is considered an estimator of the generalization ability of the model is evaluated as a

final model performance measure. Forecasting results for all models are summarized in Table 2.

It should be noted that applied linear models always converge to a unique solution, whereas nonlinear NN models converge only to locally optimal solutions depending on the initial conditions of free network parameters (synaptic weights of neurons) that form the basis for the subsequent gradient-based optimization. Consequently, the average results for multiple NN initializations are reported in Table 2 as well as the best obtained NN results. The best obtained testing results for linear and neural models are marked in gray.

Table 2. Forecasting results

Model	Training MARNE [%]	Testing MARNE [%]	
Benchmark models			
RW	3.05	3.23	
TC	2.35	3.43	
Linear models			
REG	1.51	2.62	
ARX1	1.14	1.33	
ARX2	1.06	1.33	
ARX3	1.04	1.35	
ARX4	1.03	1.35	
SR	1.08	1.24	
ARIX	1.36	1.51	
Neural network models			
		Mean	Best
NN2	0.76	1.83	1.21
NN4	0.73	1.75	1.24
NNSR	0.80	1.55	1.19
Neural network models with linear link			
NNLL2	1.08	1.40	1.23
NNLL4	1.06	1.39	1.21
NNLLSR	1.09	1.26	1.15

Both benchmark models (Table 2) yield initial generalization performance above 3 %: 3.23 % for the RW model and 3.43 % for the TC model. Although the training performance of TC model is better compared to RW model, its generalization performance is worse.

A comparison of linear models reveals that the regression model (REG) considerably improves the initial performance of both benchmark models by reducing the training error to 1.51 % and the testing error to 2.62 %. This confirms the benefits of including the proposed extracted features and delayed terms of outdoor temperatures.

The performance of the REG model is further improved by the family of autoregressive models (ARX) that include the delayed terms of past

heat consumption as inputs. The results clearly demonstrate the importance of the autoregressive forecasting approach. ARX models that differ only in the inclusion of additional weather related inputs (S , W , H) show similar performance; therefore, it can be concluded that additional weather-related inputs only marginally contribute to forecasting performance.

Additional generalization improvement was obtained by applying the stepwise regression approach that reduces the available inputs to strictly relevant ones. In the case of a SR model, a training error of 1.08 % was obtained, and a testing error of 1.24 % which is the best result in the family of linear models. Beside the improved generalization ability, the SR model also reduces the model complexity and is therefore considered as an appropriate model for application in the district heating industry.

The application of the ARIX model that includes the integrating term and, therefore, forecasts the heat consumption difference ΔQ (instead of Q) did not improve the results.

The forecasting results obtained by NN-based models show the following various interesting conclusions:

- NN training depends on the initial (random) initialization of network parameters (weights) therefore multiple learning initializations followed by supervised gradient-based learning are required to ensure good NN performance.
- Only a few hidden layer neurons are sufficient to model this type of an energy consumption process.
- The best NN results generally achieve and exceed the same level as the best linear model, but the improvement is slight due to a very linear dependence $Q(T)$.

- Due to the same reason of linear $Q(T)$ dependence, NN with a direct linear link (NNLL) seems to be a good forecasting model, as demonstrated by testing results. The best NNLLSR model based on inputs selected by an SR model achieves testing performance of 1.15 % which is the overall best generalization result. In this case, only two hidden layer neurons with sigmoidal activation functions were used. These two neurons can be considered as additional automatic nonlinear feature extractors that are added to the linear model.

The best testing (generalization) results of applied models are compared in Fig. 5. It can be seen that NN based models slightly improve the performance of linear models. The best linear model (SR) yields a testing performance of 1.24 %, and the best NN-based model (NNLLSR) yields 1.15 % which represents a 7.3 % improvement in testing performance in comparison to the SR model.

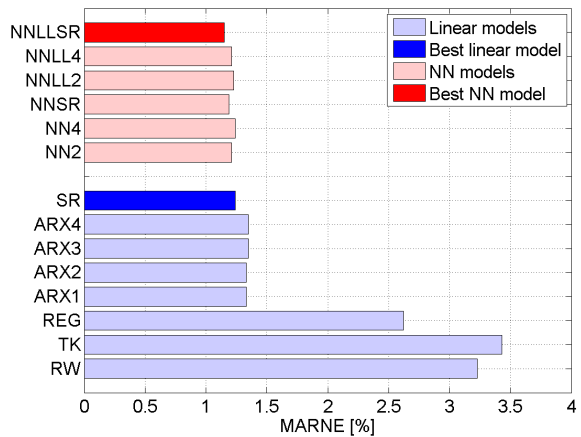


Fig. 5. Testing results of linear and NN-based forecasting models

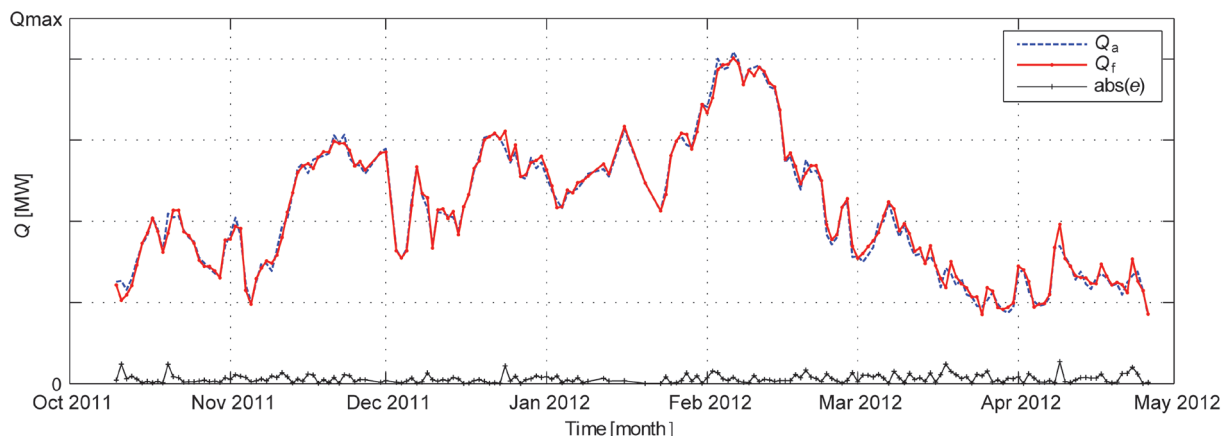


Fig. 6. Actual (Q_a) and forecasted (Q_f) heat consumption by a NNLLSR model

A graph of the forecasting results obtained by the best NNLSR model is presented in Fig. 6. Actual heat consumption Q_a , forecast heat consumption Q_f , and absolute forecasting error $e = \text{abs}(Q_a - Q_f)$ are shown for the selected test period from October 2011 to May 2012. The scatter plot of forecasting results (Q_f vs. Q_a) is shown in Fig. 7, where a very close matching can be observed (correlation coefficient $R = 0.996$).

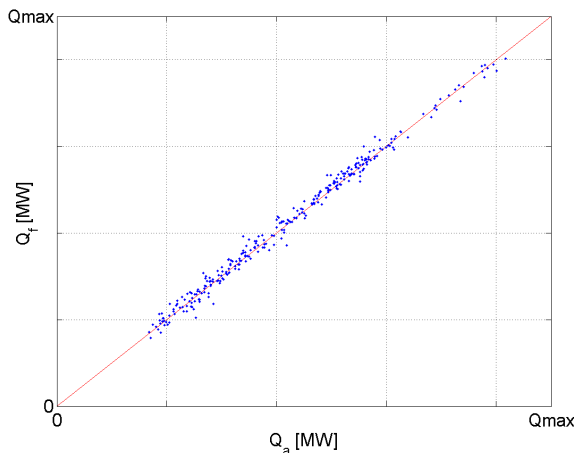


Fig. 7. Scatter plot of all testing forecasting results (Q_f vs. Q_a)

5 CONCLUSIONS

A study of forecasting models for heat demand a day in advance in a district heating system is discussed in this paper. The study is based on district heating data for the city of Ljubljana, Slovenia, for five subsequent winter seasons. Additional weather related variables (temperature, solar radiation, wind speed, relative humidity) and extracted features (days of the week, linear trend, seasonal cycle) were applied in our forecasting approach. Various forecasting models, including simple benchmark models, linear regression and autoregressive models, and nonlinear neural network-based models were constructed for the forecasting task. The forecasting performance of the models was evaluated based on the generalization performance obtained by cross-validation on a test data set. The conclusions of this study can be summarized as follows:

- There is a strong linear relationship between the heat consumption Q and the outdoor temperature T . Consequently, the most significant regressor for the future heat load $Q(t+1)$ forecasting is the outdoor temperature $T(t+1)$.
- Other weather-related parameters are less important with the exception of solar radiation

S , which has been included as a significant regressor via a stepwise regression model. This is consistent with the results in the field of natural gas forecasting [19]. Wind speed and relative humidity do not have a significant impact on heat consumption.

- Heat consumption also exhibits autoregressive behaviour; therefore, including the past heat consumption $\{Q(t-k), k=0, 1, \dots\}$ into forecasting models considerably improves the forecasting accuracy.
- Due to a strong population influence on heat consumption, including additional extracted features denoting days of the week, linear trend and seasonal cycle, also significantly improves the forecasting accuracy.
- The best linear model for this forecasting task is the stepwise regression model (SR) that includes only significant regressors. This reduces the model complexity and also improves the generalization ability. Testing performance (expressed as a MARNE error) 1.24 % was obtained for the SR model.
- Comparison of linear and nonlinear forecasting models reveals that slight improvement is possible by applying properly trained nonlinear NN-based models. In the case of NN models, multiple weight initializations should be applied in order to converge network training toward solutions emphasizing good generalization ability.
- The proposed NNLL architecture that combines NN with direct linear link results in a simple architecture that improves the linear model (represented by a direct linear link) with a nonlinear feature extractor (hidden nonlinear neurons). The NNLSR model with only two hidden neurons resulted in the best generalization result, expressed as a MARNE error of 1.15 %.

We can conclude that the proposed linear SR model is a suitable and robust candidate for industrial forecasting implementation. The advantage of the SR model is its low complexity, simple and transparent structure, and predictable model response that can be easily interpreted in terms of influences of various regressors. In contrast, the advantage of NN-based models is the ability to even better represent the input-output mapping required for the forecasting task, but this is accompanied by unstable learning that requires repeated initializations in order to generate good forecasting solutions. The NN-based models also suffer from low interpretability. This is not a problem if only the forecasting accuracy is relevant but can be a hindrance if forecasts have to be understood and

interpreted to properly support control and business decisions. In our case study, the NNLSR model improved the performance of a linear SR model by 7.3 %. This is a significant improvement that suggests that NN or the proposed NNLL structures are encouraged to be considered as forecasting solutions for applied forecasting in the district heating market. Further studies will be conducted to evaluate the adaptive versions of forecasting models [20], and take into account the influences of weather forecasting accuracy that influences heat load forecasts in online forecasting applications.

6 REFERENCES

- [1] European Commission, Climate Action, Roadmap for moving to a low-carbon economy in 2050, from <http://ec.europa.eu/clima/policies/roadmap/> accessed on 2015-02-26.
- [2] Connolly, D., Lund, H., Mathiesen, B.V., Werner, S., Möller, B., Persson, U., Boermans, T., Trier, D., Østergaard, P.A., Nielsen, S. (2014). Heat roadmap Europe: Combining district heating with heat savings to decarbonise the EU energy system. *Energy Policy*, vol. 65, p. 475-489, DOI:10.1016/j.enpol.2013.10.035.
- [3] Yeo, I.A., Yoon, S.H., Yee, J.J.: Development of an urban demand forecasting system to support environmentally friendly urban planning. *Applied Energy*, vol. 110, p. 304-317, DOI:10.1016/j.apenergy.2013.04.065.
- [4] Soldo, B. (2012). Forecasting natural gas consumption. *Applied Energy*, vol. 92, p. 26-37, DOI:10.1016/j.apenergy.2011.11.003.
- [5] Mestekemper, T., Kauermann, G., Smith, M.S. (2013). A comparison of periodic autoregressive and dynamic factor models in intraday energy demand forecasting. *International Journal of Forecasting*, vol. 29, no. 1, p. 1-12, DOI:10.1016/j.ijforecast.2012.03.003.
- [6] Gadd, H., Werner, S. (2013). Daily heat load variations in Swedish district heating systems. *Applied Energy*, vol. 106, p. 47-55, DOI:10.1016/j.apenergy.2013.01.030.
- [7] Dotzauer, E. (2002). Simple model for prediction of loads in district heating systems. *Applied Energy*, vol. 73, no. 3-4, p. 277-284, DOI:10.1016/S0306-2619(02)00078-8.
- [8] Nielsen, H.A., Madsen, H. (2006). Modelling the heat consumption in district heating systems using a grey-box approach. *Energy and Buildings*, vol. 38, no. 1, p. 63-71, DOI:10.1016/j.enbuild.2005.05.002.
- [9] Lee, C.-M., Ko, C.-N. (2011). Short-term load forecasting using lifting scheme and ARIMA models. *Expert Systems with Applications*, vol. 38, p. 5902-5911, DOI:10.1016/j.eswa.2010.11.033.
- [10] Goia, A., May, C., Fusai, G. (2010). Functional clustering and linear regression for peak load forecasting. *International Journal of Forecasting*, vol. 26, p. 700-711, DOI:10.1016/j.ijforecast.2009.05.015.
- [11] Aberg, M., Widén J. (2013). Development, validation and application of a fixed district heating model structure that requires small amounts of input data. *Energy Conversion and Management*, vol. 75, p. 74-85, DOI:10.1016/j.enconman.2013.05.032.
- [12] Bacher, P., Madsen, H., Aalborg Nielsen, H., Perers, B. (2013). Short-term heat load forecasting for single family houses. *Energy and buildings*, vol. 65, p. 101-112, DOI:10.1016/j.enbuild.2013.04.022.
- [13] Thaler, M. (2009). *An analytical-empirical model of heat demand in a district heating system*, PhD thesis. University of Ljubljana, Faculty of Mechanical Engineering, Ljubljana (in Slovene)
- [14] Guo, Y., Nazarian, E., Ko, J., Rajurkar, K. (2014). Hourly cooling load forecasting using time-indexed ARX models with two-stage weighted least squares regression. *Energy Conversion and Management*, vol. 80, p. 46-53, DOI:10.1016/j.enconman.2013.12.060.
- [15] Powell, K.M., Sriprasad, A., Cole, W.J., Edgar, T.F. (2014). Heating, cooling, and electrical load forecasting for a large-scale district energy system. *Energy*, vol. 74, p. 877-885, DOI:10.1016/j.energy.2014.07.064.
- [16] Hyndman, R.J., Koehler, A.B. (2006). Another look at measures of forecast accuracy. *International Journal of Forecasting*, vol. 22, no. 4, p. 679-688, DOI:10.1016/j.ijforecast.2006.03.001.
- [17] Draper, N., Smith, H. (1981). *Applied Regression Analysis*, 2nd ed. John Wiley & Sons, New York.
- [18] Haykin, S. (2009). *Neural Networks and Learning Machines*, 3rd ed., Pearson, New York.
- [19] Soldo, B., Potočnik, P., Šimunović, G., Šarić, T., Govekar, E. (2014). Improving the residential natural gas consumption forecasting models by using solar radiation. *Energy and Buildings*, vol. 69, p. 498-506, DOI:10.1016/j.enbuild.2013.11.032.
- [20] Potočnik, P., Soldo, B., Šimunović, G., Šarić, T., Jeromen, A., Govekar, E. (2014). Comparison of static and adaptive models for short-term residential natural gas forecasting in Croatia. *Applied Energy*, vol. 129, p. 94-103, DOI:10.1016/j.apenergy.2014.04.102.

Vsebina

Strojniški vestnik - Journal of Mechanical Engineering

letnik 61, (2015), številka 9
Ljubljana, september 2015
ISSN 0039-2480

Izhaja mesečno

Razširjeni povzetki

- Luka Čerče, Franci Pušavec, Janez Kopač: Tridimenzionalna karakterizacija obrabe rezalnega orodja SI 93
Matej Müller, Gorazd Novak, Franc Steinman, Gašper Rak, Tom Bajcar: Vpliv operativnih in geometrijskih karakteristik zaklopne zapornice na koeficient bočnega preliva SI 94
Mohsen Moslemi, Mohammadreza Khoshhravan: Izbira parametrov kohezijske cone za napovedovanje medpovršinske delaminacije tipa I SI 95
Andrzej Milecki, Dominik Rybarczyk: Modeliranje elektrohidravličnega proporcionalnega ventila s sinhronskim motorjem SI 96
Yu Zhang, Hongzhi Yan, Tao Zeng: Računalniška zasnova in simulacija ubiranja in stika hipoidnih zobnikov Formate, izdelanih po metodi Duplex Helical SI 97
Jernej Laloš, Tomaž Požar, Janez Možina: Visokofrekvenčna umeritev piezoelektričnega senzorja pomikov z uporabo elastičnih valov vzbujenih s svetlobnim tlakom SI 98
Primož Potočnik, Ervin Strmčnik, Edvard Govekar: Linearni modeli in modeli na osnovi nevronskih mrež za kratkoročno napovedovanje odjema toplote SI 99

Osebne vesti

SI 100

Tridimenzionalna karakterizacija obrabe rezalnega orodja

Luka Čerče* – Franci Pušavec – Janez Kopač
Univerza v Ljubljani, Fakulteta za strojništvo, Slovenija

V članku je predstavljena metoda tridimenzionalnega merjenja obrabe rezalnega orodja direktno na stroju. Na podlagi zajetih meritev je predlagana nova metodologija določevanja obstojnosti rezalnega orodja.

Obraba rezalnega orodja ima zelo močan vpliv na kakovost izdelkov, kot tudi učinkovitost postopkov obdelave. Kljub dandanes visoki stopnji avtomatizacije odrezovalnih procesov, ostaja nekaj ključnih področji, ki preprečujejo popolno avtomatizacijo celotnega procesa. Eno od teh področji je obraba rezalnega orodja. Le ta se običajno meri na orodjarskih mikroskopi izven obdelovalnega procesa. Zato je sprotna karakterizacija obrabe rezalnega orodja ključnega pomena.

V članku je predstavljen inovativen, robusten in zanesljiv merilni sistem za tridimenzionalno merjenje obrabe rezalna orodja, z uporabo laserskega profilometra. Zasnovan merilni sistem omogoča zajem tridimenzionalne oblike obrabe rezalnega orodja, kar predstavlja glavno prednost pred trenutno uporabljenimi dvodimenzionalnimi tehnikami (orodjarski mikroskopi, itd.). Druga pomanjkljivost trenutno uporabljene tehnike (orodjarski mikroskopi, itd.) je njihova subjektivna narava merjenja (točnost meritve je odvisna od operaterja). V delu predstavljen merilni sistem odpravlja potrebo po ročnem merjenju obrabe rezalnega orodja in tako zmanjša čas meritve.

Predstavljen merilni sistem je bil poskusno testiran na študiji primera obdelovalnosti. Velik poudarek je podan na opravljenih analizah prostorskih obrabe rezalnega orodja. Poleg meritev obrabe rezalnega orodja je bilo v delu opravljeno tudi modeliranje obrabe in karakterizacija obstojnosti rezalnega orodja. Na podlagi le-tega je predlagana nova cenilka za definiranje obstojnosti rezalnega orodja, ki vključuje prostorske značilnosti izmerjene obrabe.

Rezultati dela kažejo, da predstavlja na novo zasnovan merilni sistem za diagnosticiranje obrabe in obstojnosti rezalnega orodja objektivno in robustno tehniko za sprotno spremljanje obrabe rezalnega orodja, brez prekinitve procesa obdelave. Kot doprinos je iz prispevka razvidno, da takšna avtomatizacija diagnostike obrabe rezalnega orodja direktno na stroju izboljša produktivnost in kakovost procesa obdelave.

Ključne besede: proces odrezavanja, merjenje obrabe rezalnega orodja, tridimenzionalna obraba rezalnega orodij, sprotno spremljanje obrabe rezalnega orodja, volumska cenilka, napovedovanje obstojnosti rezalnega orodja

Vpliv operativnih in geometrijskih karakteristik zaklopne zapornice na koeficient bočnega preliva

Matej Müller^{1,*} – Gorazd Novak² – Franc Steinman³ – Gašper Rak³ – Tom Bajcar⁴

¹ DHD d.o.o., Digitalna hidrodinamika, Slovenija

² Hidroinštitut, Inštitut za hidravlične raziskave, Slovenija

³ Univerza v Ljubljani, Fakulteta za gradbeništvo in geodezijo, Slovenija

⁴ Univerza v Ljubljani, Fakulteta za strojništvo, Slovenija

Ker se pri bočnih prelivih velikokrat pojavi potreba po reguliranju pretoka vode preko preliva, se v ta namen velikokrat uporabljajo t.i. zaklopne zapornice. Za ustrezno projektiranje in tudi obratovanje zaklopnih zapornic je potrebno dobro poznavanje pretočne sposobnosti obravnavanih objektov. Izdelanih je bilo že nekaj hidravličnih analiz takšnih zapornic na čelnih prelivih, medtem ko smo pri pregledu literature opazili veliko pomanjkanje raziskav takšnih zapornic na bočnih prelivih. S poznavanjem tako kvalitativnega kot tudi kvantitativnega poteka hitrosti bi lahko lažje opredelili hidravlične lastnosti ob takšnih zapornicah, s tem pa bi lahko pomembno izboljšali tako projektiranje kot tudi samo obratovanje zaklopnih zapornic na bočnih prelivih.

V sklopu eksperimentalnega dela so bile izvedene meritve pretokov in gladin za 380 variant z različnimi dimenzijami preliva ter različnimi koti odprtja in robnimi pogoji v pravokotnem kanalu.

Izdelan je bil fizični model bočnega preliva z zaklopno zapornico, ki je bil nameščen v 6 m dolg prizmatični kanal. Obravnavane so bile različne dolžine bočnega preliva ter različne višine praga. Prav tako so bile meritve narejene za različna vtočna Froude-ova števila in različne prelivne višine, kjer se je oboje spreminjalo naključno. Pri vseh variantah pa je bilo upoštevanih še 7 različnih odprtij zapornice.

Analiza koeficienta C_d bočnega preliva z zapornico je pokazala, da je le-ta močno odvisen od kota odprtja zapornice φ . Ugotovljen je bil trend, ki približno sledi polinomski funkciji 3 stopnje.

Izdelana je bila nova enačba za koeficient bočnega preliva z zaklopno zapornico. Enačba je bila razdeljena na dva dela. V prvem delu je zajet vpliv ostrorobega bočnega preliva, medtem ko je v drugem delu zajet vpliv kota odprtja in širine zaklopne zapornice. Na ta način je mogoče skupen C_d zaklopne zapornice na bočnem prelivu izračunati tudi s pomočjo enačb drugih avtorjev za ostrorobi bočni preliv, ki pa jih je treba pomnožiti še z novim koeficientom C_φ .

Ugotovljeno je bilo zelo dobro sovpadanje med izmerjenimi in po novi enačbi izračunanimi koeficienti preliva. Rezultati so bili primerjani tudi z enačbami drugih avtorjev za koeficiente ostrorobega preliva in preliva s širokim pragom. Tudi v tem primeru je bilo ugotovljeno dobro sovpadanje.

Za vse primere dodatnih meritev so bile opravljene še meritve gladin vzdolž roba zapornice ter meritve hitrostnih polj v horizontalni ravnini tik nad prelivnim robom zapornice z računalniško podprto vizualizacijsko metodo, ki predstavlja novejšo metodo, razvito na Univerzi v Ljubljani, Fakulteti za strojništvo. Ta metoda omogoča kvantifikacijo hitrosti v celotni merjeni ravnini. Iz teh meritev je bilo mogoče pokazati, da se kontrakcija curka in s tem pretočna površina na robu zapornice bistveno spreminja s kotom odprtja φ . Iz meritev hitrostnih polj v ravnini tik nad prelivom zapornice pa je bilo ugotovljeno, da ima zelo velik vpliv na koeficient C_d bočnega preliva z zapornico tudi hidrodinamičnost, ki jo pogojuje prav položaj zapornice. Tako je preliv najbolj hidrodinamične oblike pri kotu odprtja $\varphi = 33^\circ$, kjer doseže prelivni koeficient C_d tudi maksimum.

Izdelana nova enačba bo pripomogla k boljšemu in natančnejšemu projektiranju bočnih prelivov z zaklopnimi zapornicami, prav tako pa bo pripomogla k ustrežnejšemu obratovanju takšnih objektov. Prav tako bodo rezultati uporabni za verifikacijo numeričnih modelov, ki se zadnja leta vse pogosteje uporabljajo za hidravlične analize takšnih objektov.

V tej študiji je bila obravnavana ravna zaklopna zapornica brez vpliva spodnje vode v stranskem kanalu. Kot nadaljnje delo bi bilo zelo uporabno analizirati še odvisnost pretočnega koeficienta C_d od oblike zapornice (različne ukrivljenosti) in od višine spodnje vode v stranskem kanalu. Prav tako bi bilo zanimivo dobljene rezultate primerjati z rezultati numeričnega modela, ki bi v tem primeru moral biti tridimenzionalni z ustreznim modelom turbulence.

Ključne besede: bočni preliv, koeficient preliva, zaklopne zapornice, vizualizacijska metoda, pretočnost preliva

Izbira parametrov kohezijske cone za napovedovanje medpovršinske delaminacije tipa I

Mohsen Moslemi^{1,*} – Mohammadreza Khoshhravan²

¹Klub mladih raziskovalcev in elite, Islamska univerza Azad, Iran

²Univerza v Tabrizu, Oddelek za strojništvo, Iran

Delaminacija je vrsta napake, ki se pogosto pojavlja pri laminiranih kompozitih in jo opisujemo kot ločevanje plasti ali skupine plasti od sosednjih plasti zaradi delovanja zunajravninskih strižnih obremenitev. Za napovedovanje zmogljivosti ter izboljšanje zanesljivosti in varnosti konstrukcij je pomembno, da zaznavamo in analiziramo progresivno rast delaminacije.

Predstavljena raziskava je bila namenjena pripravi primerne metodologije za karakterizacijo loma pri delaminaciji tkanih kompozitnih laminatov v pogojih čistih obremenitev tipa I. Simulacija loma materialov s kohezivnimi elementi zahteva obsežne izkušnje za določanje mreže, točne vrednosti parametrov za karakterizacijo zakona trakcije-ločevanja in tudi ustrezno obliko trakcije-ločevanja. Predlagana je nova metodologija preizkusov za določanje normalne kohezivne trdnosti (NCS) kompozitnih laminatov. Vrednost interlaminarne lomne žilavosti za interlaminarni lom tkanega kompozitnega laminata steklo/epoksi tipa I je bila izračunana s preizkusom z uporabo dvojnega konzolnega nosilca (DCB). Preizkušanci za DCB in NCS so bili izdelani s tehniko ročnega polaganja, predrazpoka pa je bila ustvarjena s 13 μm debelim teflonskim vložkom v središčni ravnini kompozitne plošče. Vsi preizkusi DCB in NCS so bili opravljeni pri sobni temperaturi zraka s spremljanjem odmikov pri hitrostih glave 1 mm/min in 0,5 mm/min. Za spremljanje dolžine razpoke je bil na rob preizkušancev prilepljen papir z natisnjeno delitvijo, ki je bil med eksperimentom fotografiran. Za redukcijo podatkov pri vrednotenju lomne žilavosti je bila uporabljena popravljena teorija nosilcev in pridobljena je bila približno gladka krivulja upornosti. Nato je bila opravljena simulacija po modelu kohezivne cone na podlagi končnih elementov stika. Da bi preprečili interpenetracijo površin razpok in umetno skladnost v numerični analizi, je bila opredeljena ustrezna kazenska togost. Za simulacijo procesa nastajanja poškodbe s kohezivnimi elementi v Abaqusu je bil uporabljen spremenjeni Park-Paulino-Roeslerjev (PPR) zakon trakcije-ločevanja v kombinaciji z bilinearnim mešanim modelom poškodb. Numerični rezultati so bili primerjani z rezultati eksperimentov, pri čemer je bilo ugotovljeno, da se dobro skladajo z eksperimentalno ugotovljeno normalno kohezijsko trdnostjo. Določena je bila dolžina kohezivne cone kot razdalja med največjo trakcijo in čelom razpoke. Prilagojeni model PPR je primeren za reprodukcijo eksperimentalno ugotovljenega vedenja kompozitnih preizkušancev in reprodukcijo približno gladke iniciacije razpoke in širjenja, medtem ko bilinearni model opisuje nenadno širjenje poškodbe. Največja razlika med eksperimentalnim in bilinearnim modelom je znašala 8,8 %, pri modelu PPR pa je znašala 2,6 %.

Avtorji so mnenja, da je model PPR točen model za karakterizacijo poškodb materiala. Prilagojeni model PPR bolje upošteva območje lomnega procesa, ki se ustvari pred vrhom razpoke kot bilinearni model. Da bi zagotovili zadostno razpršitev energije, ki uspešno napoveduje začetek in napredovanje delaminacije, smo simulirali več preizkušancev DCB z različnimi velikostmi kohezivnih elementov in dolžino kohezivne cone. Rezultati kažejo konvergirano rešitve pri vseh velikosti mreže, za točno napovedovanje začetka delaminacije pa mora biti mreža manjša od 1 mm.

Ključne besede: model kohezivne cone, delaminacija, normalna kohezijska trdnost, napovedovanje s končnimi elementi

*Naslov avtorja za dopisovanje: Klub mladih raziskovalcev in elite, Islamska univerza Azad, Tabriz, Iran, m.moslemi@tabrizu.ac.ir

Modeliranje elektrohidravličnega proporcionalnega ventila s sinhronskim motorjem

Andrzej Milecki, Dominik Rybarczyk

Tehniška univerza v Poznaniu, Inštitut za mehansko tehnologijo, Poljska

Elektrohidravlični servopogoni se lahko krmilijo z električnimi ventili dveh vrst: servoventili ali proporcionalnimi ventili. Danes se najpogosteje uporabljajo proporcionalni ventili, saj izpolnjujejo večino potreb industrijskih aplikacij in so obenem precej cenejši od servoventilov. Vreteno proporcionalnega ventila upravljata en ali dva elektromagneta. Vreteno odpira hidravlične prehode ter tako omogoča gladko in zvezno nastavljanje pretoka ali tlaka v odvisnosti od električnega vhodnega signala. Osnovna konstrukcija tovrstnih ventilov je bila opredeljena že pred 30 leti in od tedaj na tem področju ni bilo bistvenega napredka. Mnoge raziskave in objave o elektrohidravličnih ventilih so bile posvečene izboljšavam lastnosti teh pogonov z implementacijo sodobnih oblik in načinov krmiljenja. Le nekaj del pa se je ukvarjalo s parametri elementov elektrohidravličnega pogona ter z iskanjem novih rešitev za zelo natančno gibanje delov ventila, kot je npr. vreteno. Kot pogonski del drsnega elementa v proporcionalnih ventilih se danes najpogosteje uporabljajo proporcionalni elektromagneti. Čeprav so znani že zelo dolgo, pa le nekaj rešitev uporablja koračne ali enosmerne motorje. Zato smo se odločili za uporabo novega elektromehanskega aktuatorja v proporcionalnem ventilu – sinhronskega motorja s trajnim magnetom (PMSM). Ta motor ima zelo dobre lastnosti in lahko zagotavlja zelo dobro natančnost pozicioniranja.

V članku je predstavljena zasnova proporcionalnega ventila s sinhronskim motorjem s trajnim magnetom (PMSM), ki premika vreteno hidravličnega ventila. Motorna gred in vreteno sta povezana s fleksibilno sklopko, drugi konec vretena pa je neposredno povezan s krogličnim vretenom, katerega matica je pritrjena na telo ventila. Vrtenje motornega vretena povzroča vrtenje navojnega vretena ter aksialno gibanje vretena in njegovih krmilnih robov. Premik je sorazmeren s kotnim odmikom motorja in korakom navoja. Smer vrtenja določa smer translacije vretena ter odpiranja ali zapiranja prehodov v ventilu. Olje posledično priteka v komore aktuatorja in odteka iz njih, bat se premakne. Premer uporabljenega ventilskega vretena je bil 10 mm, v telesu pa so bili trije pravokotni prehodi dimenzij 2,5 mm × 2 mm. Uporabljen je bil ventil velikosti 10 (pod 64 dm³/min). Položaj rotorja meri absolutni dajalnik, ki zagotavlja pozicioniranje z veliko natančnostjo tudi v primeru izpada napajanja (262144 impulzov na obrat). Linearna ločljivost pogona je tako 0,5 μm.

V članku so opredeljene osnovne enačbe, ki opisujejo ventil, simulacijski model pa je bil pripravljen v programski opremi MATLAB Simulink. Model vključuje tudi izbrane nelinearnosti. Za določitev osnovnih parametrov obravnavanega proporcionalnega ventila je bilo postavljeno preizkuševališče za ventile. Preizkuševališče je bilo opremljeno s programirljivim logičnim krmilnikom z zaslonom na dotik in invertnim modulom. V članku so predstavljene značilnosti pretoka in odziv na stopnico, pridobljeni s simulacijo. Te značilnosti so bile primerjane z rezultati eksperimentalne preiskave in simulacijski model ventila je bil nato spremenjen in izboljššan.

Predstavljeni proporcionalni ventil s sinhronskim motorjem s trajnim magnetom je zanimiva alternativa za servoventile. Zagotavlja lahko boljše lastnosti (še posebej glede dinamike in natančnosti) kot standardni elektrohidravlični proporcionalni ventili z elektromagneti.

Ključne besede: proporcionalni ventil, elektrohidravlika, sinhronski motor

Računalniška zasnova in simulacija ubiranja in stika hipoidnih zobnikov Formate, izdelanih po metodi Duplex Helical

Yu Zhang¹ – Hongzhi Yan^{1,*} – Tao Zeng^{1,2}

¹ Državni laboratorij za visokozmogljivo kompleksno obdelavo, Univerza srednjega juga, Kitajska

² Changsha Haliang Kaishuai Precision Machinery Co. Ltd., Kitajska

Duplex Helical je napreden in najbolj razširjen postopek čelnega rezkanja stožčastih zobnikov z ukrivljenim ozobjem in hipoidnih zobnikov, ki se odlikuje z učinkovitostjo, majhnimi stroški, večjo trdnostjo in možnostjo suhe obdelave. Kitajska industrija danes pri izdelavi omenjenih zobnikov še vedno uporablja predvsem postopek obdelave v petih prehodih, ki ga je v razvitih zahodnih državah že zamenjal postopek Duplex Helical. Metodo Duplex Helical je pred več desetletji izumilo podjetje Gleason in ker je njegova tehnologija zaščitena, v objavljeni literaturi zanj ni mogoče najti posplošene teorije. Ta postopek za razliko od procesa obdelave v petih prehodih omogoča sočasno oblikovanje konveksnih in konkavnih zobnih površin z enim samim naborom nastavitve obdelovalnega stroja, zato je težko določiti optimalne nastavitve, ki dajejo dobre rezultate pri obojestranski analizi zobnega stika (TCA).

V članku je kot rešitev tega problema predlagan natančen in praktičen pristop k izračunavanju osnovnih nastavitve obdelovalnega stroja za izdelavo spiralnih zobnikov s poševnim ozobjem in hipoidnih zobnikov po metodi Duplex Helical. Za iskanje najboljših nastavitve obdelovalnega stroja za izdelavo omenjenih zobnikov po metodi Duplex Helical so bile uporabljene tri referenčne točke (M1, M2 in P) za natančno določanje medsebojnega položaja zobniške dvojice. Točki M1 in M2 se nahajata na pogonski in na gnani strani zobnih površin, tretja referenčna točka P pa je na širini pastorka in se uporablja tudi za spreminjanje dimenzij stožčastih zobnikov s poševnim ozobjem in hipoidnih zobnikov.

Postopek izračunavanja osnovnih nastavitve obdelovalnega stroja za izdelavo zobnikov po metodi Duplex Helical je enak kot pri procesu obdelave s petimi prehodi in članek obravnava osnovne nastavitve za izdelavo pastorka po metodi Duplex Helical. Najprej so bile na podlagi osnovnih nastavitve stroja in rezkalne glave izračunane vektorske funkcije zobnih površin in parametri ukrivljenosti. S konjugacijo površin zobnika in pastorka ter pastorka in rezkalne glave smo dobili dve vrsti parametrov ukrivljenosti za zobne površine pastorka. Nato smo določili osnovne nastavitve stroja za izdelavo pastorka, ki ustrezajo tema dvema vrstama parametrov ukrivljenosti. Končno smo razvili tudi programsko opremo za konstruiranje hipoidnih zobnikov na podlagi prej omenjene strategije določanja osnovnih nastavitve obdelovalnega stroja. Razvita metodologija je bila validirana na primeru dvojice hipoidnih zobnikov, izdelanih po postopku Duplex Helical. S konstrukcijskimi podatki je bila nato opravljena analiza kontaktnih napetosti zob po metodi končnih elementov, preizkus rezanja in kotalni preizkus. Rezultati kažejo, da se nosilna površina zob pri kotalnem preizkusu po velikosti, obliki in položaju ujema z nosilno površino zob pri kontaktni analizi, tri referenčne točke pa lahko učinkovito pomagajo določiti optimalne nastavitve stroja za obojestransko dobre lastnosti TCA.

Pričujoči članek je prvi, ki podrobno opisuje posplošeno teorijo metode Duplex Helical in bo ljudem pomagal pri boljšem razumevanju. Razviti pristop in programska oprema bosta prispevala k uveljavljanju metode Duplex Helical ter k izboljševanju kakovosti in učinkovitosti izdelave stožčastih zobnikov s poševnim ozobjem in hipoidnih zobnikov po metodi Duplex Helical na Kitajskem.

Ključne besede: metoda Duplex Helical, stožčasti zobniki s poševnim ozobjem in hipoidni zobniki, čelno rezkanje, osnovne nastavitve stroja, parameter ukrivljenosti, posplošena teorija, referenčna točka, kontaktna analiza zob

Visokofrekvenčna umeritev piezoelektričnega senzorja pomikov z uporabo elastičnih valov vzbujenih s svetlobnim tlakom

Jernej Laloš* – Tomaž Požar – Janez Možina
Univerza v Ljubljani, Fakulteta za strojništvo, Slovenija

V prispevku je predstavljena kalibracija piezoelektričnega senzorja majhnih pomikov z ultrazvočnimi valovi, ki jih vzbudi svetlobni tlak laserskega bliska na površini steklene plošče. S primerjavo meritev in matematičnega modela širjenja ultrazvoka v trdni snovi je določena frekvenčna karakteristika senzorja pri višjih frekvencah kot doslej.

Merjenje majhnih pomikov snovi je nepogrešljivo pri proučevanju širjenja mehanskega valovanja v snovi. Med vsemi senzorji so najbolj občutljivi tisti, ki delujejo z izkoriščanjem piezoelektričnega pojava, in so zato najbolj primerni za merjenje valovanj z majhno amplitudo pomika. Takšni senzorji so tako v uporabi v strojništvu, pri testiranjih ter v razvoju in raziskavah. Uporabljajo se pri meritvah akustične emisije in pri neporušnih preiskavah snovi, v mikroseizmologiji ter pri mnogih drugih aplikacijah ultrazvoka v snovi.

Cilj umeritve senzorja je določitev njegove prenosne funkcije. Z njo se lahko iz izhodnih signalov senzorja izlušči pomike merjenega mehanskega valovanja. Pri umeritvi se primerjata znan vzbuditveni signal in izmerjen odziv senzorja nanj. Vzbuditveni signal ima običajno obliko mehanskih površinskih valov, ki so bili za potrebe umeritve senzorja izmerjeni z že umerjenim senzorjem ali pa so bili izračunani teoretično na osnovi znanih matematičnih modelov. Mehansko valovanje je v takem primeru ponavadi vzbujeno z mehanskim sunkom sile, kot sta udarec kroglice ali zlom kapilare.

Doslej so bili površinski valovi večinoma izračunani v približku, v katerem sta stična površina senzorja in vpadna površina izvornega sunka sile obravnavani kot točki in ne kot končno veliki površini. Taka približka točkastega izvora in točkastega senzorja sta sicer uporabna pri nizkih frekvencah mehanskega valovanja, nista pa primerna pri višjih frekvencah.

V prispevku opisujemo absolutno kalibracijo koničastega piezoelektričnega senzorja. Tak senzor je zasnovan za absolutno merjenje majhnih izvenravninskih pomikov brez resonance, je hitro odziven in ima dokaj položno frekvenčno karakteristiko pri nižjih frekvencah. Čeprav je metoda primerjave spektrov izhodnega in vhodnega signala senzorja za določitev njegove frekvenčne prenosne funkcije standardna, jo je mogoče izboljšati z natančnejšim teoretičnim modelom merjenega površinskega valovanja. Tako je v prispevku uporabljena metoda modeliranja valov z uporabo Greenovih funkcij, ki upošteva realne dimenzije stične površine senzorja in vpadne površine izvornega sunka sile. Ta metoda realnega-izvora-realnega-senzorja temelji na statistični utežitvi numerično izračunanih Greenovih funkcij za izbrano snov ter za medsebojni legi izvorne sile in senzorja. Kot izvorni sunek sile je bil uporabljen svetlobni tlak laserskega bliska. Optodinamska interakcija takega bliska s snovjo je bistveno hitrejša, natančneje opredeljena in bolj ponovljiva kot katerakoli mehanska interakcija uporabljena doslej. Pri tem načinu vzbujanja je možno spreminjati tudi velikost vpadne površine laserskega bliska in njegovo trajanje.

Kot je prikazano v prispevku, omogoča taka metoda bolj zvesto modeliranje valovnih oblik, ki se širijo po snovi, kot doslej uporabljeni približki. Tako tudi omogoča določitev prave prenosne funkcije senzorja, pri čemer iz nje odstrani efekt aperture senzorja in efekt prostorske porazdelitve izvornega sunka sile. Hitre optodinamske interakcije kratkih laserskih bliskov pa omogočajo vzbujanje mehanskih valov in kalibracijo senzorja pri višjih frekvencah, kot jih omogočajo mehanske vzbuditvene interakcije.

Ključne besede: absolutna kalibracija senzorja, piezoelektrični senzor, laserski pulz, efekt aperture, elastični valovi v plošči, optodinamika, Greenove funkcije

Linearni modeli in modeli na osnovi nevronske mreže za kratkoročno napovedovanje odjema toplote

Primož Potočnik* – Ervin Strmčnik – Edvard Govekar
Univerza v Ljubljani, Fakulteta za strojništvo, Slovenija

Raziskava obravnava problematiko kratkoročnega napovedovanja odjema toplote v sistemu daljinskega ogrevanja. Kakovostne napovedi odjema toplote v vročevodnem sistemu so zelo pomembne s stališča učinkovite rabe energije, ki zahteva usklajevanje prihodnih potreb odjemalcev ter proizvodnje in dobave ustreznih količin toplote. Napovedovanje odjema toplote sodi zaradi prisotnosti kompleksnih procesov med zahtevnejše naloge daljinskega ogrevanja, kratkoročne napovedi pa so direktno uporabne za učinkovito krmiljenje in optimizacijo sistema daljinskega ogrevanja.

Osredotočili smo se na napovedovanje odjema toplote Q na dnevnem nivoju za en dan naprej, torej $Q(t+1)$, pri čemer t izraža čas na dnevnem nivoju. Kakovost napovedovanja smo ocenili s pomočjo tako imenovane MARNE napake (ang. *mean absolute range normalized error*), ki izraža povprečno procentualno odstopanje napovedi, normiranih na maksimalno prenosno kapaciteto sistema (Q_{max}). Posplošitveno sposobnost obravnavanih modelov smo ocenjevali na osnovi križnega vrednotenja, kjer smo 60 % podatkov uporabili za učenje modelov, preostalih 40 % pa za testiranje modelov. Za končno oceno kakovosti modelov smo uporabili testno napako MARNE, ki predstavlja neodvisno mero kakovosti modelov in njihove posplošitvene zmožnosti.

Pri raziskavi smo uporabili podatke o odjemu toplote na področju Mestne občine Ljubljana od septembra 2008 do februarja 2013, ki smo jih prejeli s strani podjetja Energetika Ljubljana. Na voljo smo imeli podatke za naslednje fizikalne veličine: odjem toplote Q , temperaturo ozračja T , sončno obsevanje R , hitrost vetra W in relativno vlažnost zraka H . Poleg naštetih podatkov smo izpeljali še dodatne značilke za označevanje linearnega trenda in sezonskega cikla, ter treh dodatnih značilok za označevanje delavnikov, sobot in nedelj (ter praznikov).

Za napovedovanje smo raziskali uporabo različnih vrst modelov, vključno s preprostimi referenčnimi modeli (model *random walk* in model temperaturne korelacije), linearnimi modeli (regresijski modeli, avtoregresijski modeli, modeli stopenjske regresije), ter nelinearnimi modeli (nevronske mreže, nevronske mreže z direktno linearno vhodno-izhodno povezavo). Pri nelinearnih modelih je učenje obsegalo 200 iteracij naključne inicializacije parametrov modela in nato gradientno učenje po metodi *Levenberg-Marquardt*.

Rezultati obeh referenčnih modelov znašajo prek 3 % (testna napaka MARNE), in sicer 3,23 % za model *random walk* in 3,43 % za model temperaturne korelacije. Z linearnimi modeli je mogoče bistveno izboljšati kakovost napovedovanja. Testna napaka regresijskega modela znaša 2,62%, avtoregresijskih modelov pa 1,33 %. Rezultat najboljšega linearnega modela (model stopenjske regresije), ki uporablja optimizirano podmnožico vključenih spremenljivk, znaša 1,24 %. Takšen model je že primeren za uporabo v sistemih daljinskega ogrevanja, saj ga poleg dobre kakovosti napovedovanja označuje tudi robustnost in nizka kompleksnost.

Glede uporabe nelinearnih modelov, zasnovanih na osnovi nevronske mreže, lahko podamo več ugotovitev: 1) izgradnja kakovostnega modela zahteva več ponovitev naključnih inicializacij parametrov modela, 2) za obravnavani proces odjema toplote zadošča le nekaj nevronov skrite plasti mreže, 3) najboljši nelinearni modeli še izboljšajo kakovost napovedovanja linearnih modelov – najboljši rezultat nevronskega modela z direktno linearno vhodno-izhodno povezavo znaša 1,15 %, kar pomeni še 7,3 % izboljšanje glede na najboljši linearni model.

Zato lahko zaključimo, da je poleg enostavnih in robustnih linearnih modelov na področju napovedovanja odjema toplote v sistemih daljinskega ogrevanja smiselna tudi uporaba nelinearnih modelov na osnovi nevronske mreže, s katerimi lahko še izboljšamo kakovost napovedovanja. Problem modelov na osnovi nevronske mreže je slaba interpretabilnost in nestabilno učenje, ki zahteva več interakcij učnega postopka, vendar rezultati kažejo, da lahko ustrezno pripravljene nevronske modele še bistveno izboljšajo kakovost kratkorčnih napovedi prihodnjega odjema toplote.

Ključne besede: daljinsko ogrevanje, napovedovanje odjema toplote, izpeljava značilok, stopenjska regresija, avtoregresijski model, nevronske mreže

Doktorski disertaciji, znanstveno magistrsko delo

DOKTORSKI DISERTACIJI

Na Fakulteti za strojništvo Univerze v Ljubljani sta obranila svojo doktorsko disertacijo:

- dne 2. julija 2015 **Jasenko PERENDA** z naslovom: »Spremembe napetostno deformacijskega stanja v torzijski vzmeti pri izdelavi in obratovanju« (mentor: prof. dr. Ivan Prebil, somentor: prof. dr. Janez Grum);

V proizvodnji torzijskih vzmeti se uporabljata dva različna mehanska postopka vnosa zaostalih napetosti v torzijsko vzmet: prednapenjanje in globoko valjanje. Namen teh postopkov je vnos zaostalih tlačnih napetosti v površinske sloje vzmeti z namenom povečanja dobe trajanja torzijske vzmeti. Material torzijskih vzmeti je karakteriziran z vrsto cikličnih natezno tlačnih preizkusov. Preverjanje MKE simulacije pravilnega proizvodnega zaporedja teh dveh postopkov ter porazdelitev in stabilizacija koristnih zaostalih napetosti je opravljena z meritvami zaostalih napetosti;

- dne 10. julija 2015 **Andrej SKUMAVC** z naslovom: »Uporaba novih dodatnih materialov za popravilo orodij za tlačno litje z varjenjem« (mentor: prof. dr. Janez Tušek);

V doktorskem delu so predstavljene zlitine na bazi kovin volframa in molibdena, ki zaradi svojih specifičnih fizikalnih in mehanskih lastnosti dajejo možnosti za uporabo na področju reparaturnega varjenja orodij za tlačno litje. Doktorsko delo je razdeljeno na tri glavne dele. Prvi del vključuje raziskave komercialno dostopnega dodatnega materiala iz zlitine WNi28Fe15, za katerega v pregledani znanstveni in strokovni literaturi še ni objav. Omenjeni dodajni material je bil nato

uporabljen v raziskavi sočelnega zvarnega spoja med dvema ploščama iz orodnega jekla za delo v vročem. V drugem delu disertacije smo po postopku metalurgije prahov izdelali več zlitin na bazi kovin volframa in molibdena. Naknadno so bile sintrane zlitine pretaljene s postopkom obločnega talilnega varjenja v zaščiti inertnega plina TIG ter nato visokotemperaturno žarjene pri različnih temperaturah in časih. Mikrostruktura pretaljenih in žarjenih zlitin je bila analizirana z uporabo optičnega in elektronskega mikroskopa, dodatno pa je bila za potrditev obstoja določenih mikrostrukturnih sestavin uporabljena še rentgenska strukturna analiza XRD. V zadnjem delu disertacije so bile izvedene še raziskave obrabne odpornosti navara iz zlitine WNi28Fe15 pri povišani temperaturi v laboratorijskih pogojih preizkušanja. Na zlitinah WNi28Fe15 in MoNi22Fe13 so bile izvedene tudi dilatometrijske preiskave v temperaturnem območju od 25 °C do 1100 °C. Temperaturno utrujanje navara iz zlitine WNi28Fe15 smo izvedli v laboratoriju na napravi za induktivno segrevanje, prav tako pa je bila zlitina prvič uspešno uporabljena v serijski proizvodnji tlačnega litja.

*

ZNANSTVENO MAGISTRSKO DELO

Na Fakulteti za strojništvo Univerze v Ljubljani je z uspehom zagovarjal svojo magistrsko delo:

dne 1. julija 2015:

Igor LEKŠE z naslovom: »Obvladovanje zravnavevanja pri hladnem upogibanju cevi« (mentor: prof. dr. Karl Kuzman, somentor: prof. dr. Alojzij Sluga).

Information for Authors

All manuscripts must be in English. Pages should be numbered sequentially. The manuscript should be composed in accordance with the Article Template given above. The maximum length of contributions is 10 pages. Longer contributions will only be accepted if authors provide justification in a cover letter. For full instructions see the Information for Authors section on the journal's website: <http://en.sv-jme.eu>.

SUBMISSION:

Submission to SV-JME is made with the implicit understanding that neither the manuscript nor the essence of its content has been published previously either in whole or in part and that it is not being considered for publication elsewhere. All the listed authors should have agreed on the content and the corresponding (submitting) author is responsible for having ensured that this agreement has been reached. The acceptance of an article is based entirely on its scientific merit, as judged by peer review. Scientific articles comprising simulations only will not be accepted for publication; simulations must be accompanied by experimental results carried out to confirm or deny the accuracy of the simulation. Every manuscript submitted to the SV-JME undergoes a peer-review process.

The authors are kindly invited to submit the paper through our web site: <http://ojs.sv-jme.eu>. The Author is able to track the submission through the editorial process - as well as participate in the copyediting and proofreading of submissions accepted for publication - by logging in, and using the username and password provided.

SUBMISSION CONTENT:

The typical submission material consists of:

- A **manuscript** (A PDF file, with title, all authors with affiliations, abstract, keywords, highlights, inserted figures and tables and references),
- Supplementary files:
 - a **manuscript** in a WORD file format
 - a **cover letter** (please see instructions for composing the cover letter)
 - a ZIP file containing **figures** in high resolution in one of the graphical formats (please see instructions for preparing the figure files)
 - possible **appendices** (optional), cover materials, video materials, etc.
- Incomplete or improperly prepared submissions will be rejected with explanatory comments provided. In this case we will kindly ask the authors to carefully read the Information for Authors and to resubmit their manuscripts taking into consideration our comments.

COVER LETTER INSTRUCTIONS:

Please add a **cover letter** stating the following information about the submitted paper:

1. Paper **title**, list of **authors** and their **affiliations**.
2. **Type of paper**: original scientific paper (1.01), review scientific paper (1.02) or short scientific paper (1.03).
3. A **declaration** that neither the manuscript nor the essence of its content has been published in whole or in part previously and that it is not being considered for publication elsewhere.
4. State the **value of the paper** or its practical, theoretical and scientific implications. What is new in the paper with respect to the state-of-the-art in the published papers? Do not repeat the content of your abstract for this purpose.
5. We kindly ask you to suggest at least two **reviewers** for your paper and give us their names, their full affiliation and contact information, and their scientific research interest. The suggested reviewers should have at least two relevant references (with an impact factor) to the scientific field concerned; they should not be from the same country as the authors and should have no close connection with the authors.

FORMAT OF THE MANUSCRIPT:

The manuscript should be composed in accordance with the Article Template. The manuscript should be written in the following format:

- A **Title** that adequately describes the content of the manuscript.
- A list of **Authors** and their **affiliations**.
- An **Abstract** that should not exceed 250 words. The Abstract should state the principal objectives and the scope of the investigation, as well as the methodology employed. It should summarize the results and state the principal conclusions.
- 4 to 6 significant **key words** should follow the abstract to aid indexing.
- 4 to 6 **highlights**; a short collection of bullet points that convey the core findings and provide readers with a quick textual overview of the article. These four to six bullet points should describe the essence of the research (e.g. results or conclusions) and highlight what is distinctive about it.
- An **Introduction** that should provide a review of recent literature and sufficient background information to allow the results of the article to be understood and evaluated.
- A **Methods** section detailing the theoretical or experimental methods used.
- An **Experimental section** that should provide details of the experimental set-up and the methods used to obtain the results.
- A **Results** section that should clearly and concisely present the data, using figures and tables where appropriate.
- A **Discussion** section that should describe the relationships and generalizations shown by the results and discuss the significance of the results, making comparisons with previously published work. (It may be appropriate to combine the Results and Discussion sections into a single section to improve clarity.)
- A **Conclusions** section that should present one or more conclusions drawn from the results and subsequent discussion and should not duplicate the Abstract.
- **Acknowledgement** (optional) of collaboration or preparation assistance may be included. Please note the source of funding for the research.
- **Nomenclature** (optional). Papers with many symbols should have a nomenclature that defines all symbols with units, inserted above the references. If one is used, it must contain all the symbols used in the manuscript and the definitions should not be repeated in the text. In all cases, identify the symbols used if they are not widely recognized in the profession. Define acronyms in the text, not in the nomenclature.
- **References** must be cited consecutively in the text using square brackets [1] and collected together in a reference list at the end of the manuscript.
- **Appendix(-ices)** if any.

SPECIAL NOTES

Units: The SI system of units for nomenclature, symbols and abbreviations should be followed closely. Symbols for physical quantities in the text should be written in italics (e.g. v , T , n , etc.). Symbols for units that consist of letters should be in plain text (e.g. ms^{-1} , K, min, mm, etc.). Please also see: <http://physics.nist.gov/cuu/pdf/sp811.pdf>.

Abbreviations should be spelt out in full on first appearance followed by the abbreviation in parentheses, e.g. variable time geometry (VTG). The meaning of symbols and units belonging to symbols should be explained in each case or cited in a **nomenclature** section at the end of the manuscript before the References.

Figures (figures, graphs, illustrations digital images, photographs) must be cited in consecutive numerical order in the text and referred to in both the text and the captions as Fig. 1, Fig. 2, etc. Figures should be prepared without borders and on white grounding and should be sent separately in their original formats. If a figure is composed of several parts, please mark each part with a), b), c), etc. and provide an explanation for each part in Figure caption. The caption should be self-explanatory. Letters and numbers should be readable (Arial or Times New Roman, min 6 pt with equal sizes and fonts in all figures). Graphics (submitted as supplementary files) may be exported in resolution good enough for printing (min. 300 dpi) in any common format, e.g. TIFF, BMP or JPG, PDF and should be named Fig1.jpg, Fig2.tif, etc. However, graphs and line drawings should be prepared as vector images, e.g. CDR, AI. Multi-curve graphs should have individual curves marked with a symbol or otherwise provide distinguishing differences using, for example, different thicknesses or dashing.

Tables should carry separate titles and must be numbered in consecutive numerical order in the text and referred to in both the text and the captions as Table 1, Table 2, etc. In addition to the physical quantities, such as t (in italics), the units [s] (normal text) should be added in square brackets. Tables should not duplicate data found elsewhere in the manuscript. Tables should be prepared using a table editor and not inserted as a graphic.

REFERENCES:

A reference list must be included using the following information as a guide. Only cited text references are to be included. Each reference is to be referred to in the text by a number enclosed in a square bracket (i.e. [3] or [2] to [4] for more references; do not combine more than 3 references, explain each). No reference to the author is necessary.

References must be numbered and ordered according to where they are first mentioned in the paper, not alphabetically. All references must be complete and accurate. Please add DOI code when available. Examples follow.

Journal Papers:

Surname 1, Initials, Surname 2, Initials (year). Title. Journal, volume, number, pages, DOI code.

- [1] Hackenschmidt, R., Alber-Laukant, B., Rieg, F. (2010). Simulating nonlinear materials under centrifugal forces by using intelligent cross-linked simulations. *Strojniški vestnik - Journal of Mechanical Engineering*, vol. 57, no. 7-8, p. 531-538, DOI:10.5545/sv-jme.2011.013.

Journal titles should not be abbreviated. Note that journal title is set in italics.

Books:

Surname 1, Initials, Surname 2, Initials (year). Title. Publisher, place of publication.

- [2] Groover, M.P. (2007). *Fundamentals of Modern Manufacturing*. John Wiley & Sons, Hoboken.

Note that the title of the book is italicized.

Chapters in Books:

Surname 1, Initials, Surname 2, Initials (year). Chapter title. Editor(s) of book, book title. Publisher, place of publication, pages.

- [3] Carbone, G., Ceccarelli, M. (2005). Legged robotic systems. Kordić, V., Lazinic, A., Merdan, M. (Eds.), *Cutting Edge Robotics*. Pro literatur Verlag, Mammendorf, p. 553-576.

Proceedings Papers:

Surname 1, Initials, Surname 2, Initials (year). Paper title. Proceedings title, pages.

- [4] Štefančić, N., Martinčević-Mikić, S., Tošanović, N. (2009). Applied lean system in process industry. *MOTSP Conference Proceedings*, p. 422-427.

Standards:

Standard-Code (year). Title. Organisation. Place.

- [5] ISO/DIS 16000-6:2002. *Indoor Air - Part 6: Determination of Volatile Organic Compounds in Indoor and Chamber Air by Active Sampling on TENAX TA Sorbent, Thermal Desorption and Gas Chromatography using MSD/FID*. International Organization for Standardization. Geneva.

WWW pages:

Surname, Initials or Company name. Title, from <http://address>, date of access.

- [6] Rockwell Automation. Arena, from <http://www.arenasimulation.com>, accessed on 2009-09-07.

EXTENDED ABSTRACT:

When the paper is accepted for publishing, the authors will be requested to send an **extended abstract** (approx. one A4 page or 3500 to 4000 characters). The instruction for composing the extended abstract are published on-line: <http://www.sv-jme.eu/information-for-authors/>.

COPYRIGHT:

Authors submitting a manuscript do so on the understanding that the work has not been published before, is not being considered for publication elsewhere and has been read and approved by all authors. The submission of the manuscript by the authors means that the authors automatically agree to transfer copyright to SV-JME when the manuscript is accepted for publication. All accepted manuscripts must be accompanied by a Copyright Transfer Agreement, which should be sent to the editor. The work should be original work by the authors and not be published elsewhere in any language without the written consent of the publisher. The proof will be sent to the author showing the final layout of the article. Proof correction must be minimal and executed quickly. Thus it is essential that manuscripts are accurate when submitted. Authors can track the status of their accepted articles on <http://en.sv-jme.eu/>.

PUBLICATION FEE:

Authors will be asked to pay a publication fee for each article prior to the article appearing in the journal. However, this fee only needs to be paid after the article has been accepted for publishing. The fee is 240.00 EUR (for articles with maximum of 6 pages), 300.00 EUR (for articles with maximum of 10 pages), plus 30.00 EUR for each additional page. The additional cost for a color page is 90.00 EUR. These fees do not include tax.

Strojniški vestnik -Journal of Mechanical Engineering
Askerčeva 6, 1000 Ljubljana, Slovenia,
e-mail: info@sv-jme.eu



<http://www.sv-jme.eu>

Contents

Papers

- 489 Luka Čerče, Franci Pušavec, Janez Kopač:
New Approach in Spatial Tool-Wear Analysis and Monitoring
- 498 Matej Müller, Gorazd Novak, Franc Steinman, Gašper Rak, Tom Bajcar:
Influence of the Operating and Geometric Characteristics of a Bottom-hinged Flap Gate on the Discharge Coefficient of a Side Weir
- 507 Mohsen Moslemi, Mohammadreza Khoshravan:
Cohesive Zone Parameters Selection for Mode-I Prediction of Interfacial Delamination
- 517 Andrzej Milecki, Dominik Rybarczyk:
Modelling of an Electrohydraulic Proportional Valve with a Synchronous Motor
- 523 Yu Zhang, Hongzhi Yan, Tao Zeng:
Computerised Design and Simulation of Meshing and Contact of Formate Hypoid Gears Generated with a Duplex Helical Method
- 533 Jernej Laloš, Tomaž Požar, Janez Možina:
High-Frequency Calibration of Piezoelectric Displacement Sensors Using Elastic Waves Induced by Light Pressure
- 543 Primož Potočnik, Ervin Strmčnik, Edvard Govekar:
Linear and Neural Network-based Models for Short-Term Heat Load Forecasting